HIGH-RESISTIVITY ELECTRICAL STEEL THIN STRIP BY HYBRID DEFORMATION PROCESSING

by

Brhayan Stiven Puentes Rodriguez

A Dissertation

Submitted to the Faculty of Purdue University

In Partial Fulfillment of the Requirements for the degree of

Doctor of Philosophy

School of Materials Engineering

West Lafayette, Indiana

August 2022

THE PURDUE UNIVERSITY GRADUATE SCHOOL

STATEMENT OF COMMITTEE APPROVAL

Dr. Kevin Trumble, Chair

School of Materials Engineering

Dr. Srinivasan Chandrasekar

School of Industrial Engineering

Dr. James Mann

M4 Sciences

Dr. David Johnson

School of Materials Engineering

Approved by:

Dr. David Bahr

I dedicate this work to the people who have believed in and supported me, with special dedications to my wife, father, mother, and brother. The four of you are the core of my life.

ACKNOWLEDGMENTS

The support I have received in my life to get to this point is unmeasurable. To every person who has supported me, cheered for me, or just wished me luck, I thank you.

I want to thank Prof. Liz Herrera and COLCIENCIAS in Colombia for trusting me and giving me my first opportunity to do research.

I want to thank my advisors, Prof. Trumble, Prof. Chandy, Prof. Mann, and Prof. Johnson, for sharing their knowledge, for the long conversations to decipher the challenges of doing research, for showing me the importance of working as a team, and for the constant and honest support during all these years.

I want to thank Dr. Mojib Saei for his support during the strip production work and experiments. Also, I would like to thank Theylor Amaya for his help in collecting the texture data. Special thanks to Dr. Rachid M'Saoubi and Seco Tools for providing specialized tooling for this project.

I want to thank all the School of Materials Engineering staff. You are amazing people. Special thanks to Tim, Lisa, Rosemary, and Jenni. Without your help, I cannot imagine how much harder this Ph.D. would have been.

Thanks to all the lovely friends and colleagues I have met throughout my career, Andres Gil, Julian Rubiano, Luis Ardila, Johana Fuquene, Theylor Amaya, Mojib Saei, David Brice, Xiaolong Bai, Ben Stegman, Tom Mann, Adam Caldwell, Alejandro Alcaraz, Sami El Awad, and Ana Ulloa. Special thanks to Indrani and Mohammed, who shared this Ph.D. ride with me.

Finally, I want to thank my loving family. To my parents, Martha and Martin, my brother Sebas, and my wife Lexie, whose unconditional love and encouragement made this possible.

This material is based upon work supported by the U.S. Department of Energy's Office of Energy Efficiency and Renewable Energy (EERE) under the Advanced Manufacturing Office (AMO) Award Number DE-EE0007868.

Disclaimer: This report was prepared as an account of work sponsored by an agency of the United States Government. Neither the United States Government nor any agency thereof, nor any of their employees, makes any warranty, express or implied, or assumes any legal

liability or responsibility for the accuracy, completeness, or usefulness of any information, apparatus, product, or process disclosed, or represents that its use would not infringe privately owned rights. Reference herein to any specific commercial product, process, or service by trade name, trademark, manufacturer, or otherwise does not necessarily constitute or imply its endorsement, recommendation, or favoring by the United States Government or any agency thereof. The views and opinions of authors expressed herein do not necessarily state or reflect those of the United States Government or any agency thereof.

TABLE OF CONTENTS

LIST OF TABLES

LIST OF FIGURES

ABSTRACT

Electrical steels are one type of soft magnetic material. They are based on Fe-Si alloys and are widely used for magnetic cores in transformers and electric motors. It is well known that Fe-6.5Si wt% is the most efficient composition; however, at such a high silicon concentration (6.5wt.% = 12.1 at.% Si in Fe), the poor workability of the alloy makes it unacceptable for industrial production via conventional sheet steel rolling processes.

This problem was approached in two different ways. First, a machining-based approach that suppresses the mechanisms that lead to cracking during conventional rolling was implemented for processing of thin metal strips. Two related machining-based sheet production technologies called free machining (FM), and hybrid cutting extrusion (HCE) were used to produce strips of high resistivity electrical steel. The maximum strip width achieved was 50 mm, and it was produced with a combination of FM and light rolling with a surface roughness comparable to cold-rolled sheet surfaces. Second, a new experimental alloy Fe-4Si-4Cr wt% was developed with improved magnetic properties compared to ~ Fe-3.2Si wt% and outstanding workability. Results report that the new experimental alloy has an electrical resistivity of $85 \pm 3\ \mu\Omega \cdot cm$ which is higher than Fe-6.5%Si. Also, the results on the Fe-4Si-4Cr workability show that this new alloy can withstand 75% cold-rolled reduction. The magnetic properties characterization was done via standard stacked toroid testing, and results show that Fe-4Si-4Cr experimental alloy exhibits excellent magnetic performance with a reduction in core losses of 33% at 400 Hz compared to commercial alloys with ~ Fe-3.2Si wt%.

Recrystallization kinetics and texture evolution in the experimental alloy were evaluated for traditionally rolled and machining-based samples. Results were used to construct annealing maps. These maps represent the stages of the annealing process for a range of temperature versus time conditions, i.e., the annealing maps are a graphical summary showing the different stages of the annealing process for the Fe-4Si-4Cr experimental alloy in the two conditions. Despite the significant differences in the deformation texture of the two conditions, the recrystallization kinetics were similar. Finally, the two conditions retained the as-deformed texture in the intermediate annealing but to a lesser degree after completing a full anneal. In the case of the rolled sample, it is possible to trace the original texture fibers (γ-fiber, the partial α-fiber, and the θ -fiber)

in the fully annealed data, but the texture intensity is just 2.5 mrd. On the other hand, the texture of the fully annealed HCE sample changes as compared to the as-deformed condition, located close to $(110)[1\bar{1}2]$ with a surprisingly strong peak of ~ 25 mrd.

1. INTRODUCTION

Based on the calculations reported by the DOE [1], a reduction of 37% in core losses of electrical motors would save approximately 0.44% of all the electrical energy consumed in the US. Additionally, approximately 6% of the energy generated in the US is lost in transmission and distribution based on the EIA (the U.S. Energy Information Administration) and the loss can be greater than 15% in underdeveloped countries. Reductions in energy loss on energy transformation devices like magnetic transformers and electrical motors could save millions of dollars to the country and could also represent an important reduction of CO_2 emissions for the planet since less electrical power would be needed to satisfy the current power demand.

Energy losses in magnetic transformers can be classified as due to winding resistance, core losses, and flux leakage. On the other hand, electrical motors have additional losses, which include stator and rotor resistance losses, frictional losses, and stray load losses. Independent of the type of electrical machine, core losses are one of the dominant components that determine the efficiency of an electrical motor and a magnetic transformer [2]. Core losses directly relate to the magnetic properties of the materials used to build the magnetic core of these devices. Laminated soft magnetic materials are used to build the magnetic cores of electrical motors and magnetic transformers.

Electrical steel or iron-silicon (Fe-Si) alloys are the most used type of soft magnetic alloy. These type of alloys are characterized for having a high magnetic efficiency (low core losses, and high permeability) and they are produced in the sheet form to reduce deleterious eddy current losses [3], [4]. The eddy current losses are one of the so-called core losses. Moreover, the eddy current losses become the predominant source of energy lost in high-frequency applications (above traditional 50-60 Hz). Thus, one significant way to reduce core losses is by reducing eddy current losses, and this can be achieved by increasing the electrical resistivity of the soft magnetic material and by reducing the thickness of the electrical steel sheet. Silicon is a key component to the outstanding magnetic performance of electrical steels. There is extensive research that proves all the benefits that silicon has in the electrical steel magnetic performance, but it is also well known that silicon markedly deteriorates the workability of these alloys. For years, Fe-6.5Si wt% (12.1Si at%) has proved to be the most efficient electrical steel alloy in terms of magnetic permeability,

magnetostriction, and core losses. However, silicon has such a dramatic detrimental effect on the workability of these alloys that the traditional rolling industry limits the content of silicon under ~ 3.2wt% (6.2-6.7 at%) to avoid material cracking during cold deformation.

This workability issue has been under the research radar for years, and investigators have proposed several ideas to solve this problem. Probably the most outstanding effort, in terms of processing, has been the production of Fe-6.5Si wt% sheets by chemical vapor deposition (CVD) coating of silicon on the cold-rolled 3.2%Si sheet, followed by diffusion annealing. However, despite the several alternative methods, there has not been an impact in the production industry mainly because of the considerably higher costs compared to traditional rolling [5]–[12]. One recent effort to overcome this workability issue has been the use of machining-based processes to manufacture Fe-Si alloys. Free machining (FM) and Hybrid Cutting Extrusion (HCE, also previously known as LSEM–Large Strain Extrusion Machining) are manufacturing technologies which have proved the feasibility of machining processing to produce strips of low-workability alloys [13]–[15], and there is sufficient literature that explains in detail the mechanics of FM and HCE [16]–[19].

Problem statement

The detrimental workability effect of silicon restricts the maximum potential of Fe-Si alloys for commercial applications. This thesis approaches this problem via two different ways:

1. Develop a new electrical steel alloy with magnetic performance similar to Fe-6.5Si wt%, but with better workability.
2. Produce strips of the new alloy using hybrid deformation processing.

The first approach taken in this work to optimize electrical steel while taking care of workability issues is based on the idea of substituting some silicon with chromium. This elemental substitution aims to obtain an alloy with outstanding magnetic performance, but with improved workability as opposed to Fe-6.5Si wt%. The idea of using chromium as a substitute of silicon comes from the fact that this element has a significant effect on the electrical resistivity of iron, which is a key parameter to control eddy current loses especially for high-frequency applications, but the strengthening effect of chromium on iron compared to silicon is rather low [20]–[24]. The second approach of this research work is to use hybrid deformation processing, FM and HCE

combined with light cold-rolling, to produce strips of the new experimental alloy. The combination of these machining-based processes with rolling introduces an alternative manufacturing technique to produce electrical steel sheets.

The goal of this thesis is to resolve the following questions:

1. Can Cr partially substitute Si to obtain an alloy with similar magnetic performance to Fe-6.5Si, but with better workability (cold-rollable)?
2. Can sheet of the high-resistivity electrical steel alloy be produced in thin-gauge forms by the hybrid deformation processing?

The specific objectives are:

1. Develop an Fe-Si-Cr electrical steel alloys with electrical resistivity equal or higher than Fe-6.5Si wt%, but with better workability (cold workable).
2. Study the microstructure development of the hybrid deformation process on the Fe-Si-Cr experimental alloy.
3. Scale up the hybrid deformation processes to produce strips of Fe-Si-Cr experimental alloy up to 50 mm in width.
4. Produce Fe-Si-Cr sheet with outstanding magnetic performance (core loss reduction compared to commercial benchmark Fe-3.2Si wt% or M19)

2. BACKGROUND AND LITERATURE REVIEW

2.1 Plastic deformation and slip systems

Plastic deformation has many definitions, they vary depending on the scale and materials. For metals, at the atomic scale, plastic deformation is defined as the motion of several dislocations towards a similar direction. Dislocation keeps moving towards the surface, and when they reach the surface, they leave a step at the atomic level. When this process repeats for millions of dislocations, it yields deformation at the macroscopic scale. The dislocation density is the total dislocation length per unit volume, or it can also be explained as the total dislocations lines per unit are of surface. On metals, dislocation density is usually around $10^8 \mathrm{cm}^{-2}$ [25]. Although dislocations are the key to plastic deformation, having too many dislocations is not beneficial to the deformation ability (or workability) of a material. A dislocation line has a stress field around it. Two dislocations that interact via their stress fields can inhibit one each other. This becomes inevitable when the dislocation density is high ($10^{12} \mathrm{cm}^{-2}$), which it is what happens when a material is plastically deformed. In other words, as metals are plastically deformed, they continuously lose the ability to keep deforming.

Dislocations do not have the same mobility in all directions. There are preferred planes and directions (inside those planes) for dislocations to slip. Dislocations follow these patterns to maintain the stress fields to a minimum, thus reducing internal energy. The unification of these slip planes and slip direction is called the slip system. The slip system of each crystalline material depends on the material crystalline structure. Consequently. The slip systems for FCC, BCC, HCP are all different.

A slip plane is the plane with the highest density of atoms for a specific crystal structure, i.e., the crystallographic plane that has the highest packing density. Similarly, a slip direction is the direction within the slip plane with the highest atomic density, i.e., the crystal direction that crosses the most atoms inside the slip plane. Table 1 shows the different combinations of slip planes and directions for the main crystal structures [26]–[28].

Table 1 Slip systems for FCC, BCC, and HCP structures.

CRYSTAL STRUCTURE	SLIP PLANE	SLIP DIRECTION	NUMBER OF SLIP SYSTEMS
BCC	{110}	$<\bar{1}11>$	12
	{211}	$<\bar{1}11>$	12
	{321}	$<\bar{1}11>$	24
FCC	{111}	$<\bar{1}\bar{1}0>$	12
HCP	{0001}	$<11\bar{2}0>$	3
	$\{10\bar{1}0\}$	$<11\bar{2}0>$	3
	$\{10\bar{1}\bar{1}\}$	$<11\bar{2}0>$	6

Materials that have many slip systems can withstand more plastic deformation, that is why for HCP the ability to plastically deform is poor, i.e., HCP metals have poor **workability**.

2.2 Workability and rolling

In metals, workability is the ability of a material to withstand plastic deformation without fracture or other defect formation. The workability of a metal is especially useful in bulk processing operations like forging and rolling. In metals processing, this term is key because of the role it takes to determine how difficult something will be to manufacture. For example, electrical steel with good workability can be produced by traditional rolling, which is a manufacturing process that produces massive amounts of sheet at a considerably low cost compared to more specialized techniques. On the other hand, low-workable electrical steel alloys (like Fe-6.5Si) cannot be manufactured by traditional rolling and it requires more specialized techniques like PVD and diffusion, or rolling-casting. As a result, Fe-6.5Si sheets are much more expensive.

This workability issue for electrical steel alloys is the fundamental problem that this thesis work addresses, and it is studied around the world by different researches. Many investigators work to find ways to manufacture sheets of these low-workable alloys. Here are some examples found in the literature, just to mention some [3], [5], [14], [21], [22], [29]–[31].

The workability of a metal is not an intrinsic material property. In fact, workability depends also on the production process parameters like geometry, strain, strain rate, temperature, and friction. Additionally, material parameters like microstructure and texture influence the workability. One can say that workability is a property of the material-process system [32], [33],

because it is the interaction of these two what determines the workability. Some experts in the topic claim that “if the forming limit shall be determined for a given metal forming process under given conditions, a testing method which simulates this process should be used” [34]. In other words, to test the workability of the experimental alloys in a rolling operation, the testing method should be a simulation of the real process. Defects typical of poor workability during rolling operation are alligator cracks, surface cracks, and edge cracks.

2.3 Electrical steel

2.3.1 Electrical motors and magnetic transformers

Before diving into all the technicalities of electrical steel, let us establish a context that will help understand the importance of these alloys. Electrical motors and magnetic transformers are present in almost any electric machine. These two apparatuses are key components for the industrial and residential facilities, i.e., electrical motors and magnetic transformers are massively used throughout the entire world.

Figure 1 is a very simplified schematic of the magnetic transformer. In the most simplistic and fundamental way, a transformer works by having an alternating current traveling through a winding 1 that creates an alternating magnetic field. This magnetic field induces an alternating current in winding 2, and the differences between current 1 and 2 will depend on the number of turns in each winding.

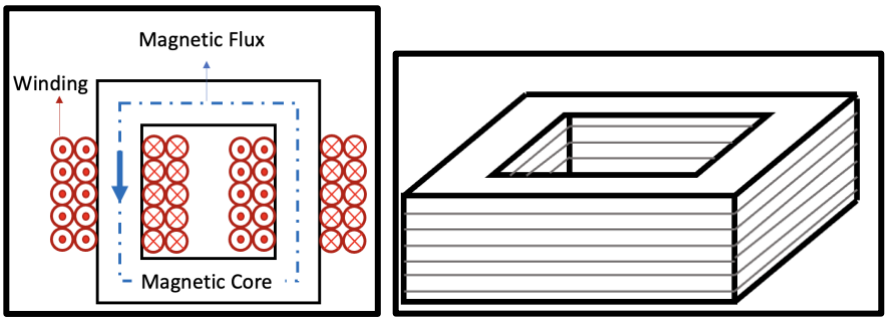

Figure 1 Basic schematic of a magnetic transformer (left) and a magnetic core (right).

Magnetic cores are made of stacked sheets of soft magnetic materials and are used on electromechanical and magnetic devices with alternating magnetic fields like electric motors and magnetic transformers. Magnetic cores are used to confine the magnetic flux, and to strengthen the magnetic fields produced by an electromagnetic coil, thus magnetic induction improves.
Magnetic core losses represent a big component of the total energy loss of transformers and electric motors. Some studies have reported that, in electrical motors, core losses can reach >20% of the total loss [2]. On the other hand, the distribution energy loss of transformers depends on the load applied to the windings, and in cases of low load, core losses dominate the total loss distribution of these transformers.

Naturally, one significant way to improve the efficiency of electrical motors and magnetic transformers is by reducing core losses, which can be done with the use of more efficient soft magnetic materials [35], [36].

2.3.2 Soft magnetic alloys

Soft magnetic alloys are characterized for having a high magnetic permeability and flux saturation, and a low coercivity, core loss, and magnetostriction. These magnetic properties are key for the efficiency of conversion of magnetic transformers and electrical motors. Soft magnetic alloys can be divided into four main categories: permalloys (nickel-iron), soft ferrites, nanocrystalline or amorphous alloys, and the more traditional **electrical steel alloys** (Fe-Si). Although nanocrystalline alloys are the most efficient type engineered so far, electrical steel is the material that still dominates the market because of the large capital investment that would be required to switch to these alternative more efficient alloys, and because of the low cost of Fe-Si materials.

2.3.3 Electrical steel / Fe-Si alloys

Electrical steel is a widely used material in the power transformation industry and can be found as grain oriented (GO) and non-grain oriented (NGO) grades. These alloys are characterized for having a high magnetic efficiency (low core losses, and high permeability) and by being produced in thin sheet forms for lamination to reduce eddy current losses [3]. One reason for the

outstanding magnetic properties of electrical steels is the addition of silicon as an alloying element. There is extensive research that proves all the benefits that silicon adds to the electrical steel performance, but it is also well known that silicon markedly deteriorates the workability of these alloys. For years, Fe-6.5 Si wt% has proved to be the most efficient electrical steel alloy in terms of core losses and permeability, but the workability detriment of silicon is such that the traditional rolling industry keeps the content of silicon under ~ 3.2 wt %. Figure 2A is a graph widely distributed by JFE-Corp that depicts the silicon effect on core loss and magnetostriction for pure Fe. Also, Figure 2B shows what occurs to a Fe-6.5Si wt% sample after withstanding less than 5% cold-work.

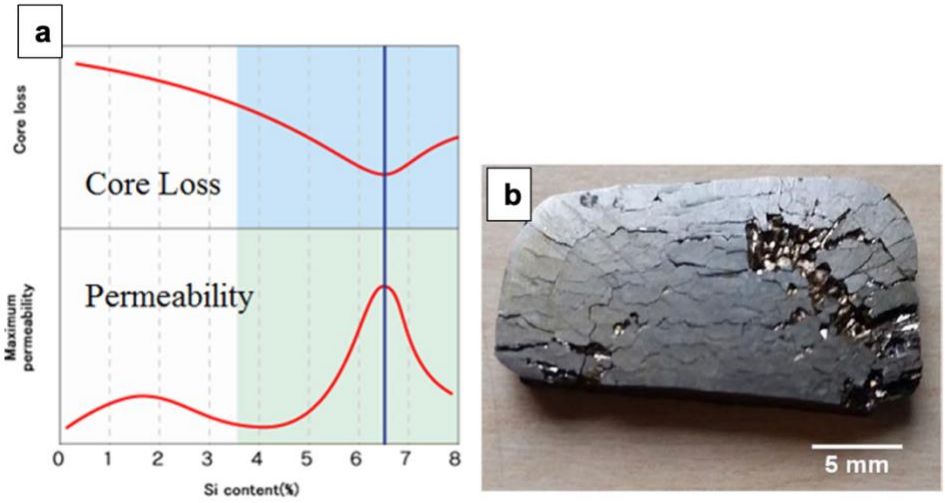

Figure 2 A) Effect of Si on the core loss and permeability for pure Fe. Graph presented by JFE-Steel Corp., B) Fe-6.5Si wt% cracked sample after even light cold rolling (after [14], with permission from Elsevier).

For many years, researchers have worked on different ideas to overcome this workability issue. Probably the most outstanding effort in terms of processing has been the production of Fe-6.5Si wt% sheets by CVD coating of cold-rolled 3.2Si wt% sheet with silicon and diffusion annealing, but despite the several alternative methods there has not been a considerable impact in the market mainly due to increased costs of these alternative production processes [5]–[8], [10]–[12], [37].

2.3.4 Why Fe-Si?

A soft magnetic alloy is a material that is characterized with a high magnetic permeability and flux saturation, and a low coercivity, core loss, and magnetostriction. Pure iron excels at some of those requirements, especially for its high flux saturation of 2.158 T (21.58 kG) [38]. One property that pure iron does not excel at is electrical resistivity (9.8 $\mu\Omega \cdot$ cm). The importance of electrical resistivity is related to the eddy current losses. The magnetic core losses will be further elaborated later in this document, but as a rule of thumb, the higher the electrical resistivity, the lower the eddy current losses. Besides high electrical resistivity, soft magnetic materials for electric motors and magnetic transformers application are required to be thin. Commercial electrical steel thickness traditionally ranges between 0.36 - 0.64 mm, but recently ultra-thin electrical steel (<0.36 mm) has gained popularity in the market because of its good performance in high-frequency applications. Iron workability excels compared to any other soft magnetic alloy, making it relatively easy to process by rolling into thin sheet on a massive scale.

Despite the good magnetic properties of iron, commercial electrical steel is usually a combination of >96Fe wt% in addition to other elements. Silicon is the main alloying element of traditional electrical steel. The benefits of silicon for the soft magnetic properties of iron are: a dramatic increase in electrical resistivity, lower magnetostriction, lower core losses, and a higher magnetic permeability [38], [39]. Besides the magnetic properties, other benefits of silicon are a reduction of the gamma loop of iron, enabling more precise control of microstructure development during processing. Also, silicon benefits the development of preferred orientation, which is ideal considering that the easy direction of magnetization of iron is [001]. Figure 2A shows the effect of silicon on core losses. As depicted by Figure 2A, Fe-6.5Si wt% is the most efficient composition. Also, Table 2 shows the composition effect on core loss and peak permeability for a range of commercial electrical steels.

Table 2 Electrical steel commercial alloys. Composition effect on core loss and peak permeability, data obtained from [38].

AISI TYPE	Si+Al wt%	MAX CORE LOSS AT 60HZ AND 1.5T (W/kg)	RELATIVE PEAK PERMEABILITY AT 60HZ AND 1.5T
M47	1.05	8.38	1300
M45	1.85	6.39	1250
M43	2.35	5.07	1100
M36	2.65	4.52	930
M27	2.80	4.19	870
M22	3.20	4.08	750
M19	3.30	3.83	660
M15	3.50	3.70	375

However, silicon has a detrimental effect on the workability of iron. This is probably the biggest challenge the electrical steel community has been trying to resolve for the past 50+ years. Commercial production of Fe-Si alloys are limited to Fe-3.2Si wt% because the traditional rolling production is incapable of processing the higher concentrations of silicon. Silicon has a potent strengthening effect on iron that has been widely documented. Although strengthening does not have a direct relationship to ductility, it is usually the case that a stronger and harder material will have a lower workability. This relates to the presence of crystalline defects and their effect on dislocation motion.

There is another phenomenon that impacts the workability of electrical steel. Figure 3 is the Fe-Si phase diagram. Using this diagram, one can appreciate what happens to the crystal structure as Si% increases. Fe-Si system undergoes a continuous order-disorder transformation from α-Fe to α_2. In the α_2 region, there is a presence of B2 and $D0_3$ brittle phases. This has a dramatic effect on the alloy workability [40], [41]. This ordering effect relates to the change on the preference of silicon to pair with iron, i.e., as silicon content increases, it is more energetically favorable to form these ordered phases than having Si distributed around the α-Fe matrix randomly. Another important part of this phase diagram is that one can see the effect of silicon on the Fe gamma loop as it was mentioned before. Above approximately 2Si wt%, it is possible to do any type of heat treatment while always maintaining the BCC structure [42]–[44].

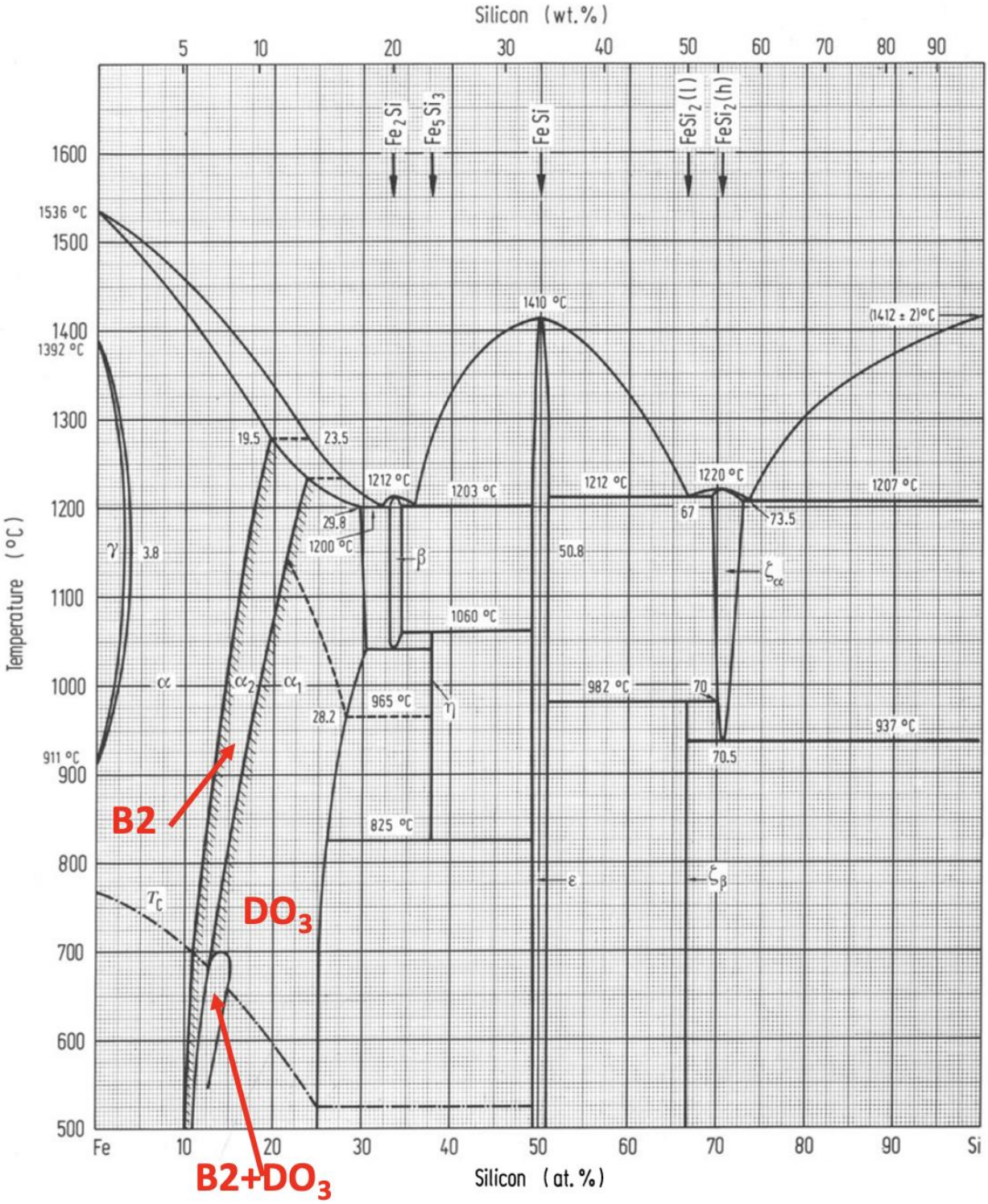

Figure 3 Fe-Si Phase diagram (after [45], with permission from Springer).

Alloy impurities such as carbon, oxygen, nitrogen, and sulfur are commonly found in steel. Electrical steel is not the exception, and the electrical steel manufacturers have to manage the deleterious effects of the impurities. Carbon is especially detrimental to the magnetic properties of Fe-Si steels. Figure 4 shows the effect of carbon on the hysteresis core loss of unalloyed iron. This figure shows that C% has a detrimental effect on the core loss of iron, and that there is a significant drop from about 0.01 to 0 C%. Very small concentrations of carbon can influence the magnetic properties of iron. At C% above the solubility limit on iron at room temperature, carbon will form carbides and precipitate into very small particles. These particles restrict the movement of the magnetic domains, thus having a detrimental effect of the magnetic properties. This effect is called magnetic aging. All finished electrical steel products should have <0.003% (30 PPM) to avoid this effect.

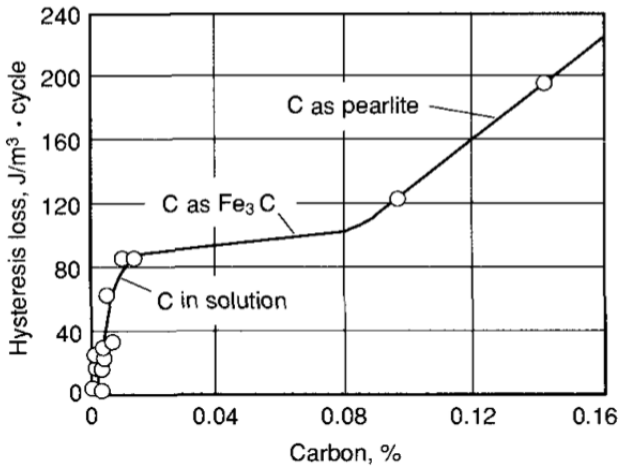

Figure 4 Carbon % effect on the hysteresis loss of pure iron at 1T (from [38], with permission from ASM International).

2.3.5 Alternative techniques to produce Fe-6.5 Si wt%

Fe-6.5Si wt% electrical steel is such a promising material, not only for its high electrical resistivity but also for its very low magnetostriction. Finding alternative ways to produce this alloy has been for years a popular topic for discussion. Many solutions have arisen, but only a few of them have been relevant in the field. Two techniques have been widely discussed, melt spinning and CVD + diffusion. Both techniques proved it is possible to manufacture Fe-6.5Si wt% [11],

[46]–[48]. However, these techniques did not dominate the electrical steel market because of the higher costs of production compared to traditional rolling.

2.4 The relevance of texture

There are 2 types of electrical steels: grain oriented (GO), and non-grain oriented (NGO). GO electrical steels are sheets of metal with a high degree of preferred orientation. Goss texture (named after its inventor N. P. Goss), also called cube-on-edge texture, is the main orientation found in GO steels. This orientation is characterized for having {110} planes parallel to the sheet surface and <001> directions parallel to the rolling direction (RD). Commercial alloys of electrical steel are usually found as BCC - Fe-α, and for this type of crystallographic structure, <001> is the easy direction of magnetization.

Goss textured sheets have considerably better magnetic properties along the RD than the NGO sheets in any direction. However, magnetic properties through any other of the main directions (normal direction [ND] and transverse direction [TD]) would be lower than a NGO sheet. Texture can be defined as the distribution of crystallographic orientations in a polycrystalline material. Percentages of around 40% of the grains oriented in one direction would represent a strong textured material. In the best of the cases, when an effort is made to reduce texture, one can say that this material has a "random" texture. Nevertheless, when a material is processed, there is always some type of remaining preferred orientation coming from the previous manufacturing steps. Thus, it is not accurate to say that a material does not have texture.

GO electrical steels are only used on stationary applications where it is possible to control the magnetic flux path through the rolling direction of the sheets. For rotational application like motors, NGO sheets are preferred. Another popular type of orientation is the cube texture. This orientation is characterized by having {100} planes parallel to the sheet surface and two <001> directions in the sheet plane. This texture is ideal for electrical steel used in rotatory applications. However, it is not widely used because there is no commercial process to produce it at a massive scale.

There are many ways to represent texture in materials, some of them depend on the type of deformation process. Figure 5 shows an example proposed by Suwas & Ray [49]. There are three sheets of metal, each one representing a different level of texture. Figure 5 represents how different

would be a strong textured material compared to a randomly textured sample and a material with 2 texture components. Texture is usually denoted by Miller indices. In rolling, it is necessary to know both which plane of the oriented crystals is parallel to the rolling plane, and which direction of the oriented crystals is parallel to the rolling direction. With wire drawing, it is enough to know the orientation of the crystal's axis relative to the longer dimension of the piece.

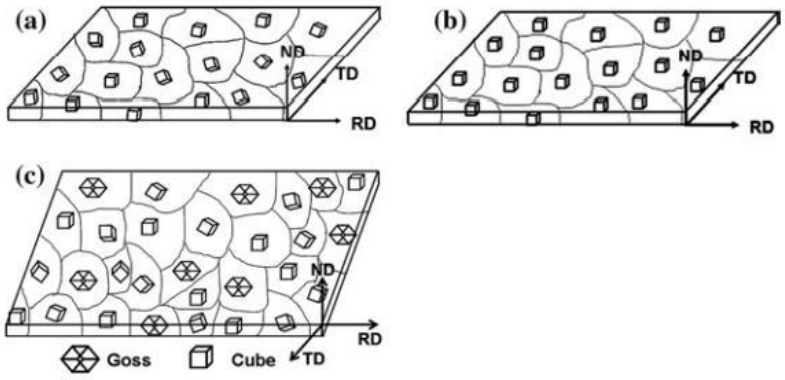

Figure 5 Three sheets of metal depicting a) random texture, b) strong texture with (100) [010] orientation, and c) a material with 2 textures (from [49], with permission from Springer).

The representation of texture gets more complicated when a material has a series of texture components such as $\{h_1 k_1 l_1\}$ $<u_1 v_1 w_1>$, but also $\{h_2 k_2 l_2\}$ $<u_2 v_2 w_2>$,…$\{h_n k_n l_n\}<u_n v_n w_n>$. It is necessary then to include a way to represent the relative intensities of the different orientations, usually expressed as multiples of random distribution (mrd). Stereographic projections of the crystallographic texture, called pole figures, are used to represent texture. Poles figures provide useful information to analyze the texture of materials. Figure 6A is a representation of a Goss textured grain in a sheet. Also, Figure 6B shows the hypothetical (100) pole figure for a 100% Goss textured sample.

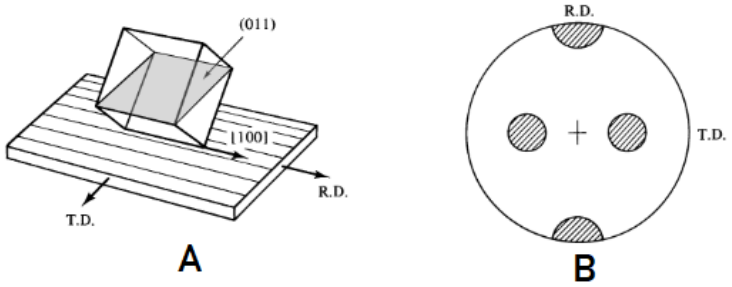

Figure 6 A) Schematic of how a Goss crystal orientates with respect to the sheet main directions, and b) ideal Goss texture on (100) pole figure (from [50], with permission from Wiley).

Nevertheless, pole figures are limited. Poles figures are 2D representations and crystals are 3D shapes. This difference lowers the resolution of the texture information that can be displayed in a pole figure. What has been used to solve this problem is the method called "orientation distribution function" (ODF) [49]. The orientation distribution function (ODF) is a representation of the density of the crystallographic orientations of a material in Euler angles φ_1,Φ, φ_2 as described by Bunge [51]. In a similar way to the contour lines for pole figures, ODF uses contour lines to depict the intensity of the orientation. The ODF is a 3D representation of texture. Usually, φ_2 is fixed at certain angles from 0 to 90° (usually jumping every 5°), thus 2D representations can be evaluated. Regularly, ODFs at $\varphi_2 = 45°$ are the most used ones for steels. Figure 7 shows the ODF section at $\varphi 2$ = 45° for a cold-rolled interstitial-free steel obtained from experimental data, in addition to the representation of the main rolling texture components in the Euler space for $\varphi 2$ = 45°. Cold rolled specimens are usually characterized for the presence of the γ-fiber and the partial α-fiber. The γ-fiber is a continuous series of texture components in the Euler space (φ_1= 0 - 90°, Φ=55°, and φ_2=45°) that are identified for having the <111> parallel to the sheet normal direction (ND), and the crystallographic direction range from $[1\bar{1}0]$ to $[\bar{1}\bar{1}2]$, as shown in Figure 7. On the other hand, the partial α-fiber (φ_1= 0°, Φ=0-55°, and φ_2=45°) is characterized for having the <110> parallel to the rolling direction (RD) and the crystallographic planes range from (001) to (111) as shown in Figure 7. Finally, another important texture is the θ-fiber (φ_1= 0°, Φ=0-90°, and φ_2=45°) which is characterized for having the <100> parallel to the normal direction of the sheet, and the crystallographic directions range from $[1\bar{1}0]$ to $[\bar{1}\bar{1}0]$ as shown in Figure 7. The θ -

fiber is not as common as the other two, but it is more beneficial for the magnetic properties. Also, the θ-fiber is also known as the λ-fiber is some papers.

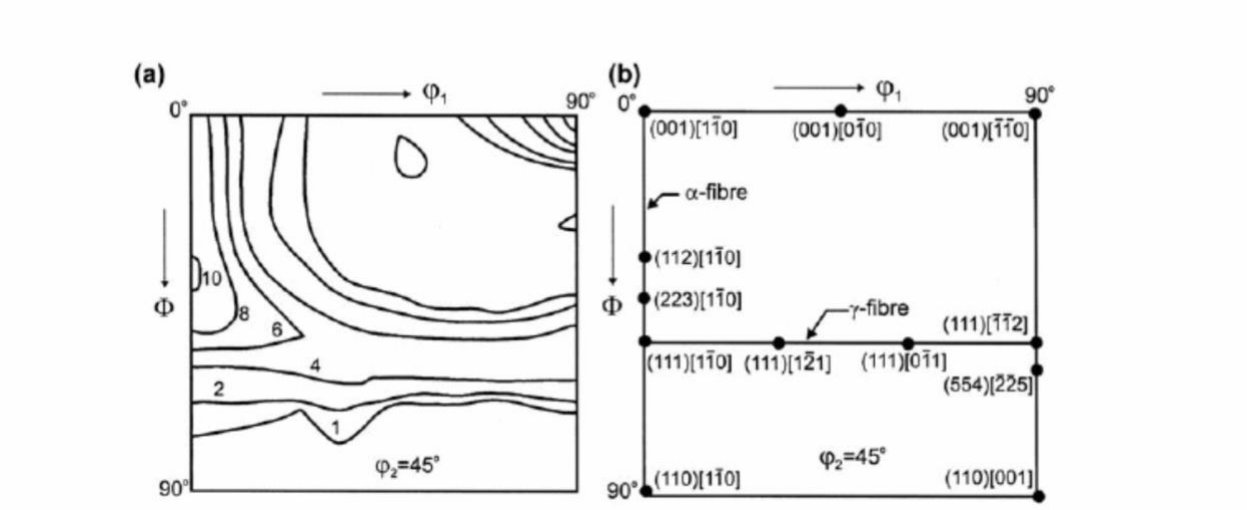

Figure 7 ODF section at $\varphi 2 = 45°$ for cold-rolled interstitial free steel; a) is an example from experimental data, and b) is the representation of the ideal rolling texture component in the Euler space (from [52], with permission from Elsevier).

Finally, it is also possible to represent texture using the electron backscattered diffraction technique (EBSD) to plot inverse pole figure maps. In EBSD, diffracted rays are obtained when an electron beam interacts with a crystalline sample tilted around 70º (more diffracted rays are obtained at this angle). In SEM, when the electron beam interacts with the sample, back scattered electrons are obtained in the process. There is a finite probability that some of these scattered electron beams would interact with the lattice planes of the sample surface at the right angle to satisfy Bragg's law. The satisfaction of this law would lead to a constructive interference, thus producing strong diffracted electron beams that contain all the information about the relationships of the crystallographic planes of the sample (microstructure, orientation, etc.). When a phosphor screen is placed just in front of the sample, a pattern shows up on it. These diffracted patterns are called "Kikuchi patterns". Following this idea, in EBSD millions of data points are collected to construct and inverse pole figure map (IPF map) that will show the orientation of each individual grain relative to the specimen coordinates. Figure 8 shows an example of an IPF map for the RD and the ND for visualization.

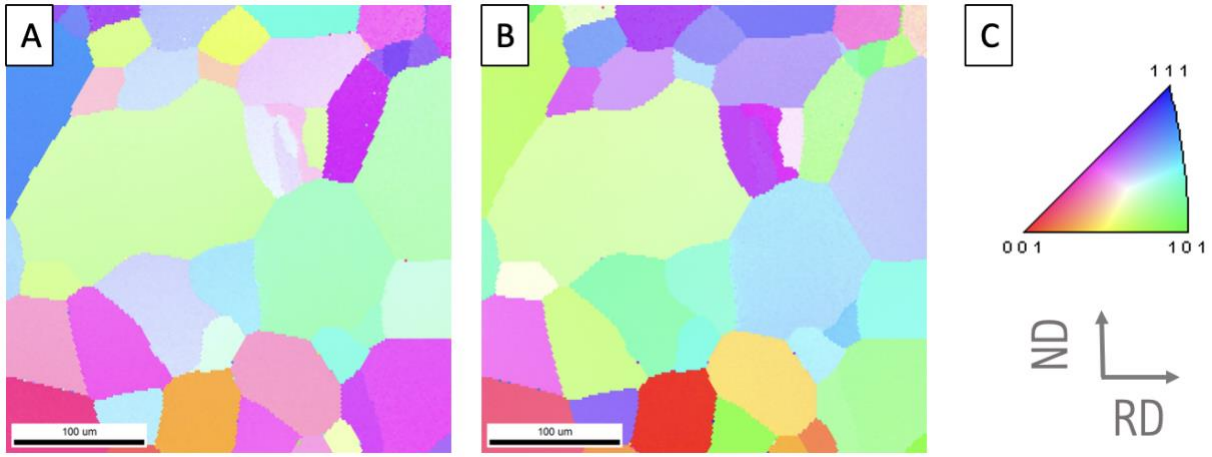

Figure 8 Examples of IPF maps collected via EBSD for electrical steel sample. A) IPF map with crystallographic direction parallel to the RD, B) IPF map with crystallographic direction parallel to the ND, and C) IPF showing the color coding of the EBSD picture.

2.5 Fundamentals of magnetism in electrical steel

There are 5 types of magnetism, ferromagnetic, ferrimagnetic, paramagnetic, anti-ferromagnetism, and diamagnetism. This thesis deals only with ferromagnetic materials.

Ferromagnetism is a phenomenon where materials are attracted to magnets and can be easily magnetized. This behavior is related to iron, cobalt (Co), and nickel (Ni), but it is also possible in their alloys. Additionally, some rare earth elements can be ferromagnetic [53].

Ferromagnetic materials have a unique behavior that explains their ability to be attracted to magnets or turn into a magnet. Ferromagnetic materials have a microstructural feature called magnetic domains. At the atomic level, each atom can be seen as an atomic electromagnet. In ferromagnetic materials, groups of atoms tend to align their unpaired electron spins in the same direction, forming groups of so-called magnetic domains.

Each magnetic domain produces an intense magnetic field, but a polycrystalline material has millions of these magnetic domains oriented in different random directions, which turns into having a demagnetized bulk material. When a magnetic field is applied on a ferromagnetic bulk material, the magnetic domains align with each other “magnetizing” the sample. The difference between a soft or a hard magnetic material is that a soft magnet will be magnetized only in the presence of an externally applied field, while a hard one will have remaining magnetism even after the applied field has been removed.

Fundamental magnetic properties of soft magnetic materials

In this thesis, the author mentioned already what are the magnetic properties for which soft magnetic materials are characterized. As a rule of thumb, soft magnetic materials are known for having high magnetic permeability and flux saturation, and a low coercivity, and core loss. This section will explain in more detail each one of these properties.

Let us talk about the hysteresis loop. Although, it was not mentioned in the previous paragraph as one of the important properties of soft magnetic materials, the hysteresis loop establishes a great common background that can be used to explain and relate almost all the properties.

Figure 9 is a schematic of a basic hysteresis loop for magnetic applications usually known as the B-H loop. For ferromagnetic materials, the hysteresis loop is a consequence of the ability of these materials to have remanent magnetization. To describe the B-H loop, let us assume a material that has not been exposed to an externally applied field, thus it does not have remanent magnetization. This condition locates at the origin of the graph in Figure 9. When an external field H [Oe or A/m] is applied, the material magnetization B [Gausses or T] follow the path "P1" until it reaches B_{sat}, which is the saturation magnetization.

After this point, as H is reduced to zero, B follows the path "P2". As a result, when H = 0, B = B_r. The reason is that when a ferromagnetic material is exposed to an external applied field, the magnetic domains orientate towards the same direction. Once the field is removed, some of these magnetic domains remain in the oriented direction. This phenomenon is known as remanent magnetization or remanence. After this point, if an external field is applied in the opposite direction (negative in the B-H loop) at H_c (or $-H_c$) the magnetization goes back to zero. H_c is known as the coercivity. After reaching - B_{sat}, the external magnetic field is reduced to zero and then it follows path "P3" until reaching B_{sat} again, thus completing the loop.

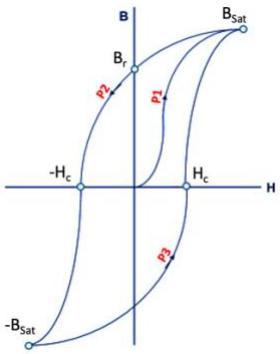

Figure 9 Fundamental B-H loop for a ferromagnetic material.

Thanks to the B-H loop, it is possible to introduce some of the concepts of the magnetic properties. Almost all the remaining properties can be explained as well using the B-H loop. In the following, this section will cover the concepts of the magnetic properties, but in more detail.

- Saturation Magnetization (B_{sat}): This is the maximum magnetization possible for a ferromagnetic material. In other words, it is the state when any increase in H does not represent a significant change in B. This can be seen in Figure 9 where at B_{sat}, the slope of the loop is almost horizontal. The explanation for this phenomenon relates to the magnetic domains. Magnetic domains in a bulk material are like small magnets with different orientations. This makes the total magnetization of a material to be low under no external applied field. As explained before, when an external field H is applied to a ferromagnetic material, the magnetic domains align towards the same direction of H. The higher the magnitude of H, the more the magnetic domains align, thus the higher the intensity of B. The saturation magnetization is the B value where the magnetic domains have aligned the most they can. After this point, any increase in H will not have a significant variation in B because the magnetic domains have reached their limit of alignment. The saturation is material and crystal structure dependent, but also it heavily depends on temperature.
- Coercivity (H_c): The coercivity is the ability of a magnetic material to stay magnetized after applying and removing an external magnetic field. In other words, H_c is the necessary magnetic field to demagnetize a ferromagnetic material (B = 0). In soft magnetic materials, a lower H_c is desired. Figure 9 shows H_c in the B-H loop. The higher H_c (meaning a higher value of H is required to demagnetize the material), the wider is the B-H loop. And as it

will be discussed later in this section, for soft magnetic material the narrower the loop, the better.

- Permeability (μ) : Another term for magnetic permeability is "ease of magnetization". The magnetic permeability is the ability of a material to get magnetized when exposed to an external field. Another definition of magnetic permeability is the ratio of magnetization and external applied field, which can be expressed as $\mu = \frac{B}{H}$. Figure 9 shows that the relationship between B and H is far from linear. As a result, there is not just one single μ for a determined material. There are many ways to the report permeability, and the most popular ways are:
    - B values accompanied by their correspondent H.
    - Maximum permeability μ_{max}, the maximum obtained permeability value from an original demagnetized material.
    - Initial permeability μ_i, the permeability value at low numbers of B, usually under B = 0.1 T.
    - Relative permeability μ_r, this is an extra method to report permeability. It is the ratio of any of the previous mentioned permeabilities and the permeability of free space, $\mu_r = \frac{\mu}{\mu_0}$.
- Core Loss (P_s): Core losses are the energy waste associated with having an alternating magnetic flux traveling through the magnetic core. This energy loss transforms into heat that is conducted throughout the magnetic core. For applications that use soft magnetic materials like transformers and electric motors, losing energy is not a good thing to have. Not only that, losing energy that transforms into heat has a secondary detrimental effect. The heat associated with the loss energy increases the magnetic core temperature, which affects the magnetic performance of the material, especially the B_{sat}. The total core loss has three different components, hysteresis loss (P_h), eddy current loss (P_e), and anomalous loss (P_a).
    - The hysteresis loss is represented by the area enclosed in the B-H plot, which can be described as the energy required to complete on loop of the magnetization cycle. In an ideal soft magnetic material, $H_c = 0$ thus the B-H loop transforms into one

line with no enclosed area. But real ferromagnetic materials present some degree of coercivity, thus the existence of the hysteresis loss.

- Eddy current losses are associated with alternating current (AC) applications. The higher the frequency, the higher the eddy current losses. According to Faraday's law of induction, an alternating magnetic field applied to a metal will induce an electromotive force that can produce significant currents. One of the side effects of magnetizing a magnetic core with an alternating magnetic field H is the production of parasite currents in the core. These currents are called eddy currents and they have a detrimental effect on the magnetic core efficiency. The presence of parasite currents in the core that has a resistance R will dissipate energy as heat and that is called eddy current losses. There are two ways to reduce eddy current losses, increasing the material electrical resistivity and/or building the magnetic core by stacking thin laminations of soft magnetic material with resistive (insulation) barriers in between. Hence the importance of having soft magnetic materials with high electrical resistivity, but also with the ability to form into thin sheets [53].
- Bertotti's model introduced the concept of anomalous losses, as an additional core loss due to domain wall movement. Bertotti's model is widely used to study the core losses of electrical steels [54]–[56].

Equation 2-1

$$P_s = \underbrace{\{C_0 B_m^{\alpha} f\}}_{P_h} + \underbrace{\left\{\frac{\pi^2 d^2 B_m^2}{6\rho\gamma}\right\}}_{P_e} + \underbrace{\left\{C_1 B_m^{3/2} f^{3/2}\right\}}_{P_a}$$

B_m= Max flux Density, f = frequency, d = sheet thickness, ρ = electrical resistivity, γ = material density, and α, C_0 & C_1 are constants characteristic of material obtained via curve fitting.

Knowing three experimental points of the equation is enough to determine unknown constants.

This model is useful when **f > 20 Hz** and **B_m < 1.5 T**

- Magnetostriction: Magnetostriction is one property of the ferromagnetic materials that makes them change their shape when exposed to an external magnetic field. As an alternating magnetic field is applied to a soft magnetic material, the magnetic

domains rotate to align towards the direction of the magnetic field. This rotation generates mechanical strain in the sample. This magnetic property is detrimental to devices like transformers and electric motors. Magnetostriction can create internal friction that can contribute to an increase in temperature. Also, variations in the core's geometry can alter the electro-mechanical design of the device.

2.6 Chromium as an alloying element for soft magnetic materials

Silicon has beneficial and detrimental effects on iron. On one hand, silicon greatly benefits the magnetic properties of Fe. On the other hand, silicon effect on the workability of iron inhibits industrial production of the most efficient alloys. The electrical resistivity of the alloy is a key parameter to the reduction of core losses in a magnetic core. The electrical resistivity is directly related to the eddy current losses (see Equation 2-1), which at high frequencies become the predominant source of energy lost (above traditional 50-60 Hz). Thus, one significant way to reduce core losses is to increase the electrical resistivity of electrical steel.

Figure 10 depicts the effects of different alloying elements on the electrical resistivity of iron. In the wt % figure, silicon has the greatest effect of all the elements; this is expected, since one effect of silicon in iron is having a considerable reduction in the eddy current losses. However, Figure 10 shows that other elements can increase the electrical resistivity of iron as well. For example, aluminum has an outstanding effect on the electrical resistivity of iron. In fact, aluminum is widely used as a partial substitution of silicon, although Al wt% is kept below 2%. It has been proved that the lowest core loss for the Fe-Si-Al system [24], [57] is obtained in below 2Al wt%. Also, despite the potential of aluminum, the extra challenges during processing and increased costs have stalled the usage of aluminum as a substitution of Si [22], [58]. On the other hand, in the atomic % graph, tin has the greatest effect on the electrical resistivity of iron. This difference is due to the higher atomic weight of tin compared to the other elements. There are no other significant changes in the order of the other elements. However, the at% graph shows that the difference in resistivity effect of Cr compared to Si and Al is not as high as it is shown in the wt% graph. This is important because it is the at% of Fe what determines the maximum flux density of the alloy, and this is used as one of the design restrictions to develop new electrical steel alloys.

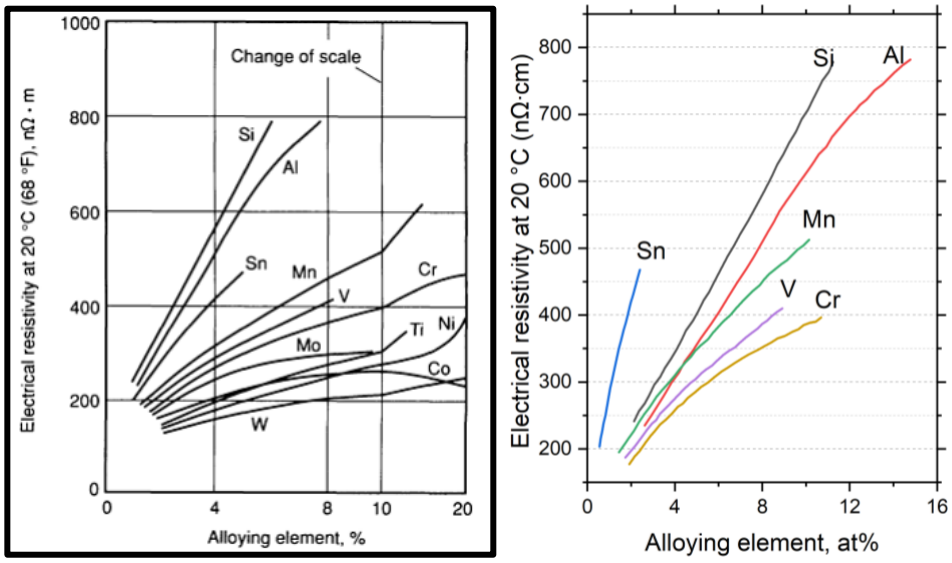

Figure 10 Effect of alloying elements on electrical resistivity of Fe. To the left, alloying elements in wt% (from [38], with permission from ASM International). To the right, adaptation showing alloying element in at%.

This thesis focuses on chromium. Chromium is not at the top of the list of the elements with the greatest effect on the electrical resistivity of iron. However, the reason this work finds chromium so attractive is the almost nil strengthening effect of chromium on iron. Figure 11 from [59] is a graph that shows the strengthening effect of different alloying elements on iron out to large plastic strains produced by wire drawing. Figure 11 shows how low is the strengthening effect of chromium on iron compared to other elements like silicon. The combination of the data collected in Figure 10 and Figure 11 is a good lead to believe that chromium could be an alloying element with great effect on materials resistivity but a low effect on workability.

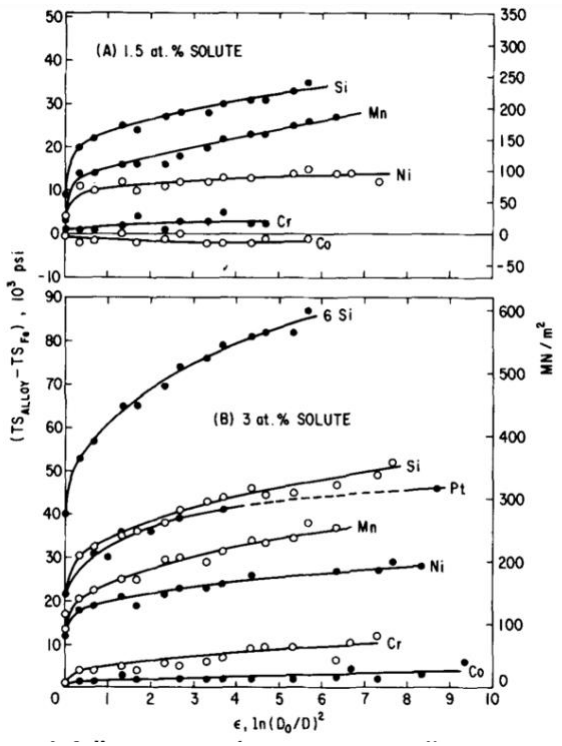

Figure 11 Effect of different alloying elements on the tensile strength of iron as a function of wire-drawing strain. (A) 1.5 at. pct solute, (B) 3 at. pct solute (from [59], with permission from Springer).

Figure 12 is the Fe-Cr phase diagram. This binary system is characterized by having an FCC-gamma loop that stops at 13Cr wt%. Another important characteristic of this system is the presence of an intermetallic σ phase. The σ phase is not of interest for this work because of the high Cr wt% at which it forms. At lower temperature there is a miscibility gap between the α' (iron BCC) and the α'' (Cr BCC) phases.

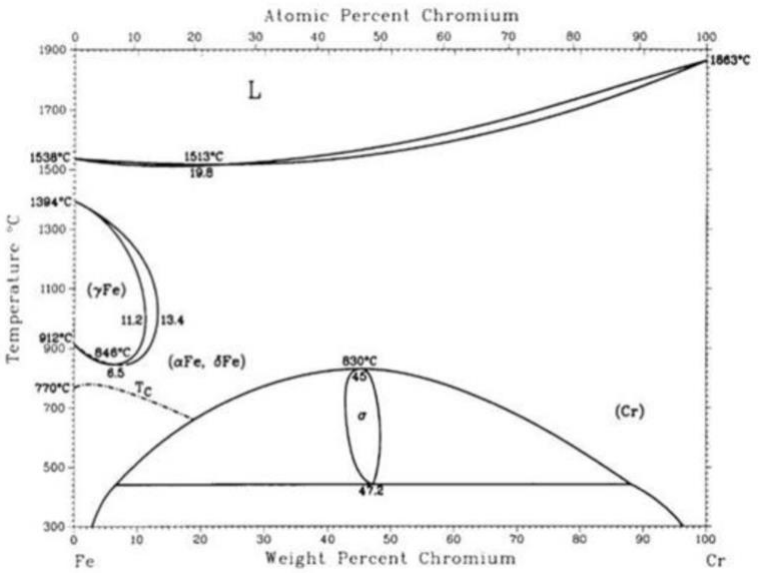

Figure 12 Fe-Cr phase diagram (from [60], with permission from ASM International).

For this project, it is useful to look at the Fe-Si-Cr ternary diagram, since this thesis is looking at the possibility of substituting some Si with Cr in electrical steel alloys. Figure 13 shows the iron-rich corner for the Fe-Si-Cr ternary phase diagram at 600 °C, which it is of interest because of the proximity to actual heat treatment temperatures for electrical steel sheet. This ternary phase diagram shows compositional boundaries for the ferrite phase region of the Fe-Si-Cr system. The graph shows that alloys up to approximately 10Si and 25Cr at% sit within the α region, which is ideal for magnetic properties.

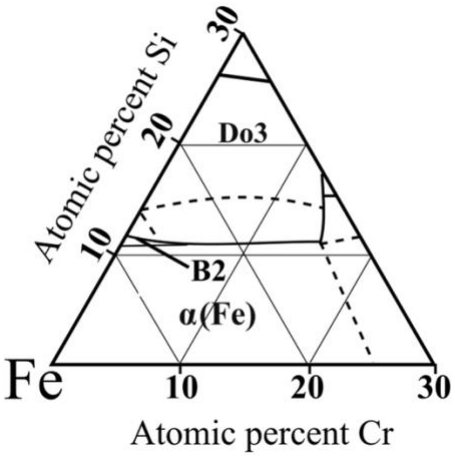

Figure 13 Fe-Si-Cr ternary phase diagram for the iron rich corner at 600 °C (from [61], with permission from Springer).

2.7 Fundamentals of machining-based sheet production

The following section explains the mechanics of free machining (FM) and hybrid cutting extrusion (HCE). These two processes are machining-based techniques, and in combination with rolling, they will be used in this work as alternative manufacturing methods for electrical steel processing. FM and HCE have been used to prove the feasibility of machining process to produce strips of low-workability alloys [13]–[15], and there is an extensive literature that explains in detail the mechanics of FM and HCE [13], [15]–[19], [62]–[64].

2.7.1 Mechanics of FM and HCE Overview

Figure 14 is a schematic of strip production via free machining (FM). FM is a plane strain machining-based process to produce strips (usually metallic) in a single step. Figure 14 shows a workpiece that is rotating at a constant surface velocity V_0. A sharp cutting tool with a rake angle α engages the rotating workpiece at a preset depth t_0, which is also called the undeformed chip thickness. As the cutting tool engages the workpiece, a continuous chip of metal with deformed chip thickness t_c is produced. This strip shaped chip forms due to the intense and localized shear strain that happens within a narrow deformation zone A-B. This deformation zone can be idealized as a shear plane due to its small width of ~100 μm [14], [62]. Since there is no constraint on the upper face, the material is free to flow, which causes the strip to have a rough top face (free face),

and in contrast, the face in contact with the cutting tool (rake face) is characterized as smooth. FM strips can be lightly rolled in order to improve their quality and make their surface roughness comparable to a traditionally rolled sheets [65], [66]. CFD means chip flow direction, and ND is the normal direction of the strip surface.

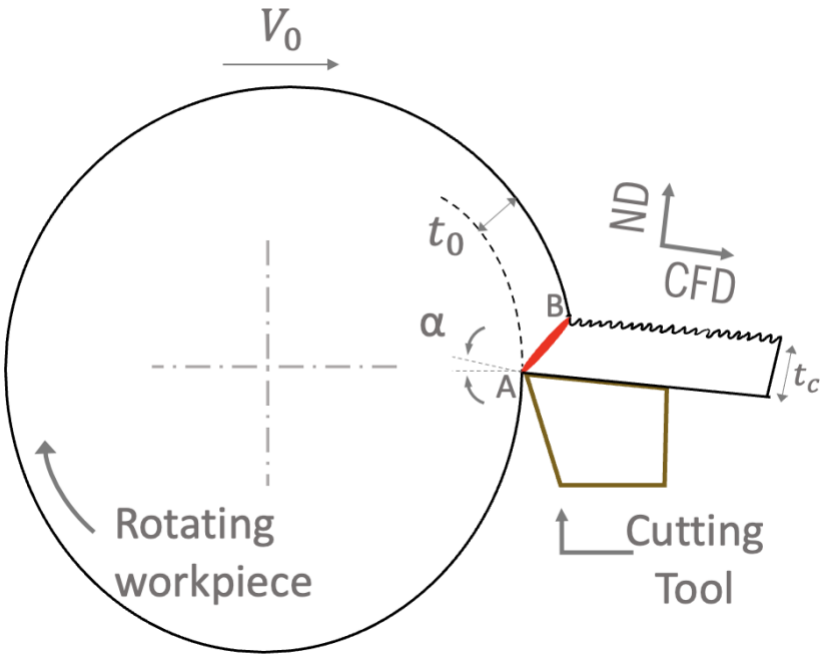

Figure 14 Schematic showing strip production via FM+Rolling.

Similar to FM, Figure 15 shows the schematic for strips production via HCE. The fundamentals are the same as in the FM system, but with the addition of a constraining tool as it is shown in Figure 15. The constraining tool is intended to transform the machining-based process into a hybrid cutting-extrusion process. The combination of elevated hydrostatic pressure, intense and localized shear strain, and adiabatic heating lead to the suppression of the mechanisms that cause cracking on low workability alloys, which is one of the great features of this manufacturing process. Setting the gap between the cutting and the constraint tool allows control over the deformed chip thickness. Hence, HCE allows for more control over the deformation process than FM, producing a continuous strip with a defined final geometry and with surface roughness on both faces comparable or superior to traditional rolling[14], [17], [19], [64]

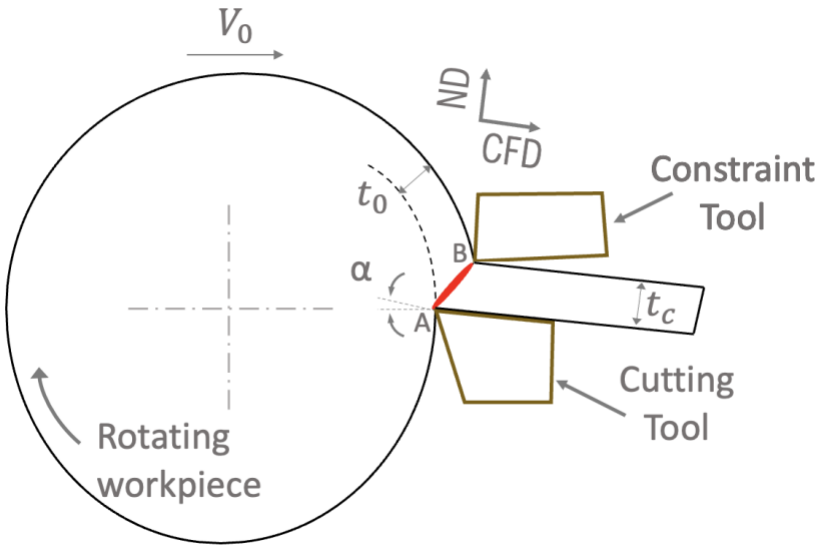

Figure 15 Schematic of strip production via HCE.

Two key parameters of FM and HCE to suppress workability issues are the confined and high strain, as well as the adiabatic heating. The following section describes the mechanics of these two phenomena.

2.7.2 Deformation strain, and adiabatic heating

Previous works used PIV (particle image velocimetry) to plot the deformation field on HCE [16]–[18]. These studies reported intense, confined, and uniform shear strain within a narrow deformation zone A-B that extends from the cutting tool to the constraint tool as shown in Figure 14 and Figure 15. Because of this narrow deformation zone, it is reasonable to idealize it as a shear plane, thus allowing for the definition of effective strain as:

Equation 2-2

$$\varepsilon = \frac{1}{\sqrt{3}}\left(\frac{\lambda}{\cos(\alpha)} + \frac{1}{\lambda \cos(\alpha)} - 2\tan(\alpha) \right)$$

having $\lambda = \frac{t_C}{t_0}$ and α = rake angle [14], [17], [18]. Figure 16 is a graphical representation of Equation 2-2, and it shows how the effective strain changes as a function of lambda for three different set rake angles. The minimum effective strain point is always located at $\lambda = 1$, no matter

α, i.e., as λ moves away from 1 in either direction ε increases. This increase in ε influences the final microstructural condition of the strip. The lower limit for λ is based on the machine capabilities, while the upper limit is defined by the working material.

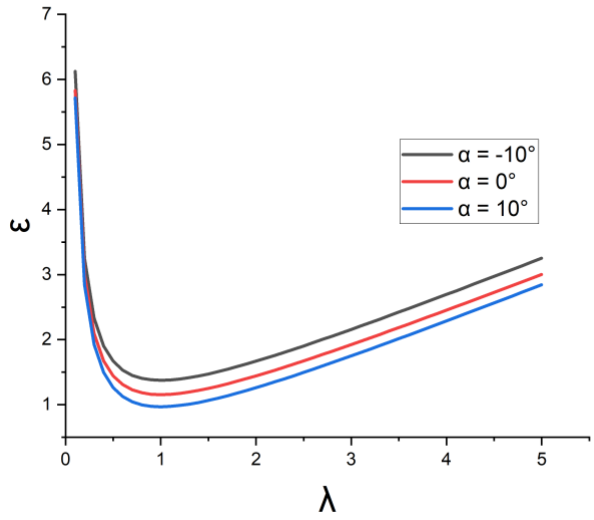

Figure 16 Effective strain as a function of λ and α.

One great feature of strip production via FM/HCE is having the possibility of varying the deformation path by setting different λ or α. Changing the deformation path in machining allows one to control the shearing path during deformation, meaning that one has control over the final microstructure of the strips. This is important because of the relationship there is between deformation path and the microstructure texture. FM/HCE make possible production of strips with shear textures, which is not possible with traditional rolling [65]. Figure 17 depicts how the deformation path changes as a function of λ. In addition to the deformed chip thickness, λ also changes the angle of the shearing zone (deformation path). More details and examples about this feature will be shared in the results section.

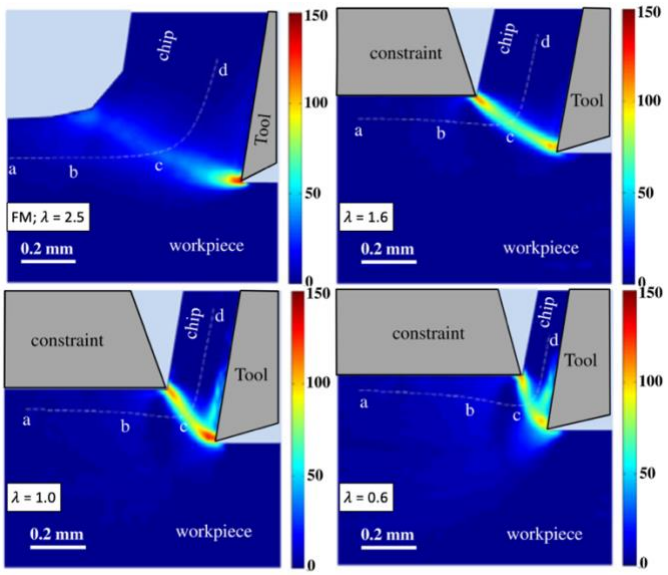

Figure 17 Strain rate fields showing deformation path by PIV analysis of strips produced via machining for $\lambda = 0.6 – 2.5$ (from [67], with permission from Elsevier).

Additionally, during HCE and FM chip formation there is heat generation due to the plastic deformation of the process. The shear plane model allows one to predict the strip temperature in the narrow deformation zone, and it can be calculated as:

Equation 2-3

$$T = \frac{(1-\Gamma)U_s}{\rho c} + T_0$$

with Γ as the fraction of heat going into the workpiece, U_s as the specific shear energy of chip formation and is measured from cutting forces, T_0 as the initial temperature, ρ as the density, and c as the heat capacity of the workpiece. All parameters of Equation 2-3 have been extensively explained in previous works, and the increase of temperature in the strip due to adiabatic heating is usually located between 200 – 500 °C [14], [18]. Such adiabatic heating can have dramatic effects on the strip microstructure, leading to phenomena like dynamic recrystallization, creating unique as-deformed microstructures.

3. HIGH-RESISTIVITY ELECTRICAL STEEL – DEVELOPMENT OF AN EXPERIMENTAL ALLOY

This chapter focuses on the development of a new experimental alloy to substitute the well-known high performance of Fe-6.5Si. The goal is to obtain an alloy with the high resistivity of Fe-6.5Si (**at least 80 μΩ·cm**) but better workability for sheet production. The dramatic effect of Si on the loss of ductility in iron is well known. In general, this poor ductility (workability) above about 4% Si has been attributed to a B2 ordering due to the dissociation of superlattice dislocations induced by the high Si amounts in the material [68]. Silicon is the most potent alloying element to increase the electrical resistivity of iron. However, other elements like aluminum and chromium are also effective alternatives [69], [70]. Moreover, Fe-Al and Fe-Cr phase diagrams show that other than the gamma loop typical of iron alloys, there is no other type of ordering or phase transformation up to 10 wt% for the Fe-Al system and more than 20 wt% for the Fe-Cr system. In fact, previous studies have demonstrated that if the correct thermomechanical procedure is followed (hot rolling down to 1 mm + cold rolling), thin sheets of Fe-Si-Al alloys can be produced. However, there is no solid agreement about how much Si+Al can be added and still maintain good cold workability, i.e., before the alloy gets too brittle. Some authors claim that Si+Al has to be lower than 3.5 wt%, but some others say that even Fe-6.5(Si+Al) is possible if the correct procedure is followed [22], [71], [72]. Information about the workability of alloys in the Fe-Si-Cr system is limited, as is any type of resistivity information about this alloy.

3.1 Experimental methods

3.1.1 Materials for alloy selection experiments

Fe-3Si-3Al and Fe-4Si-4Cr (wt%) samples were produced in-house in order to control the purity of the alloy. The rationale for the selection of these two specific alloys is in section 3.2. High purity elemental metals used to manufacture the alloys had compositions in wt.% as follows: Fe 99.98%, Si (>99.999%), Cr 99%, and Al 99.99%. The experimental alloys were made using an arc melter with a non-consumable tungsten electrode on a water-cooled copper hearth. The alloys were melted under flowing 99.99% Ar, and they were turned over and re-melted three times to

obtain button shaped samples with good homogeneity. The button samples were approximately 50 g, diameter of 4 cm, and thickness of 1.5 cm approximately. The buttons were hot rolled to ~1 mm thickness, and then cold rolled down to the limit of the mills (~200 μm) to produce thin strips ~10 mm wide. The samples were heated in a box furnace in air up to 800 °C for 10 min before the first pass and in between all the passes during hot rolling. Samples were polished after hot rolling and before cold rolling to remove the small amount of oxidation.

3.1.2 Materials for workability experiments

Fe-3.2Si and Fe-1Si wt% materials were obtained from AKSteel and Nucor in the as-hot rolled and the as-cast conditions, respectively. The Fe-4Si-4Cr alloy for the workability experiments was obtained in the as-cast condition from Sophisticated Alloys Inc in Butler, Pa. An ingot of 4.3 in diameter and height of 11.5 in (plus hot top) was prepared by VIM and the chemical analysis reported 4.02%Si, 3.88%Cr, and interstitials (C, O, and S) < 100 ppm. The Fe-6.5Si wt% was produced in-house via arc melter with a non-consumable tungsten electrode on a water-cooled copper hearth, using high purity elemental metals Fe (99.98%) and Si (>99.999%). Specimens of each material were manufactured with a geometry of 12 mm width and 8 mm thickness. These specimens were hot rolled at 800 °C to a thickness close to 2 mm using a Stanat rolling mill with 5 in diameter rolls. The specimens were cold rolled to 0.5 mm with progressive reductions of 5%. After every step, specimens were checked for presence of cracks, ripples, or other typical defects in the rolling process.

For metallographic preparation, the as-cast buttons were cut using a wire EDM and the rolled strips were cut with a low-speed diamond saw. Silicon carbide paper with grits from 320 to 2000 were used to grind the samples, with a final polishing using 0.05 μm alumina powder dissolved in water and 0.02 μm colloidal silica. The samples were etched for microstructure examination using 5% nital for the Fe-Si alloys and 40% nitric acid aqueous solution for the Fe-4Si-4Cr alloy. Vickers hardness testing was performed with a load of 500 g (HV0.5) and at least 250 μm distance between indentations. At least 10 indentations were made for each hardness and the values are reported as the mean ± one standard deviation.

3.1.3 Resistivity

Resistivity measurements were done following the 4-wire method of ASTM A712-14 Standard Test Method for Electrical Resistivity of Soft Magnetic Alloys. A multimeter (HP 3468B) measured the resistance of Fe-3Si-3Al and Fe-4Si-4Cr (wt%) strips with a resolution of 1 mΩ, and the geometry of the strip was measured with a Vernier caliper with a resolution of 0.01 mm. Although the conventional standard requires a minimum specimen length of 25 cm, for this study resistivity measurements were observed using shorter lengths due to restrictions on the length of strips that could be produced from the small arc melted buttons. Three measurements at 5 cm, 10 cm, and 14 cm were taken for each strip. Results showed that resistivity values were consistent for strips shorter than 25 cm.

3.2 Alloy selection

In power transformation devices like electric motors and magnetic transformers, core losses are composed of eddy current losses, hysteresis losses, and anomalous losses. Eddy current losses are frequency dependent and can be reduced by increasing electrical resistivity, most effectively through solid solution alloying additions. Whereas hysteresis losses are affected also by microstructure modifications such as grain size, and texture [4], [73]. At frequencies of approximately 50 Hz, the ratio of hysteresis losses and eddy current losses is close to 1:1. The higher the frequency, the higher the eddy current losses compared to the hysteresis losses. The eddy current losses become the predominant source of energy loss in high-frequency applications (above traditional 50-60 Hz), thus the importance of electrical resistivity.

Figure 10 shows the effect of different alloying elements on the electrical resistivity of iron. As expected, silicon has the greatest effect. As shown in the figure, aluminum and chromium are good options to be used as partial substitutes of Si. This elemental substitution aims to obtain an alloy with outstanding magnetic performance, but with improved workability as opposed to Fe-6.5Si wt%. The idea of using Al and Cr as a substitute of Si comes from the fact that these two elements have significant effect on the electrical resistivity of Fe, which is a key parameter to control eddy current loses especially at high frequency applications, but their strengthening effect on Fe compared to Si is rather low [20]–[24].

The selection of the alloys was based on resistivity calculations as a function of their composition, with a targeted resistivity of at least 80 μΩ·cm, which corresponds to the high resistivity of Fe-6.5Si wt%[21], [44]. Another constraint was to keep Fe at% as high as possible, since this is what determines the flux density saturation. To estimate a tentative alloy composition, the model [6] shown in Equation 3-1 was used. Equation 3-1 is a model developed by AK Steel to estimate electrical resistivity of iron alloys (electrical steel) as a function of composition.

Equation 3-1

$$\rho = 13 + 6.25(\%Mn) + 10.52(\%Si) + 11.82(\%Al) + 6.5(\%Cr) + 14(\%P)$$

where ρ is the electrical resistivity with units of μΩ·cm, and the compositions are in wt%. Based on this model the following two compositions are proposed:

- Fe-4Si-4Cr wt% with an estimated $\rho = 81$ μΩ·cm based on Equation 3-1
- Fe-3Si-3Al wt% with an estimated $\rho = 80$ μΩ·cm based on Equation 3-1

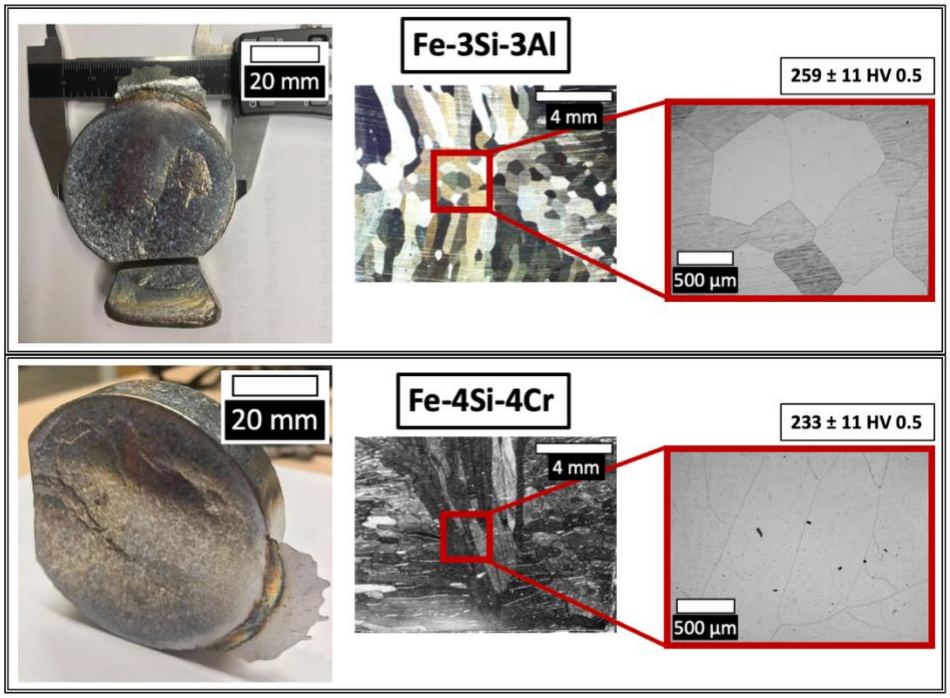

Figure 18 In-house made VIM ingots, experimental alloys as-cast micro and macro structure, and hardness. Top) Fe-3Si-3Al. Bottom) Fe-4Si-4Cr.

Ingots were cast in a 2 kg vacuum induction melting (VIM) furnace (Balzers, Germany). The elemental metals were melted in alumina crucibles (Zircoa). The furnace was evacuated and backfilled with Ar. The melts were heated to ~ 1550 °C and poured into a copper mold producing ingots of 50 mm in diameter and 20 mm thick.

Figure 18 shows the VIM ingots and the as-cast structure of the experimental alloys. Columnar grains can be seen in both samples but there is no presence of dendritic structure. The absence of dendritic structure is likely due to the narrow freezing range of these alloys and high solidification rate in the VIM. One thing to highlight is the absence of secondary phases or inter-granular phases, which is good since these are detrimental to the alloy workability. The presence of just one phase allows for hot rolling the sample right after casting with no homogenization needed. Hardness measurements on the as-cast alloys indicated values of 259 ± 11 HV0.5 and 233 ± 11 HV0.5 for the Fe-3Si-3Al and Fe-4Si-4Cr, respectively. Previous studies suggested that Cr has little effect on strengthening of Fe alloys [59], and this is corroborated by the fact that the Fe-3Si-3Al hardness is higher than the Fe-4Si-4Cr despite the fact the Cr alloy has more Si content. Also, this hypothesis is supported by the fact that the Fe-4Si-4Cr hardness is similar to the hardness reported for Fe-4Si wt% [74]. The lack of solution strengthening is a good indication that Cr does not affect the workability of Fe.

One of the goals of this project is to produce strips of one new experimental alloy by hybrid deformation processing (machining-based + rolling). Cutting force measurement experiments were performed on two experimental alloys using a linear slide apparatus with carbide cutting tools that consists of 2 mm thick plate workpiece and a rigid cutting tool with $\alpha = 0°$ that moves parallel to the workpiece. The workpiece was clamped between two glass blocks to guarantee plane-strain conditions, thus avoiding side flow during the cut. The undeformed chip thickness (t_0) was 125 μm. At the same time, forces on the tool parallel to V_0 were obtained with the use of a piezoelectric dynamometer (Kistler 9272, natural frequency ~2 kHz). Figure 19 shows the force traces representative of cutting Fe-4Si-4Cr and Fe-3Si-3Al obtained from the linear cutting experiment. The data on specific cutting force for the two alloys looks similar on the graph, which does not provide substantial information on the cutability differences of these two experimental alloys.

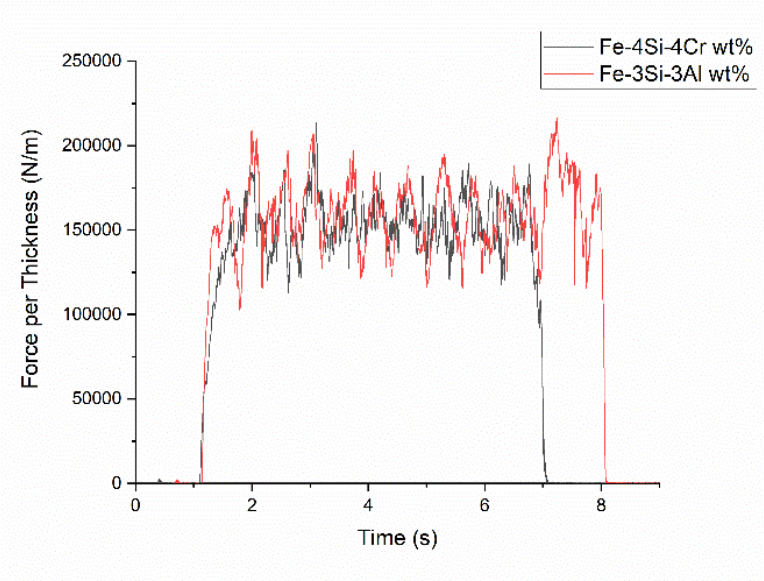

Figure 19 Specific cutting forces on FM for Fe-4Si-4Cr and Fe-3Si-3Al

3.3 Electrical resistivity results

The resistivities measured over three different lengths were **74 ± 3 μΩ·cm for Fe-3Si-3Al wt% and 85 ± 3 μΩ·cm for Fe-4Si-4Cr wt%**. The standard deviation remains below 5% of the average resistivity, which is a good indicator that the experiment is valid despite not following the 25-cm length required in the standard. The target was 80 μΩ·cm based on the resistivity of Fe-6.5Si wt%. Resistivity measurements for Fe-3Si-3Al wt% stayed below the target. There is a discrepancy in previous published data on the resistivity for Fe-3Si-3Al wt%. Based on measurements on a series of Fe-Si-Al alloys, Perrier and Brissonneau [24] claimed that the resistivity for this composition should be a value of 70 μΩ·cm, while Equation 3-1 predicts that the resistivity should be 80 μΩ·cm. The present resistivity measurements on this alloy are nearly the average of these previous predictions. It makes sense to believe that this experimental alloy would have a resistivity below 80 μΩ·cm since the Si+Al system adds up to 6%, which is lower than the 6.5% Si of the optimal electrical steel alloy. Initially it was thought that a possible Si-Al interaction could increase the resistivity up to 80 μΩ·cm, but it seems not to be the case in the results reported in these experiments. On the other hand, the Fe-4Si-4Cr alloy showed a resistivity a bit higher than the targeted value. Previous resistivity data for this experimental alloy is more limited than the case of the Fe-3Si-3Al wt%. Equation 3-1 predicts Fe-4Si-4Cr wt% should have

a resistivity of 81 μΩ·cm. However, the data collected reports a higher resistivity, showing a discrepancy as in the case of the Fe-3Si-3Al wt% alloy.

3.4 Experimental alloy workability

Since Fe-4Si-4Cr alloy has higher electrical resistivity, lower hardness, and similar cutting forces than the Fe-3Si-3Al alloy, it was decided that Fe-4Si-4Cr would be the experimental alloy used to complete the study. From here, this work will focus only on the Fe-4Si-4Cr experimental alloy.

Commercial production of non-oriented electrical steel sheets is composed of a series of complex steps. Figure 20 shows a concept map of the process. The workability of the material is an extremely important parameter for all rolling steps of this process [4], [75].

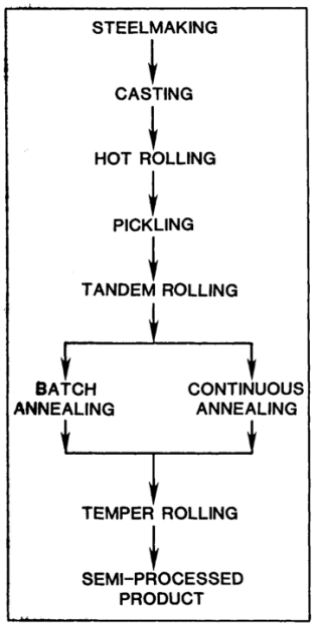

Figure 20 Production steps (from [39], with permission from Springer).

Studies on the workability of the experimental alloy were done by replicating the commercial rolling process, but on a smaller scale. For this experiment, the Fe-4Si-4Cr experimental alloy is compared to traditional Fe-Si alloys, Fe-1Si, Fe-3.2Si, and Fe-6.5Si wt%. Samples were hot rolled and sub-sequentially cold rolled, as elaborated in the experimental section. Figure 21 shows the results obtained from the workability experiment. The experimental alloy, the Fe-1Si and the Fe-3.2Si alloys could withstand 75% of cold work. It was possible to obtain 0.5

mm thick strips of these alloys with no visible cracks or defects on the edges. In contrast, it was to perform the full experiment on the Fe-6.5 Si alloy because the samples failed during hot rolling as shown in Figure 22.

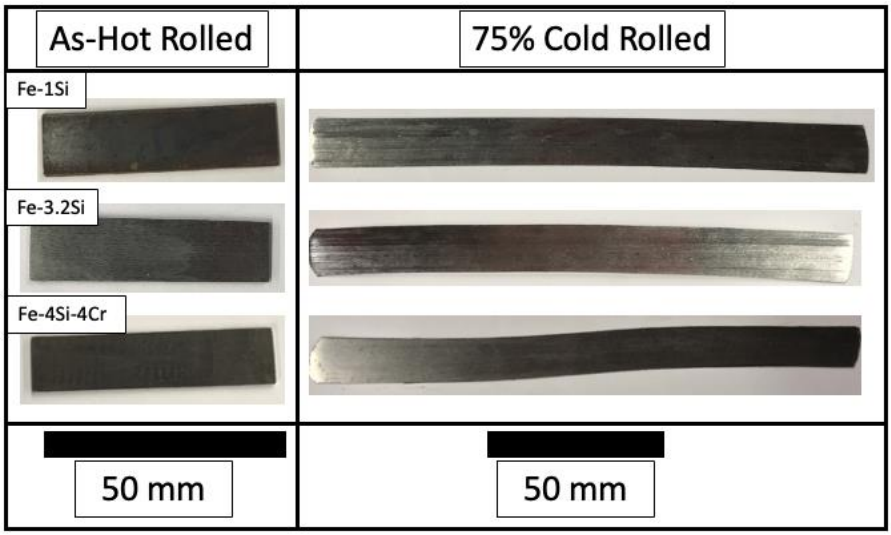

Figure 21 Workability test results after 75% cold work reduction. Graph reports results for Fe-1Si, Fe-3.2Si, and Fe-4Si-4Cr alloys.

These results show that despite the high silicon content, the experimental alloy is cold-rollable in contrast with the popular Fe-6.5Si wt% that possess a similar resistivity [21], [22].

Figure 22 Fe-6.5Si wt% sample failing after only 5% reduction during hot rolling.

4. HYBRID PROCESSING OF ELECTRICAL STEEL

Back in the introduction chapter, the author explained the workability issues of high-silicon electrical steel alloys. Throughout this work, the author has been elaborating on a background related to this workability issue and on some solutions to approach this engineering challenge. One approach that has been proposed is to develop a new experimental alloy with improved workability and outstanding magnetic performance (chapter 3 and 6.3). The second approach is to produce strips of the new experimental alloy using a hybrid deformation process. The combination of machining-based techniques like FM and HCE with light rolling introduces an alternative manufacturing process to produce electrical steel sheet. FM and HCE have been explained in section 2.7. This combination machining-rolling is what it is called as hybrid deformation processing.

FM and HCE (previously known as LSEM) are machining-based techniques that have been widely explored as alternative processing techniques for sheet metal production. Many materials have been explored, like pure aluminum and alloys, brass, magnesium alloys, pure titanium and alloys, and steels [14], [17], [63], [64], [76]–[79]. All these materials have processing issues, and FM and HCE have been proven to be an effective solution.

Fe-Si alloy strips have been produced via FM and HCE. The workability of the alloy is enhanced by the highly constrained shear deformation during cutting, the high-strain deformation, and the adiabatic heating. All these phenomena combined suppress the mechanism that leads to cracking during traditional rolling. There is an economic benefit from sheet making by machining-based techniques, and it is because of the reduction of the many intense energy steps from traditional rolling to a single stage of deformation characteristic of FM and HCE. Besides the economic benefits, there is interest in the greater microstructural control that is possible in FM and HCE that yields unique types of microstructures.

So why hybrid and not just machining-based? Because some alloys, like Fe-Si alloys, are susceptible to having a poorer surface quality after machining on the constraint face of the strips due to the high strength and poor machinability of the alloy. However, the surface quality of the strip can be significantly improved with some light cold-rolling right after cutting the strip. That is why hybrid deformation (machining + rolling).

4.1 Experimental methods

4.1.1 Materials, workpieces, and characterization.

Fe-4Si-4Cr (wt%) samples for narrow scale strip production were produced in house in order to control the purity of the alloy. High purity elemental metals used to manufacture the alloys had compositions in wt.% as follows: Fe 99.98%, Si (>99.999%), and Cr 99%. The experimental alloys were made using an arc melter with a non-consumable tungsten electrode on a water-cooled copper hearth. The alloys were melted under flowing 99.99% Ar, and they were turned over and re-melted three times to obtain button shaped samples with good homogeneity. The button samples were approximately 50 g, diameter of 4 cm, and thickness of 1.5 cm approximately.

On the FM and HCE experiments of narrow strips, the as-cast ingots of Fe-3Si-3Al and Fe-4Si-4Cr were cut and rolled into a disk. It was important to keep parallelism between the disk faces. Microstructure refinement was promoted via deformation and recrystallization.

Sample grinding for the metallography of the strips was performed using 320 – 2000 grits, and a final polishing was done using 0.05 μm alumina powder in water and 0.02 μm colloidal silica. The grain microstructure of the samples was revealed using 40% nitric acid aqueous solution. Vickers hardness was performed with a load of 500 g (HV0.5) for almost all the samples, but for thin samples 300 g (HV 0.3) was used instead. Also, the distance between indentations was 250 μm. 10 indentations were made on each test and values are reported as the mean ± one standard deviation.

Surface measurements and topography profiles were obtain using a 3D optical profilometer Zygo New View 8300.

4.1.2 FM and HCE Setup

Figure 23 FM/HCE set up. A) Rotating workpiece assembled to a mandrel B & C) Insert cutting tools assembled to the holders in two different positions.

The experimental set up for FM and HCE consists of a rotating workpiece, and a custom-made cutting tool assembled on a CNC Haas lathe. Figure 23A shows an example of a Fe-4Si-4Cr workpiece assembled to a mandrel. Figure 23B, and C, show the cutting tools used for narrow strip production. The narrow tool was an insert carbide of 8 mm width with a rake angle of +6°. These tools were used for rotary plunge cutting with a cutting speed range of 0.5 m/s – 6 m/s. Feed rate varied between 100 µm/rev and 250 µm/rev. The cutting tool materials include high-speed tool steel, different carbide grades (Co content), and coated carbide tools. To hold these cutting tools, a holder set-up was specially designed and manufactured for the machining system (see Figure 23B). FM strips were cold rolled to improve surface roughness. Cold rolling was performed through 10% reduction steps. The total reduction percentage varied depending on the working material ranging from 10-50%.

4.2 Strip production of experimental alloy

One recent effort to overcome the workability issues of high-silicon electrical steel sheet production has been the use of machining-based techniques. FM and HCE have been used to prove the feasibility of machining process to produce strips of low-workability alloys [13]–[15], and the details of the mechanics have been already explained in the section 2.7, as well as in literature [16]–[19]. Figure 14 and Figure 15 are sketches of these two machining-based processes. FM and HCE are single-step deformation processes that utilize a wedged cutting tool with a rake angle α that engages a rotating workpiece piece with a surface velocity V_0 at a pre-set depth of cut t_0. This

operation produces a continuous strip-shaped chip of metal with final/deformed chip thickness t_c. The difference between FM and HCE is that in FM there is no constraint on the upper face (free face) of the strip, allowing the material to freely flow with no control over the final chip thickness. This lack of control results in a rough free face whose surface roughness value varies depending on the material and the cutting conditions.

4.2.1 Free Machining (FM)

Fe-4Si-4Cr strips were successfully produced via FM in one single step, as shown in Figure 24. FM strips are characterized by having one rougher face which is known as the free face. Also, the face in contact with the cutting tool is called the rake face. The intrinsic roughness on the free face can be easily corrected by rolling. Figure 24A shows the typical microstructure of a FM strip. This microstructure is characterized by flow lines result of the intense and localized strain that occurs within the deformation shear plane, as has been explained earlier and in previous publications [14], [15], [19], [64], [80]. In this example, the effective strain for the strip formation was 1.5, for an $\alpha = 7°$ and a natural $\lambda = 2.3$. This intense deformation induces a considerable hardening effect on the strips, represented by the hardness values shown in Figure 24A compared to the as-cast value for the same alloy reported in chapter 3 as 233 HV. Additionally, Figure 24B depicts the results of cold rolling a previously annealed FM strip (FM+R), showing the improved quality of the free face surface roughness. The surface quality improvement is demonstrated by means of optical profilometry in Figure 24C and Figure 24D. Surface roughness changes from Sa (Arithmetical Mean Height) = 33.6 µm to Sa = 0.20 µm after rolling. Figure 25 is a photograph of a FM+R strip that shows the shiny appearance of the free face, which is a consequence of the improved surface roughness.

In contrast, Figure 25 also shows a wavy strip with some small cracks on the edges of the strip. These defects can be expected in narrow FM strips, especially for low workability alloys. Later in this work, the defects will be shown to be prevented.

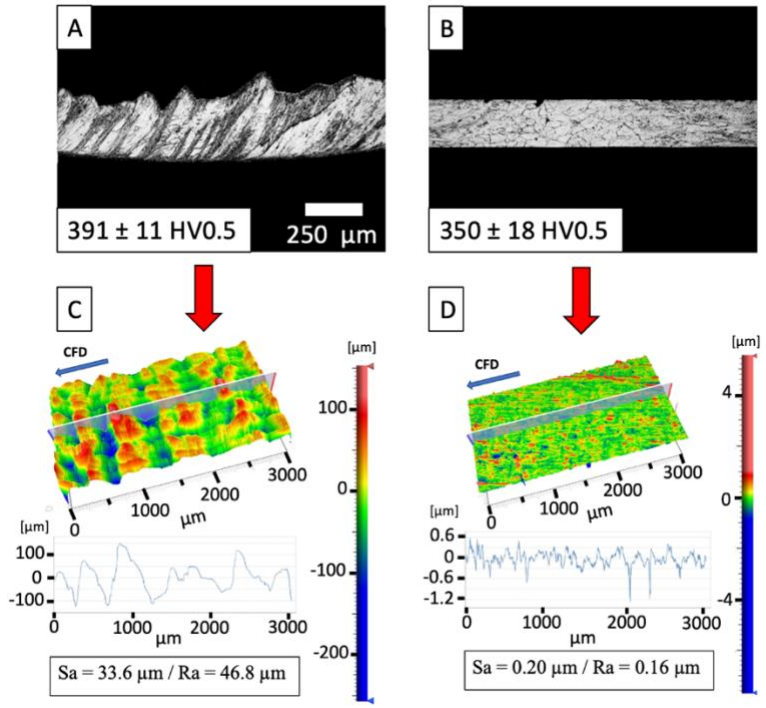

Figure 24 Side-view metallography, A) Fe-4Si-4Cr FM strip, B) Fe-4Si-4Cr FM+CR strip. Free face surface roughness, C) Fe-4Si-4Cr FM strip, and D) Fe-4Si-4Cr FM+CR strip.

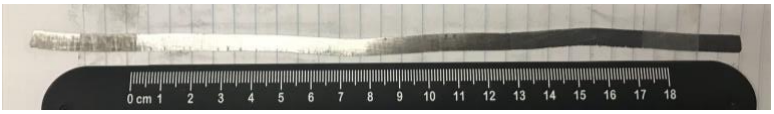

Figure 25 Photograph of FM+CR strip.

4.2.2 HCE

In contrast to FM, HCE has a constraint that can be set to control the final chip thickness, allowing advanced microstructural control and smoother surface roughness of the upper face (constraint face).

One can say that HCE is a more complete and complex technique for producing metal sheets. The as-cut surface roughness of HCE strips is better than the FM strips, and HCE also allows continuous production of strips due to better control over the microstructure. Figure 26 is an example of a 2 mm wide Fe-4Si-4Cr strip made by HCE, and the respective surface roughness profilometry. HCE resembles FM in several aspects, but with the difference that there is a constraint on the free face of the strip transforming this one onto a constraint face. The position of

the constraining tool is adaptable, allowing control over the final thickness of the strip, hence having control over the chip thickness ratio. The surface roughness for the HCE strip is Sa = 0.52 µm, which is superior to the FM strip and is slightly higher than the FM+CR strip. The effective strain for this HCE strip was 1.1. The effective strain for the HCE sample shown in this section is smaller than the one for the FM sample. This result makes sense considering that the lambda for a constraint sample is always smaller than the natural lambda of the FM strip (Figure 24A). The smaller effective strain is reflected in the lower hardness of the HCE strip compared to the FM strip. Other aspects of the process also affect the final hardness of the HCE strips like the high hydrostatic pressure and the higher adiabatic temperature rise.

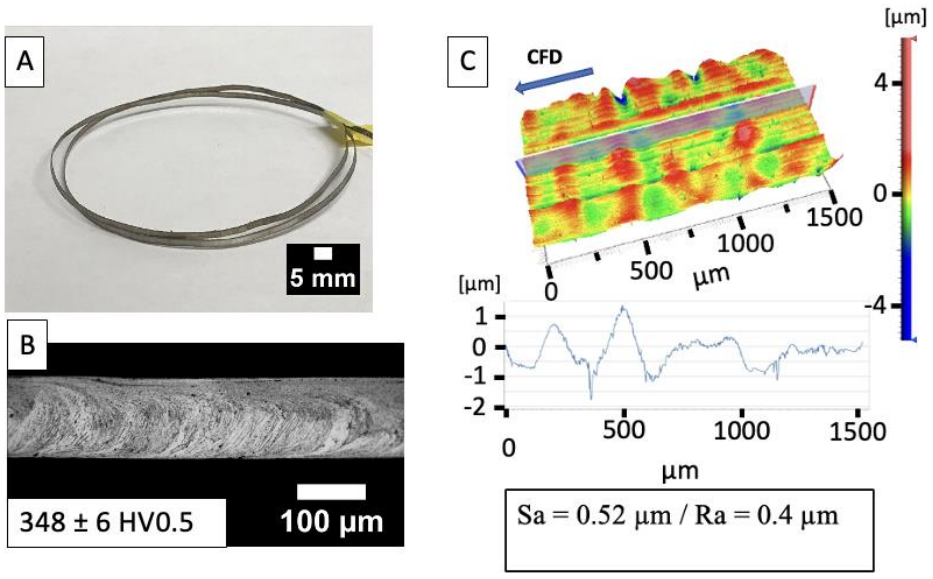

Figure 26 2 mm wide continuous Fe-4Si-4Cr HCE strip. A) Photograph, B) microstructure and hardness, and C) constraint-face surface roughness.

4.3 Microstructure control of machining-based strip production

4.3.1 Microstructure control as a function of λ

Following there is a list of cutting parameters that are important to produce strips via machining. These parameters play an important role on the final geometry and microstructure features of the strip. For more details, please read section 2.7

- Cutting tool rake angle, α

- Depth of cut or undeformed chip thickness, t_o
- Deformed chip thickness, t_c
- Chip thickness ratio, λ
- Workpiece surface velocity, V_o
- Initial temperature, T_o

There are also variables related to the workpiece that one can change to alter the quality of the strip produced via machining, like the workpiece grain size, texture, and dislocation density.

All these parameters have been explored during previous investigations on other materials. In the case Fe-Si alloys, the studies focused on exploring the effects of T_o and V_o on the strip's final microstructure [14]. In this section, the author will elaborate on the effects of λ on the strip's final microstructure. The author will also relate these results to previous studies on machining-based strip production and the magnetic performance of electrical steel alloys.

Deformation Zones

Figure 15 shows the schematic of strip production via machining, more specifically in that case through HCE. Previously it was mentioned that the red zone between points A & B in Figure 15 is the deformation or shear zone during machining. The deformation zone is a defined area in the workpiece/material where significant straining occurs. Figure 27 depicts a schematic of the deformation process during rolling. A metal plate of thickness h_0 enters the rolls at point A, and leaves the rolls at point B. The area A-B is the deformation zone for rolling [81]. Although Figure 15 and Figure 27 are just schematics, it is intentionally shown that the deformation zone during rolling is wider than the one shown in machining. The deformation zone confinement in machining is one of the reasons for the improved workability of this sheet production process.

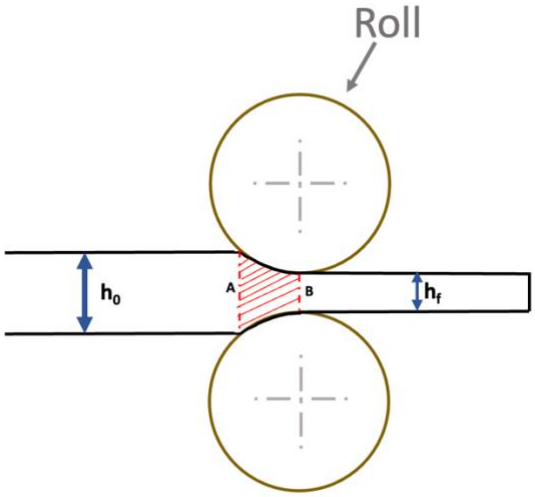

Figure 27 Schematic of deformation during rolling. The highlighted area corresponds to the deformation zone.

Figure 28 is a traditional rolled sheet microstructure where grains are elongated and aligned with the direction of rolling. This happens because of the deformation path that is developed during rolling, where point B of Figure 27 is the end of the deformation zone and the material exiting has a velocity V_B with a direction parallel to the direction of rolling. The microstructure obtained after rolling can change depending on the material crystal structure and workability, but in general, it will look like Figure 28.

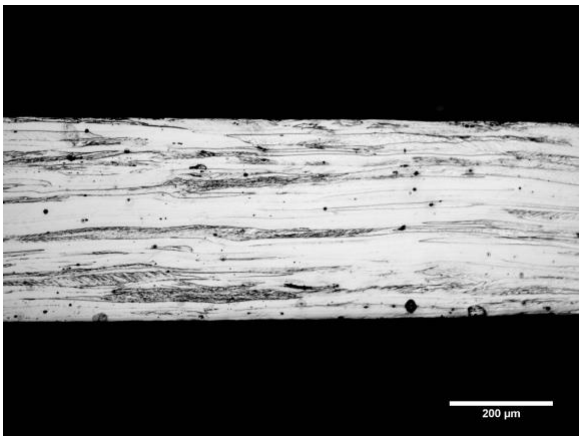

Figure 28 Microstructure of traditionally rolled sheet. The picture shows grains elongated and oriented towards the rolling direction.

The microstructure and deformation path are different on a machining-based strip. Figure 29 shows the typical microstructure obtained from an HCE strip. There is a primary deformation zone that is confined between the two red rectangles in Figure 29B. This primary deformation zone corresponds to the shearing plane A-B depicted in Figure 15. Since the flow lines are closely aligned with the deformation path [82], here they can be used as visual markers of the deformation path during machining, as shown in Figure 29. In addition to the primary deformation zone, in machining, there is also a secondary deformation zone. After the material passes through the primary deformation zone (the shear plane in Figure 15), the extreme conditions in the cutting tool-chip interface (high forces and temperatures) facilitate frictional force against the tool sliding. This creates a shearing effect right at the surface, and this is known as the secondary deformation zone for strips produced via machining [81]. The secondary deformation zone is shown in Figure 29B highlighted by the two red rectangles.

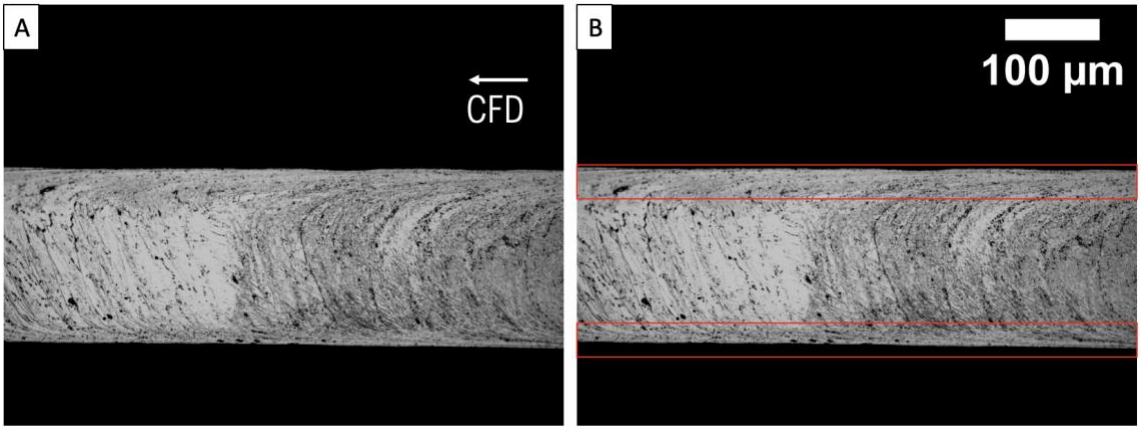

Figure 29 To the left is the microstructure of a Fe-4Si-4Cr HCE strip. To the right, the same microstructure with two red rectangles highlighting the secondary deformation zone.

Controlling deformation zones with λ

In the previous section, the author explained the differences between the primary and the secondary deformation zone. The microstructure of a regular FM strip (as shown in Figure 24A) is composed of one primary deformation zone that takes approximately 95% of the side view area, and one secondary deformation zone that takes the remaining ~5%. In the case of HCE, the microstructure of a strip is composed of one primary shear zone, and two secondary shear zones

(as shown in Figure 29). The first secondary deformation zone (lower rectangle in Figure 29B) corresponds, as well as in the FM strip, to the frictional force against the tool sliding. The second secondary deformation zone (upper rectangle in Figure 29B) corresponds to the extrusion effect due to the constraint tool in HCE.

Figure 30 shows the microstructure of three HCE strips made of Fe-4Si-4Cr. The cutting parameters of the strips are the same, except for λ which changes from 1.1 to 1.7. The chip thickness ratio has been defined as $\lambda = \frac{t_C}{t_0}$, where t_c is deformed chip thickness, which can be set at will for the HCE set up. Under the conditions described in Figure 30, the only method to vary λ is by modifying t_c. In other words, reducing λ requires one to reduce t_c. The lower the deformed chip thickness, the higher the level of constraining in the strip required from the constraint tool. This higher constraining is reflected in the fraction of the upper secondary deformation zone in Figure 30, where the $\lambda = 1.1$ sample has an upper secondary deformation zone fraction of ~40% while the $\lambda = 1.7$ has a fraction of ~10%.

Additionally, to the microstructural control, HCE has the unique capability to offer control over the strain imposed on the strip. Figure 16 shows, for $\lambda > 1$, that the higher the chip thickness ratio λ, the higher the effective strain ε on the strips. In other words, changing λ allows one to have control over the strain imposed on the strip. These variations in the effective strain can be corroborated by Figure 30, where the hardness value changes for the three different λ conditions, having the highest hardness value for the highest λ condition, which agrees with the model shown in Figure 16 and Equation 2-2.

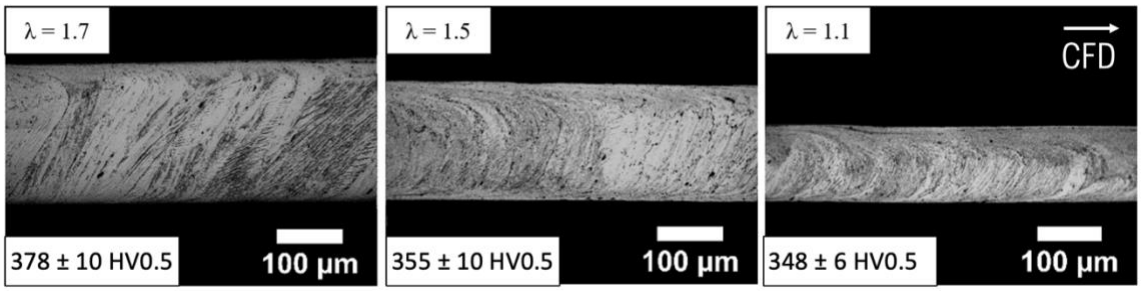

Figure 30 Microstructure of three different strips with different λ and their respective Vickers hardness.

There is a correlation between the deformation path and the result crystallographic texture. Since rolling does not offer control over the deformation path, there is little control over the crystallographic texture that can be obtained in traditionally rolled sheets. Crystallographic textures for the as-rolled condition include γ-fiber, α-fiber, and brass texture $\{011\}\langle 21\bar{1}\rangle$, which are deleterious to the magnetic properties of electrical steel. Other textures beneficial to magnetic properties are achievable via rolling, but these require precise combinations of heat treatments and deformation steps to achieve them. Some examples include Goss and cube textures.

On the other hand, the production of metal strips via machining offers access to a unique control over the deformation path of the strip. First, it is possible to control the angle of the shear zone with respect to the rake face (ϕ') as shown in Figure 17; hence one can set the angle of the flow lines of the primary deformation zone of the strips. As mentioned before, there is a correlation between the deformation path and the result crystallographic texture. This correlation has been shown before for machining-based strips of magnesium alloys and Fe-Si alloys [81], [83], [84]. Second, the primary and the secondary deformation zones have different textures. This is expected because of their different strain paths and it has been proved in a previous study for the Fe-Si alloys [83]. For strips like the one shown in Figure 30 with $\lambda = 1.1$ one could possibly manufacture strips with two different textures throughout the thickness of the sheet. Strips with complex textures as explained in this section are not likely to be advantageous for magnetic performance in electrical steels. However, the microstructural control shown here and in previous studies lay down a foundation for a potential crystallographic texture engineering for electrical steel, but also for other materials and applications.

Dynamic Recrystallization

Another unique feature of HCE related to microstructural control is the possibility to obtain fine equiaxed grain structures right after cutting. Figure 31A shows a traditional microstructure for a highly strained strip obtained via HCE, and Figure 31C shows a microstructure with coarse equiaxed grains resulting from annealing an HCE strip for 75 minutes at 1100 °C. The strip in the middle (Figure 31B) looks like the traditional HCE strained microstructure, but after closer inspection, it is possible to see that this strip has an equiaxed grain structure with an approximate grain size of 2-3 μm as shown in Figure 31D.

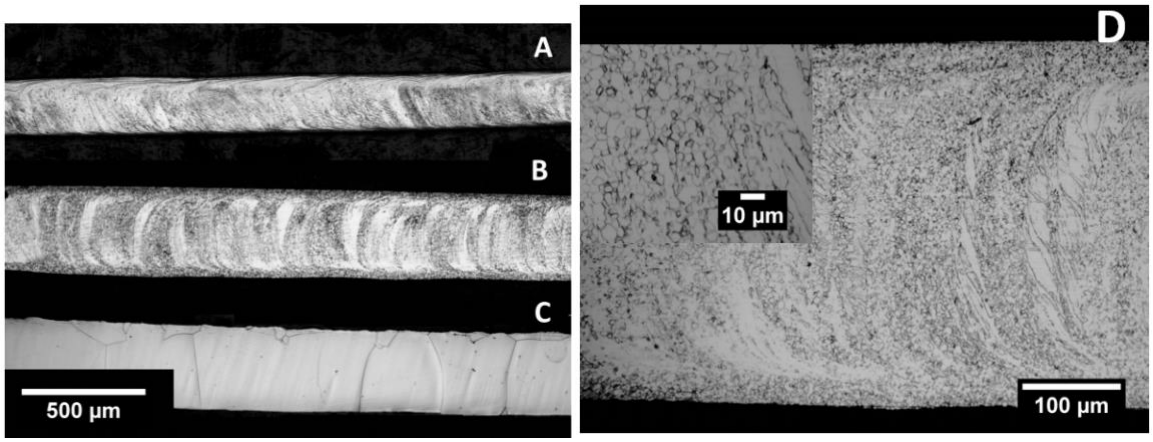

Figure 31 Three different HCE strips with different microstructures. A) Highly strained, B) dynamically recrystallized, C) statically recrystallized, and D) zoom-in of the dynamically recrystallized strip. CFD to the left of the micrographs.

High strain rate deformation processes like machining are characterized by having a narrow deformation zone and high adiabatic heating within it. The sample shown in Figure 31B was produced at a surface velocity of 8 m/s, as compared to Figure 31A which was produced at 3 m/s. The transition from a highly deformed microstructure to fine equiaxed grains is attributed to a considerably high adiabatic temperature rise in the deformation zone due to the high surface velocity of the sample, which could be also described as a classic case of dynamic recrystallization. Dynamic recrystallization is a metallurgical phenomenon that can be explained as a process of nucleation and growth of new grains during deformation, as opposed to static recrystallization which occurs after deformation with a separate annealing heat treatment. Dynamic recrystallization occurs when a metal is deformed at high strain levels and elevated temperatures, promoting re-arrangement of dislocation during the deformation of the metal [85]–[87].

Equation 2-3 models the temperature rise in the narrow deformation zone during plane strain machining. This model describes that the final temperature at the deformation zone depends on the initial temperature of the workpiece. Previous work showed that by increasing the initial temperature of the workpiece one can produce strips with as-cut equiaxed microstructure with grain size in the order of ~25 µm [14], [74], [83]. What makes unique the example shown in Figure 31 is that this dynamically recrystallized structure was produced with a workpiece at room temperature. The recrystallization is attributed to the adiabatic heating due to the high cutting velocity.

5. SCALING UP HYBRID PRODUCTION OF EXPERIMENTAL ALLOY STRIPS

The machining-based techniques were scaled up to produce strips up to 50 mm width. Process development work was done on model alloys including Al6061, brasses, and Fe-3.2Si wt%. In this work, 50 mm wide strips of the experimental alloy Fe-4Si-4Cr wt% were produced via hybrid deformation (machining and rolling). In this section, the author will present results on the characterization of the 50 mm wide strips and will comment on the quality of the strips. Scaling up the technology required to produce 50 mm wide strips of the experimental alloy has been an iterative process with several trials, experiments, design ideas, and failures. In this section, the author will also talk about the design and implementation of the process to scale up the technology for wider electrical steel strip production by FM and HCE. The results presented in this section were developed conjointly with the "Center for Materials Processing and Tribology".

5.1 Experimental methods

5.1.1 Materials, workpieces, and characterization.

On the FM and HCE experiments of wide strips, all the workpieces were machined into the required disk shape. The Fe-4Si-4Cr ingot for the wide strip experiments was obtained from "Sophisticated Alloys Inc" in the as-cast condition. An ingot of Ø4.3" and height of 11.5" (plus hot top) was prepared by VIM and the chemical analysis reported 4.02%Si, 3.88%Cr, and interstitials (C, O, and S) < 100 ppm. A slice of the ingot was hot forged ~70% in two steps, the first at 1,000 °C, and the last at 600 °C producing a disk nominally 210 mm diameter and 55 mm thick. A surface grinder was used to maintain the parallelism between the disk faces. Other workpiece specifications such as the final geometry and the microstructural condition of the workpieces used on this study varied for each material used and Table 3 summarizes all of them.

Table 3 Information of the working condition of materials used for FM and HCE.

MATERIAL	OBTAINED FROM	CONDITION	FINAL GEOMETRY	HARDNESS HV
Al 6061	McMaster-Carr	T6	51 mm thick – 203 mm diameter	100
Naval brass	AVIVA METALS	O25 (Hot rolled and annealed)	51 mm thick – 203 mm diameter	104
Brass 260	AVIVA METALS	M20 (Hot rolled)	51 mm thick – 203 mm diameter	106
Fe-3.2 Si	AK Steel	Hot rolled	25 mm thick – 203 mm diameter	194
Fe-4Si-4Cr	Sophisticated Alloys Inc	Refined microstructure	51 mm thick – 203 mm diameter	235

The microstructure of the samples was characterized, but only the microstructure of the electrical steel alloys is shown in this work. Sample grinding was performed using 320 – 2000 grits, and a final polishing was done using 0.05 micron alumina powder dissolved in water and 0.02 micron colloidal silica. The grain microstructure of the samples was revealed using 40% nitric acid aqueous solution for Fe-4Si-4Cr, 5% nital for Fe-3.2Si. Vickers hardness was performed with a load of 500 g (HV0.5) for almost all the samples, but for thin samples 300 g (HV 0.3) was used instead. Also, the distance between indentations was 250 μm. 10 indentations were made on each test and values are reported as the mean ± one standard deviation.

Surface measurements and topography profiles were obtain using a 3D optical profilometer Zygo New View 8300.

5.1.2 FM and HCE Setup

A more robust setup was used for wide strip production as it is shown on Figure 32. Figure 32A and B show the wide FM/HCE set-up with a rotating workpiece, insert tools, and cutting tool holder in rotatory configuration using a CNC Okuma lathe (50 HP). Figure 32C shows a set of custom WC-Co cutting and constraint tools provided by Seco Tools.

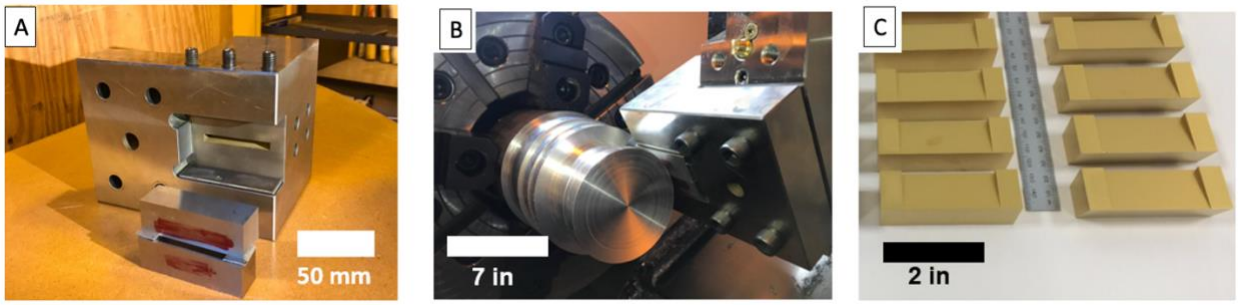

Figure 32 FM and HCE setup for production of wide strips (2 in width max). A) Cutting tool engaging the workpiece, B) cutting tool inserts made of WC-Co with TiN coating.

These tools were used for rotary plunge cutting with a cutting speed range of 0.5 m/s – 6 m/s. Feed rate varied between 100 µm/rev and 250 µm/rev. The experiments on wide strips (up to 48 mm wide) were done using two different cutting tool set-ups. A high-speed steel tool of rake angle 0° was used for cutting of Al 6061. Other workpiece materials were cut with the WC-Co tools with a rake angle of +10°. Cutting tool materials include different carbide grades (Co content), and coated carbide tools. To hold these cutting tools, a holder set-up was specially designed and manufactured for the machining system (see Figure 32A). The constraint tool had similar dimensions to the cutting tool. The constraint tools have a fixed clearance angle and rake angle of 3° and +10°.

FM strips were cold rolled to improve surface roughness. Cold rolling was performed through 10% reduction steps. The total reduction percentage varied depending on the working material, ranging from 10-50%. Wide HCE samples were lightly cold rolled (10% ≤) for the same purpose.

5.2 50 mm wide Fe-4Si-4Cr strip via hybrid processing

Figure 33 shows pictures of a 50 mm wide strip made of the experimental alloy Fe-4Si-4Cr. This is a FM+R strip that was eventually used for magnetic testing, as will be shown in the next chapter. In this study, the team was not able to produce 50 mm strips with HCE because high cutting force demand was compromising the cutting tools and constraining was not working well. More details on this process will be discussed in section 5.3

The cutting and post processing parameters for this specific strip were the following:

- Cutting = T_0 = 160 °C; f = 150 µm/rev; V_0 = 2 m/s; to = 203 µm; α = 20 °

- Annealing = 5 minutes at 700 °C
- Rolling = 25% cold rolled reduction.

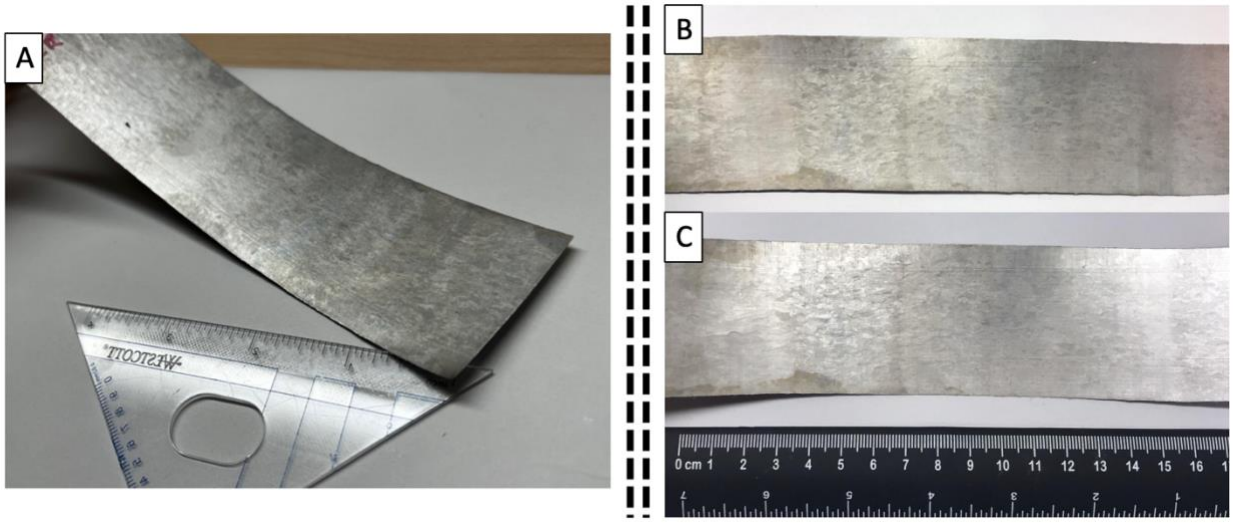

Figure 33 50 mm wide continuous Fe-4Si-4Cr FM+CR strip. A) Isometric view, B) top view of the rake face, and C) top view of the free face.

Figure 34 presents the microstructure of the 50 mm strip before and after rolling. The strips had a 5-minute intermediate annealing in between cutting and rolling to improve the surface quality of the strip. The reason is that the FM strip thickness is approximately 300 μm, which is close to the minimum reduction that can be reached with the rolling equipment available. The intermediate annealing reduces the strain hardening in the strips, thus pushing further the reduction limits of the rolling equipment. The intermediate annealing explains the lower hardness in the FM+R condition. As can be seen on the FM+R strips in Figure 34, a big portion of the free face is flat, which is expected after applying cold rolling on the FM strip. Nonetheless, there are some irregular spots on the upper face of the micrograph. These irregularities are spots where the cold rolling deformation did not affect the strip due to the reduction limitation of the equipment that the author already mentioned. These irregularities are result of the deformation mode of the FM strip, which is due to a segmentation formation on the free surface of the chip.

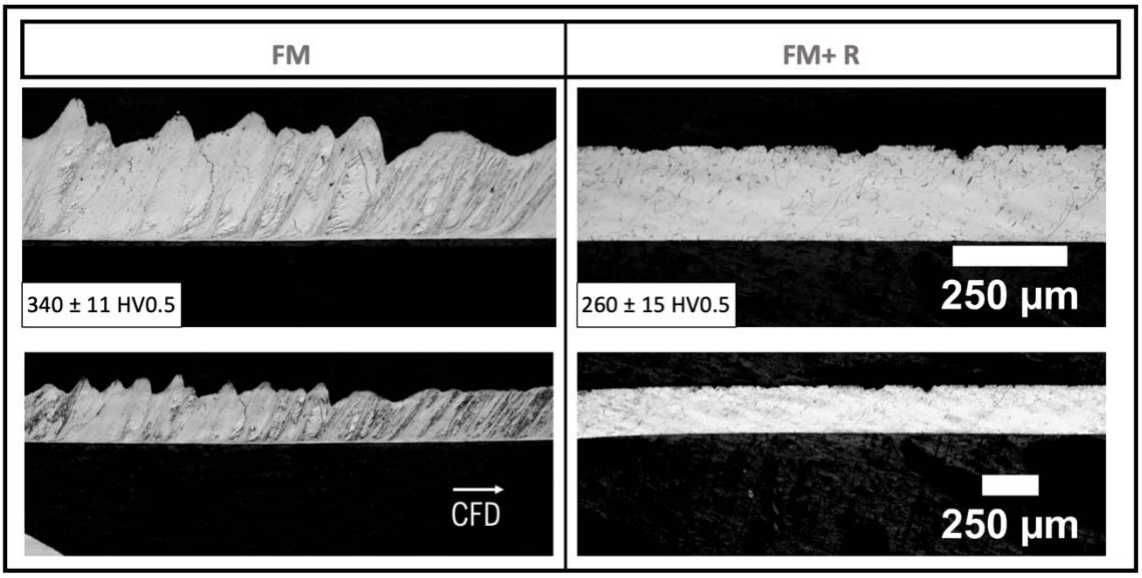

Figure 34 Side-view metallography of a 50 mm wide FM+R strip at two different scales.

Figure 35 depicts the optical surface profile of the 50 mm strip. The rake face of the sample is smoother with some rough regions that are attributed to the lift-up of material on the tool rake face. The S_a of the rake surface is 0.56 µm. The free surface of the FM+CR chip is characterized by elongated deeper regions perpendicular to the cutting direction, which correspond to the spots mentioned in Figure 34B that are due to incomplete rolling. The free surface is rougher than the rake face with S_a = 2.75 µm.

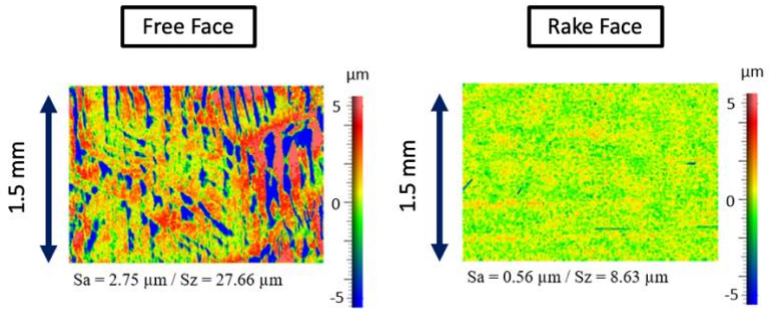

Figure 35 Fe-4Si-4Cr FM+R surface roughness optical surface profiles with rake face (left) and free face (right).

5.3 The process of scaling up machining-based production of Fe-4Si-4Cr sheet

Scaling up production of strips by FM and HCE from 2 mm wide to 50 mm sounds conceptually possible. FM and HCE are both plane-strain processes, which means that changing the width of the strip should not influence the strain mechanics of these process. In other words, increasing the strip width will not be deleterious to the improving workability effects of machining-based production of metal strips. So far there is not a proven process limitation for FM and HCE to machine different alloys or to make wider sheets. However, stronger alloys require higher power capabilities and machine stability, which can limit the production capability at the lab scale. Following there is a list of the technical challenges to be considered during the design of a production system of wider strips via machining:

- Higher cutting forces: Predicting the cutting forces of a process is essential to maintain the quality of the products. In addition to the strip quality, the cutting forces are also important to determining the need of acquiring a bigger, more robust, and higher capacity power cutting lathe. Additionally, if the new workpieces for wide strips have larger diameter, this would turn into higher torque demand ($\tau = d \times F$), thus higher power requirements ($P = \tau \times \omega$).
- New cutting tools: At the moment this project was started, the tungsten carbide cutting tools available were designed for production up 8 mm. Large custom WC tools had to be designed, and they had to be adapted to the new lathe system.
- Workpiece/mandrel bending: One challenge of FM and HCE is the component of the cutting forces that is parallel to the radial direction of the workpiece. This component can become an issue for mandril/workpiece bending. FM and HCE are machining with tight tolerances, and small deviations on the specific position of the cutting contact can compromise the whole process.
- Chattering and vibrations: Chattering occurs when there are harmonic vibrations between the workpiece, the cutting, and the machine. Chattering is common issue of machining where the workpiece and the cutting tools basically bounce against each other due the vibrations. This phenomenon causes strip waviness, loud operations, and it can severely deteriorate the cutting tool life. Higher cutting forces have the potential to increase cutting chattering.

- Workpiece preparation: Scaling up the process to produce wider strips by FM and HCE also means scaling the size of the workpiece. Depending on the set up, the workpiece requires preparation before cutting such as adapting to the cutting system and microstructural tune up. Preparing the newer larger scale workpieces will bring challenges, from how to cast such bigger ingots to how to the correct microstructural control, especially at the laboratory scale.

In this section the author explores the steps and iterations followed to achieve the production of 50 mm wide strips of Fe-4Si-4Cr. The following sections summarize the way the whole process was approached, showing intermediate results, as well as strategies that helped during the process, but also other strategies that did not yield good results.

Narrow strip production

The first step was to produce strips of the Fe-4Si-4Cr experimental alloy using set-up for production of narrow samples. The main goal is to collect data and learn about the capabilities of FM and HCE to make strips of the experimental alloy. Most relevant results of this part project have been shared in section 4.1. The takeaway from those results is that it is possible to produce continuous strips of Fe-4Si-4Cr via FM and HCE. Also, it was learned that the rollability of the machining-based strips is useful to improve the surface finish of FM strips.

Widest strip at narrow set-up

The second step was to explore the maximum capabilities of the set-up for narrow strip production (Figure 23A,B, & C). One can see that the cutting tools of the small set-up have maximum cutting gap of 8 mm, as shown in Figure 36. A 5 mm wide strips shown in Figure 36 is the maximum capability for the small production setup based on results. The stability of cutting tool arrangement limited the production of wider strips. The wider the strip, the less stable the set-up. As a consequence, the operation became louder, which it is a symptom of vibrations and chattering, and finally inserts chipped at the 7 mm strip experiments.

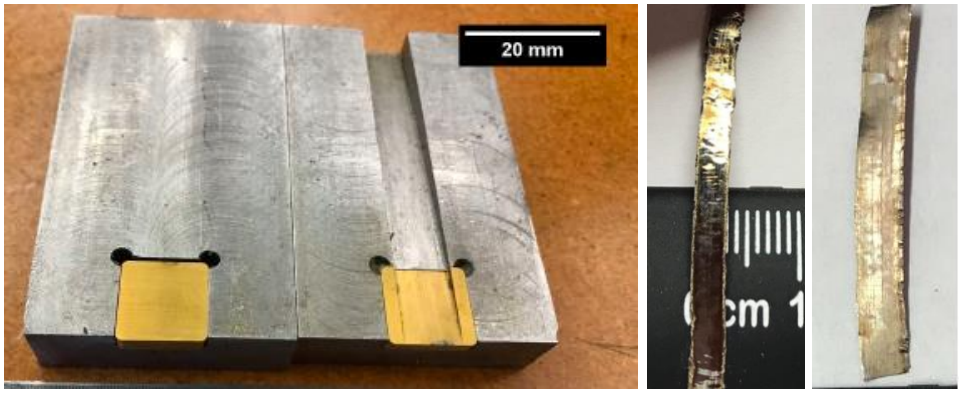

Figure 36 To the left the first-generation of tungsten carbide HCE tools, in the middle and to the right widest strips ever produced with this cutting tool (3.5 and 5 mm).

Wide set-up and wider softer alloys strips

In the experimental section, the author described the key aspects of the design for production via FM and HCE of wide strips of metals. Before using the wide set up to experiment with the Fe-4Si-4Cr alloy, cutting experiments were conducted with a series of other soft other alloys. Al6061, naval brass, Brass C260, and Fe-3.2Si were the materials used for these experiments. Table 3 summarizes the working condition data of all the workpieces.

The capabilities of FM and HCE to manufacture strips of a wide range of materials is broadly shown in Figure 37. This figure is an arrangement of pictures that shows strips produced by FM+R and HCE+R of 5 different alloys. Although it has not been mentioned the use of rolling on HCE samples, for wide samples very small reductions (~5%) were beneficial to the overall strips quality. Figure 37 shows strips of alloys that are known to have production issues including Al alloys, dual-phase alloys such naval brass, and low workability alloys like high-Si electrical steels. FM and HCE possess intrinsic advantages compared to other traditional sheet manufacturing processes such as rolling. One advantage is that FM and HCE are single step manufacturing processes. Due to this, typical rolling intermediate steps (heat treatments, multi-step deformation, etc.) are eliminated. Another asset of FM and HCE is related to the considerably lower equipment investment compared to a rolling mill and consequently the improved versatility of these sheet production machining processes.

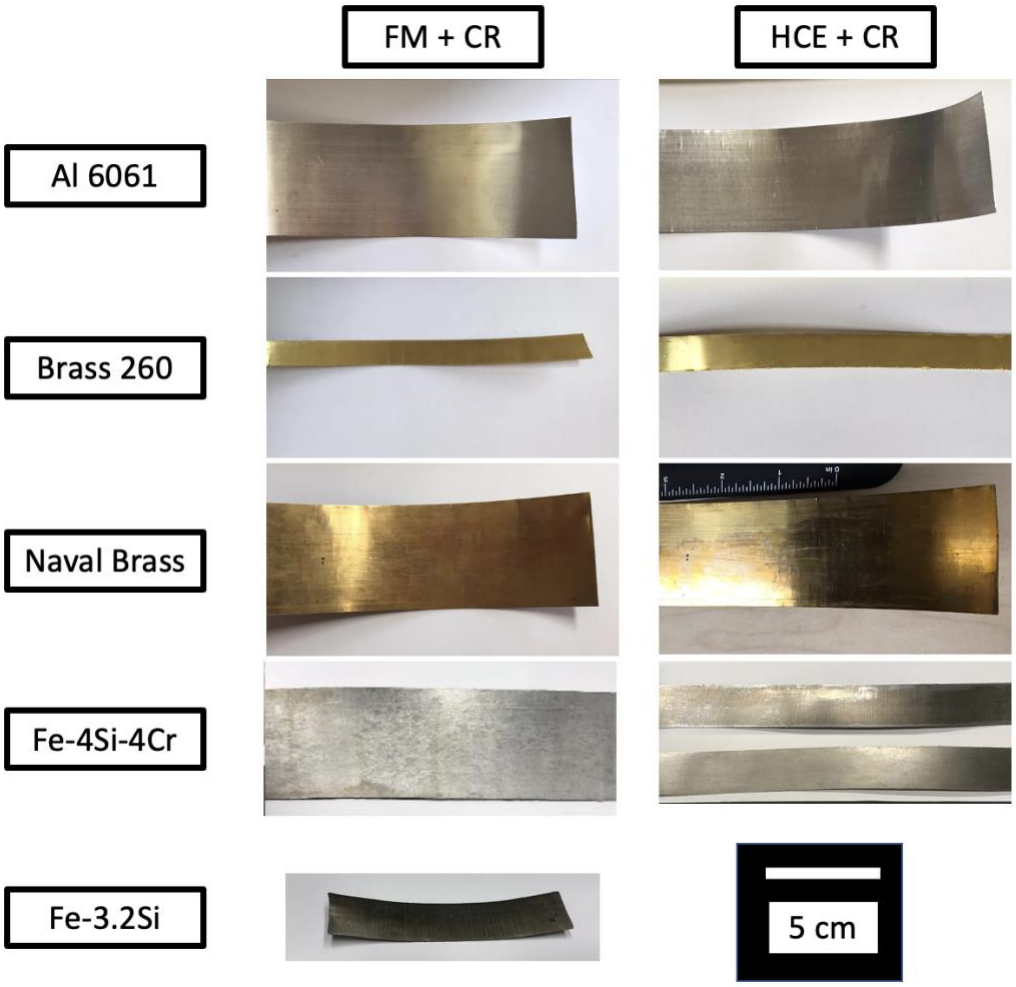

Figure 37 FM+R and HCE+R strip photographs of 5 alloys, Al6061, Brass 260, Naval Brass, Fe-3.2Si (just FM+R), and Fe-4Si-4Cr.

Wider Fe-4Si-4Cr Strips

The experiments performed with softer alloys (as shown in the previous section) provided the know-how to initiate the production of wider strips of Fe-4Si-4CR. Figure 38 shows the evolution of the hybrid production of Fe-4Si-4Cr strips. This figure summarizes the primary outcomes from this series of experiments. During this process, the researchers had to solve several issues related to the stability of the system, the tool integrity, and the quality of the strip.

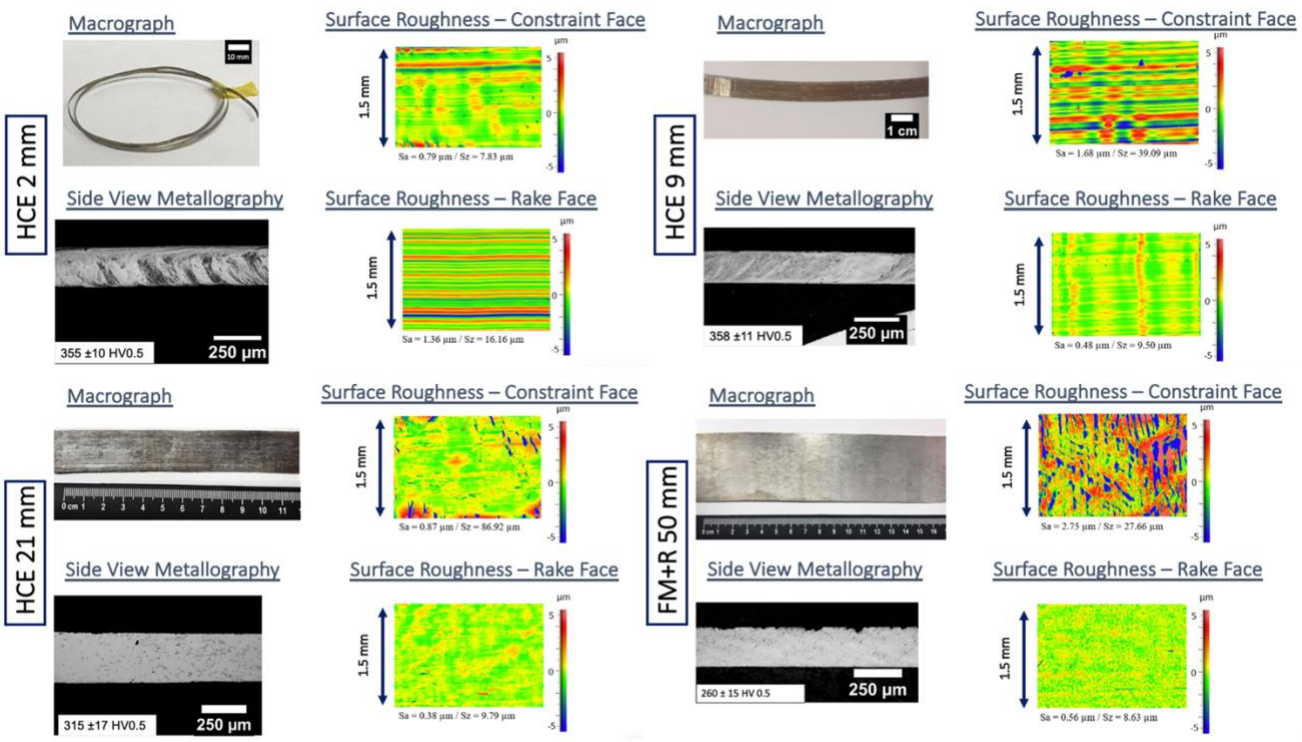

Figure 38 Evolution of the hybrid production of Fe-4Si-4Cr strips. Macrographs, microstructures, and surface roughness of 2, 9, and 21 mm HCE+R strips and 50 mm FM+R. Strip.

Notice that Figure 38 does not report an HCE strip for the 50 mm width. The HCE cutting tools were severely compromised on production 50 mm strips. It is believed that the reason for this issue is the high cutting+extrusion forces required. During the set-up design for the production of wider strips, the research team considered the high cutting forces as one of the design parameters. As a result, a lathe was acquired with considerably more power than the first one, a much stronger cutting tool system was designed, and the lathe's tailstock was engaged to reduce mandril bending and vibrations (see experimental section). Despite all the preventive actions, the system stability was compromised at HCE 50 mm, resulting in poor strips and cutting tools with excessive damage. Examples of poor strips are shown in Figure 39. In this document, it has been elaborated that light rolling passes can improve strips' surface roughness. For the strip shown in Figure 39, rolling is not an appropriate method to correct the defects of the sample.

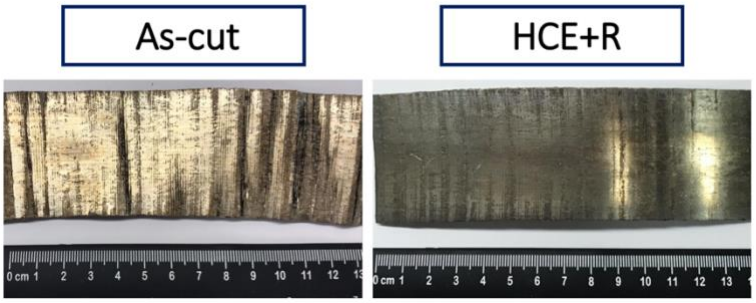

Figure 39 50 mm HCE strip in the as-cut and the HCE+R conditions. This figure shows the poor quality of the strip.

Experiments to reduce the cutting forces and thus increase the quality of the strip were performed. It is known that for BCC metals, the yield strength can be decreased by increasing the temperature. This reduction is due to the thermal activation of dislocation motion, which facilitates deformation. Linear cutting experiments were performed to determine the effect of initial temperature T_0 on the cutting forces and the strip surface roughness. It is expected that a reduction in yield strength due to the higher T_0 will yield lower cutting forces and an improved surface finish. The cutting parameters used for this experiment were:

- Width = 2.8 mm,
- Rake angle = 10°
- Depth of Cut = 100 µm
- Speed of Cut = 3 mm/s

The workpiece was heated using a MAPP torch, and temperature was measured using a thermocouple type K. Figure 40 shows the results of the cutting force and surface roughness measurements as a function of temperature. The experiments explored three temperatures, room temperature, 270 °C, and 470 °C. As shown in the figure, the higher the T_0, the higher the cutting forces. Additionally, the higher the temperature, the higher the surface roughness of the samples. These results do not support the hypothesis that a higher initial temperature can be used to improve the quality of the machined strips.

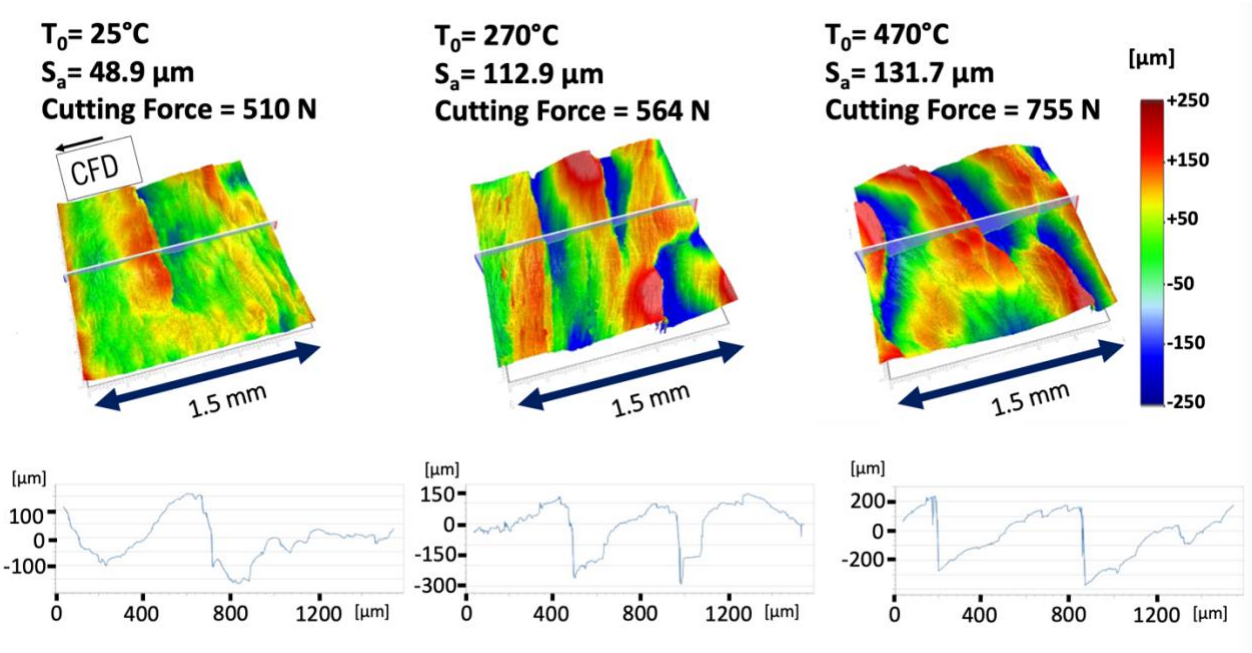

Figure 40 Cutting forces and surface roughness as a function of temperature, 25 °C, 270 °C, and 470 °C.

Previous work on the cutting of soft metals like aluminum and copper has shown that despite their low yield strength, the cutting forces can be high [88], [89]. This behavior happens in soft and ductile alloys due to the increased thickness of the strips that form with these materials. Higher thickening in machining is a consequence of how the material in the free face flow. For example, in pure aluminum, the free face forms very thick mushroom-like features. The higher the undeformed thickness, the higher the straining in the deformation zone, thus the higher the cutting forces. This analysis agrees that the surface roughness features are more significant for the higher temperature condition in Figure 40.

In addition to the linear cutting experiments, the author experimented with producing FM strips. The FM set-up offers the possibility of using higher cutting speeds, similar to those used in strip production via machining. The general cutting parameters used were $\alpha = +6$ and $f = 100$ µm/rev. All the other parameters were specific to each condition, summarized in Figure 41. The results presented in Figure 41 re-affirm the hypothesis that higher T_0 results in thicker strips.

There is a slight reduction in hardness on the strips with higher T_0. This could be due to low levels of dynamic recovery. Equation 2-3 explains that the final temperature in the shear zone after deformation is a function of T_0; this model supports the idea of having dynamic recovery.

Finally, there are no microstructural or macrostructural differences for the surface speeds explored in Figure 41.

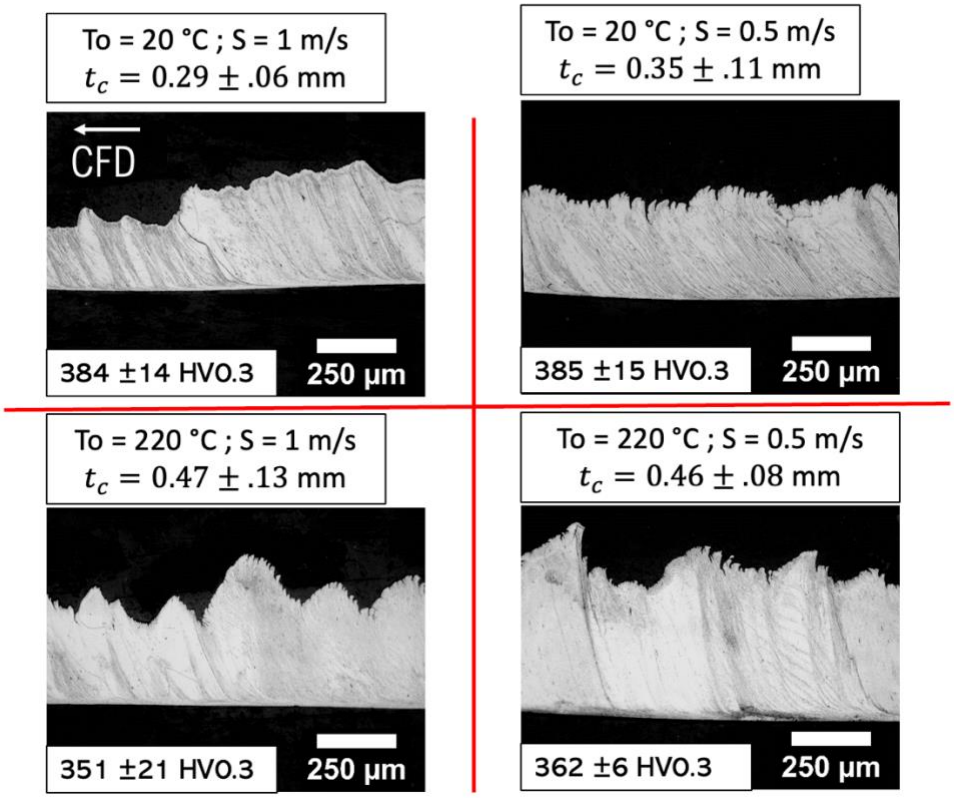

Figure 41 Results from experiments on FM strips as a function of temperature and surface velocity.

6. RECRYSTALLIZATION KINETICS AND TEXTURE ANALYSIS OF MACHINING-BASED AND ROLLED STRIPS

This chapter elaborates on the annealing behavior of the Fe-4Si-4Cr experimental alloy in the HCE and rolled conditions.

The parameters determining magnetic performance of electrical steel sheets are alloy composition and microstructure (**grain size**, dislocation density (strain state), **texture**). Understanding the microstructural evolution of the experimental alloy during annealing is key to the optimization of magnetic properties and potential transition to industrial applications.

The following sections will examine the formation of recrystallization microstructure in the experimental alloy on strips produced by rolling and HCE. The specific studies that will be covered are:

- Grain structure evolution
- Avrami kinetics (recrystallization fraction vs. time)
- Texture evolution

6.1 Experimental methods

6.1.1 Material and strip making

Recrystallization and texture studies were performed on Fe-4Si-4Cr in two different conditions, as-rolled and HCE (sample done by HCE). The material for the workpieces was obtained from Sophisticated Alloys Inc in the as-cast condition. An ingot of Ø4.3" and height of 11.5" (plus hot top) was prepared by VIM and the chemical analysis reported 4.02%Si, 3.88%Cr, and interstitials (C, O, and S) < 100 ppm. A polished and etched cross-section of the as-cast ingot is shown in Figure 42. Hardness is 98 HRB +/- 1 (~ 228 HV) which is close the value reported for the as-cast in-home made material reported in Figure 18 (233 +/- 11 HV 0.5).

For the rolling condition, samples of this material were cut by EDM into rectangular prisms of 30 mm width and 10 mm thickness. After this, samples were hot rolled to 2 mm at 800 °C and then cold rolled to 400 μm. Intermediate annealing was conducted at 800 °C for 5 minutes in an air furnace between cold rolling steps after every 25% cold-work. For samples in the HCE

condition, a slice of the ingot was hot forged ~70% in two steps, the first at 1,000 °C, and the last at 600 °C. The cutting parameters for the HCE samples were: V_o = 3 m/s, Feed = 220 µm/rev, λ = 1.7, T_o = 160 °C, and a rake angle of 10˚. Metallography data on the as-deformed structure of the conditions are available in Figure 43.

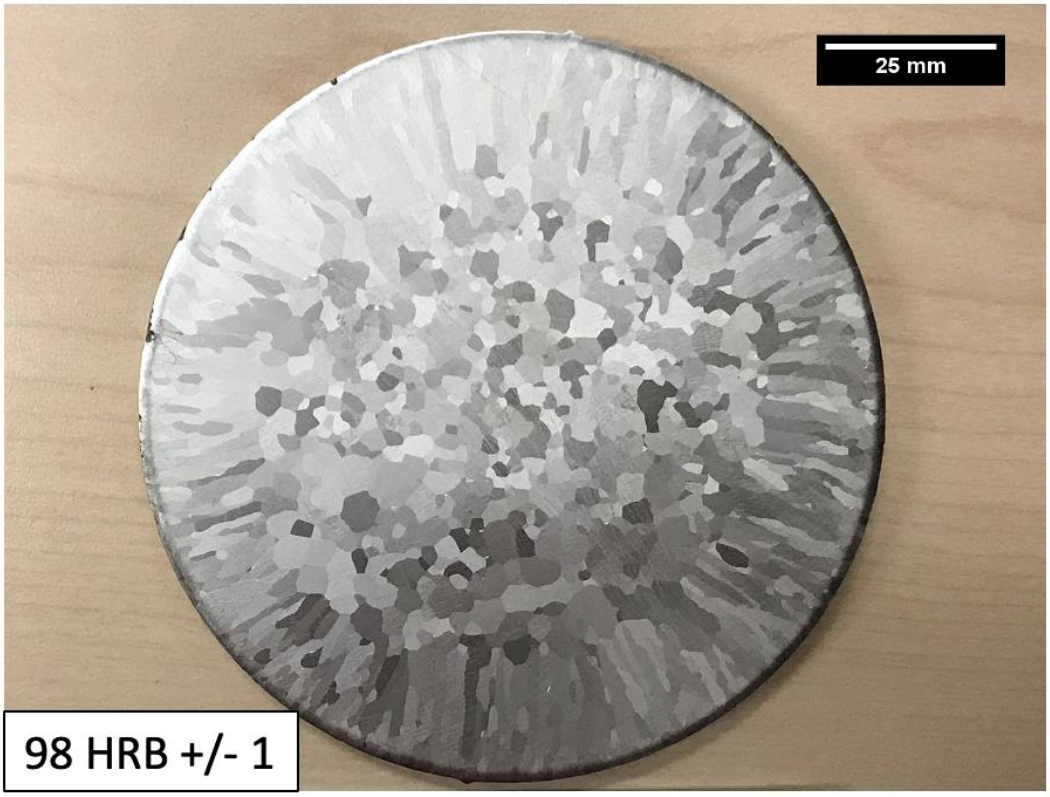

Figure 42 Fe-4Si-4Cr ingot cross section in the as-cast microstructure and hardness.

6.1.2 Sample preparation

For the recrystallization study, 1x1 cm samples were cut using a shear. Samples were annealed in a small air furnace for times ranging from 5 s to 50,000 s depending on the temperature. Samples were annealed at 600, 700, 800, and 900 °C. The loading and unloading procedure of the samples in the furnace was strictly repeated to reduce time error. Temperature was measured using a type K thermocouple in contact with the specimens. After annealing, all samples were ground 1 mm on the edge surface of evaluation to remove the layer affected by remaining strain for the shear. This grinding operation was done putting special attention on maintaining the parallelism between the surface and the RD/CFD. Samples are evaluated in the cross-sectional area composed of the RD and the ND for the rolled sample, and the chip flow direction CFD and the ND for the

HCE samples. Silicon carbide paper with grits from 320 to 2000 were used to grind the samples, and a final polishing using 0.05 μm alumina powder dissolved in water and 0.02 μm colloidal silica. The samples were etched for microstructure examination using 5% nital for the Fe-Si alloys and 40% nitric acid aqueous solution for the Fe-4Si-4Cr alloy. The recrystallization kinetics were tracked by relative hardness measurements between the cold-worked and fully recrystallized conditions. Vickers hardness testing was performed with a load of 500 g (HV0.5) and 250 μm distance between indentations. At least 10 indentations were made for each hardness and the values are reported as the mean ± one standard deviation. The average grain size was calculated using the linear intercept method. The grain size distribution was done using the thresholding technique in ImageJ and the grain size of each grain was calculated finding the equivalent circular area diameter. A normal curve was fit to the grain size distribution of each sample for comparison.

6.1.3 Texture analysis

Texture analysis was performed in the as-deformed condition, intermediate annealing (IA), and in the fully annealed (FA) state for the rolled and HCE conditions. For IA and FA, samples were annealed at 800 °C for 60 and 3600 s, respectively. The texture analysis of the samples was done using electron backscatter diffraction (EBSD). All EBSD data was taken in the cross section composed by the RD and the ND (or CFD and ND for HCE samples) using a Quanta 650 FESEM equipped with an EDAX EBSD detector. All the data collected was cleaned up using a filter to remove data points with C.I. <0.1. Samples were hot mounted using copper filled diallyl phthalate resin, and then they were polished following the procedure previously described. A final polishing step was done using a Pace GIGA900 vibratory polisher for 4 hours in 0.02 μm colloidal silica. Macro texture is represented using the orientation distribution function (ODF) and pole figures (PF) that were built using data obtained from several EBSD scans. ODFs were built using the tool MTEX-5.7.0 utilizing the calcODF function which calculates the ODF from EBSD data with a statistical method called kernel density estimation. The PF were built using OIM analysis utilizing the harmonic series expansion method. Many EBSD scans were used for the calculation of each ODF and PF. The statistical significance of this technique to represent macro texture data compared to conventional XRD technique has been explored by some investigators. As explained by some authors, cubic materials require 500-1000 single grain orientations to have a good

statistical representation [90]. In this study, many EBSD scans were taken to obtain >500 single grain orientations for the FA samples, and >>1,000 for the IA and as-deformed condition.

6.2 Grain structure evolution

6.2.1 Background

In metallurgy, annealing is a type of heat treatment designed to alter the microstructure and sometimes the composition of metal. Usually, annealing is used to transform highly deformed microstructures (like in rolled or machined strips) into fully recrystallized microstructures. Annealing has three main stages, recovery, recrystallization, and grain growth. Recovery is a stage characterized by rearrangement of dislocations into lower energy configurations, but without any change in the grain structure. During recovery, there is a decrease in the dislocation density of the sample, which causes a small reduction in hardness. The second stage is recrystallization, and this is when there is enough thermal energy available to create new strain-free grains that nucleate and grow to consume the highly deformed microstructure. During recrystallization there is a large drop in hardness. Finally, there is grain growth, which results from extended high temperatures passed the time of recrystallization. If the thermal energy is sustained, the grain size will continue to coarsen, reducing the total grain boundary interface. Following there is more information on the nucleation and grain growth phenomena which are two essential concepts for the development of this chapter.

Nucleation

Let us define nucleation as the random formation of a new phase inside a matrix of the former phase [91]. In recrystallization, nucleation refers to the presence of small grains with high angle grain boundaries that grow and form a low-defect structure. Although the name suggests the creation of nuclei, they do not form during recrystallization. Nuclei are placed in the material during deformation. Just a few of all the nuclei activate and grow during recrystallization. Approximately 1 out of 1 million possible sub-grains emerge to be a growing nucleus [92]. The

nucleation theory explains how, among all the options, one nucleus transforms into a nucleus that will form areas with high angle boundaries and migrate and move through the high strained regions. There are three principal models to explain nucleation: migration of pre-existing high-angle grain boundaries, nucleation by low-angle boundary migration, and nucleation by sub-grains coalescence. Following, Table 4 describes the fundamental notions of the leading nucleation models.

Table 4 Key notions of the three principal models of nucleation.

Migration of pre-existing high-angle grain boundaries:	**Nucleation by low-angle boundary migration**	**Nucleation by sub-grains coalescence**
High-angle boundaries migrate easier than low angle boundaries. Pre-existing high angle boundaries will migrate towards grains with high levels of strain. The process occurs due to the reduction of stored energy that happens when defects are eliminated thanks to the migration of the boundary. There is reduction of the total grain boundary area by the migration of boundaries [23].	Understanding of the migration of low-angle boundaries is still very limited. This model uses the theory of polygonization to explain how high-stressed lattice regions suddenly transform into low-stressed lattice regions. These newly transformed low stressed lattices regions are capable to grow at the expense of the surrounding highly stressed lattice [93]. During recrystallization, the main migration occurs on high-angle boundaries, however low-angle boundaries also move, but very slowly, making it difficult to study [94].	Two adjacent grains will rotate with respect to each other until the lattices coincide and form just one grain. Reduction in orientation differences, and disappearance of sub-boundaries, thus reducing stored energy in the structure. Many grains do the same until a zone with high-angle boundaries that would growth by boundary migration.

Grain Size Growth

Grain growth is the last step of annealing. Grain growth occurs at high temperatures once the material has undergone recovery and recrystallization. It is also the last step for a

polycrystalline material to lessen its internal free energy and the step that takes the most time in the entire process. The driving force behind grain growth is reducing the grain boundary surface area, hence reducing the total interface energy, especially for high-angle grain boundaries [92]. There are two types of grain growth, normal and abnormal. During grain growth, a collection of grains growing at a much more rapid rate than their neighbors characterizes abnormal growth. This turns into a microstructure dominated by a few groups of big grains. Abnormal growth or secondary recrystallization is the mechanism used to develop grain-oriented electrical steel. Normal growth, on the contrary, is characterized by a more homogeneous microstructure with similar grain boundary mobility rates throughout the sample.

There is not an ultimate theory to explain the migration of boundaries. However, some studies have been published to demonstrate how the variation of composition, deformation and annealing parameters can vary the boundary migration velocity [95], [96].

6.2.2 Results

The microstructure of a mechanically deformed sample depends on the mechanics of the specific deformation process. Figure 43 shows the as-rolled and as-machined microstructure for rolled and HCE strips. Highly elongated grains, known as flow lines, aligned with the rolling direction, and a heterogeneous microstructure characterize the rolled sample. The heterogeneity of the microstructure in Figure 43A is typical of rolled Fe-Si samples, and it is shown by the dark and white zones in the picture [97]–[104]. The differences in etching are related to the dislocation density. The dark zones correlate to grains with high dislocation density, whereas white zones do with low dislocation density. This microstructure heterogeneity is commonly seen in Fe-Si rolled strips. It could be potentially changed with modifications in the initial as-cast microstructure or with an annealing heat treatment after hot rolling.

Investigations have reported information that relates this heterogeneity of the microstructure with the orientation of the different grains [9], [98], [105], [106]. These early studies stated that grains with low dislocation density are generally < 110 >//RD oriented, while darker grains, i.e., high dislocation density, usually have a < 111 >//RD orientations.

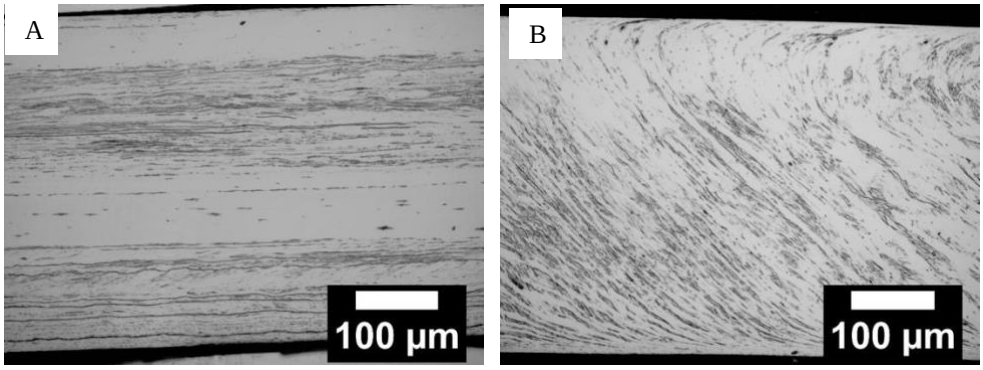

Figure 43 As-deformed optical microstructure, A) corresponds to the cold-rolled strip and B) displays the corresponding metallography of the HCE strip. Notice HCE strip has two distinctive deformation zones (primary and secondary).

Figure 43B presents the metallography of an HCE strip in the as-cut condition. In contrast to the rolled sample, the HCE microstructure is more homogeneous. Figure 43B shows the common elements of a machining-based strip, such as highly deformed grains, angled deformation flow lines, and two distinct deformation zones. HCE strips are likewise characterized as having a homogeneous microstructure because of the existence of a confined shear plane during deformation. Microstructure homogeneity in the as-deformed condition is significant because it affects the grain size distribution of the annealed material. The more homogeneous the as-deformed structure, the narrower the grain size distribution, hence better magnetic properties.

Figure 44 depicts the evolution of the grain structure transformation of the rolled and HCE specimens as a function of annealing time at 800 °C. It is commonly understood that nucleation of new grains during recrystallization takes place preferentially in the shear bands, because of the rather high energy stored compared to the regions of lower deformation [9], [98]–[100], [107]–[110]. Likewise, it is the case with the two conditions examined in this investigation. A closer examination of Figure 44 shows that nucleation is already happening at 30s, as the micrographs of the two conditions present small nuclei near the high deformation zones. The hardness differences between 0 and 30 s also supports the completion of recovery. As a comparison, nucleation in the so-called “white zones” of low dislocation density takes more time, and it is not noticeable until the 400s frame in the rolled sample. An analogous case is noted in the HCE sample, but the area fraction of low dislocation density is smaller than the rolled sample. Having a better distributed deformation in the microstructure of the HCE samples results in a more homogeneous microstructure in the early stages of recrystallization. Surprisingly, at subsequent stages of

annealing the hardness and microstructure homogeneity is similar for the 2 conditions showing that regardless of the manufacturing technique the final grain structure and materials hardness are similar. This is not the case for the texture of the samples, but this will be the topic of a later section. Figure 45 shows the grain size distribution comparison of the rolled and the HCE samples. For the rolled sample, the average grain size is 56 µm and the standard deviation is 31 µm. For the HCE sample, the average grain size is 67 µm and the standard deviation is 37 µm. The standard deviation is approximately 55% of the average grain size in the. two conditions, which confirms that after grain growth the rolled and HCE samples have similar microstructure homogeneity, although the median grain size is approximately 10 µm smaller for the rolled condition.

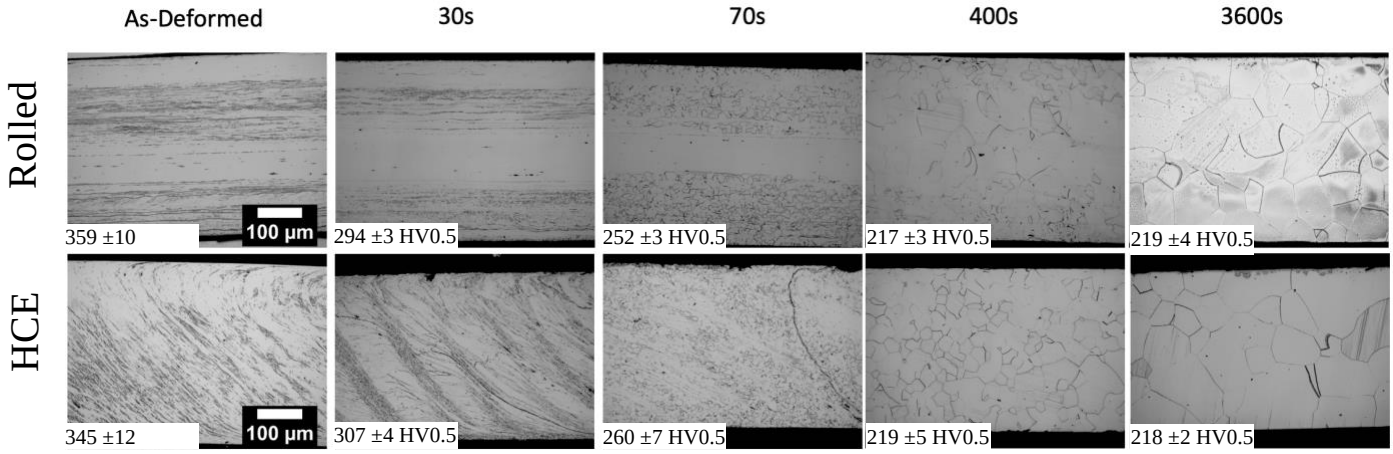

Figure 44 Microstructure evolution throughout annealing time at 800 °C for the rolled and HCE conditions.

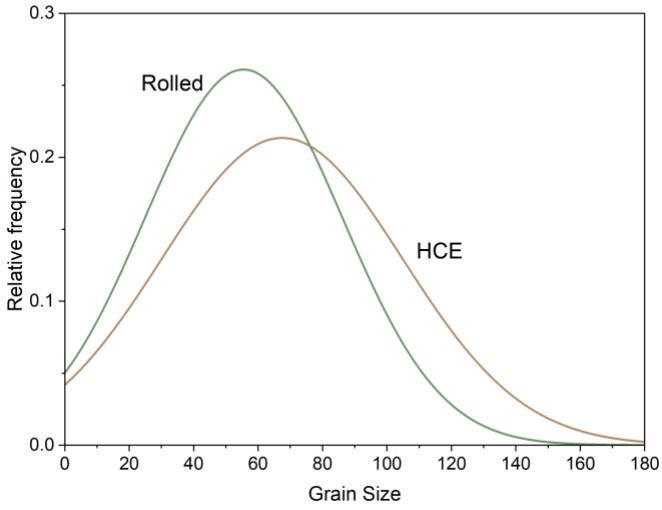

Figure 45 Grain size distribution of rolled and HCE conditions at 800 °C for 3,600 s.

The grain size evolution in electrical steels is important at the final annealing stages because of the proven effect of grain size on magnetic properties. Several researches have examined the ideal grain size for electrical steels [109], [111]–[113]. This optimal grain size depends on composition and sheet thickness. A general settlement in literature is that, among commercial electrical steel sheets, the ideal grain size of approximately 150 µm. In this study, the investigators did not seek to discover an ideal grain size for the specific experimental conditions. However, later in the document, magnetic properties will be reported, and to have the best possible results, it is needed to determine an ideal grain size for the specific samples studied here. After completing a literature review and characterizing commercial materials of **similar thicknesses** to the samples produced via hybrid processing, it was concluded that 80 µm is the grain size targeted. The grain size-thickness relationship has an effect on the magnetic properties of electrical steel. The average grain size found in literature and in commercial materials is about ¼ of the strip thickness. Grain boundaries are known for being deleterious to the motion of the magnetic domain walls; thus, the bigger the grain size, the better the magnetic properties. However, having grains of a size equal to the strip thickness is detrimental to the magnetic properties as well. There is a reason why the ideal grain size should be a fraction of the total strip thickness, and it is related to the anisotropy of α-iron. If one has a material with grains as big as the strip thickness, there is a

possibility that some of those grains will have the hard direction of magnetization aligned to the RD. Having a smaller grain size reduces the likelihood of this happening.

Figure 46 shows the evolution of the average grain size as a function of time and temperature for rolled and HCE samples of the experimental Fe-4Si-4Cr alloy. The samples evaluated are in the same condition as those shown in the as-deformed column in Figure 44. Figure 46 shows an expected tendency where the higher the temperature, the larger the coarsening effect in the grain structure. Differences between the rolled and HCE sample are appreciable at 900 °C, where at times >1,000 s, the grain size of the HCE is about 40% larger than the rolled sample. The data shown in Figure 46 is a sub-product of the data collected for the recrystallization kinetics of the experimental alloy. This grain size evolution data sets the path for a systematic study of grain size effects on the magnetic performance of the experimental alloy samples.

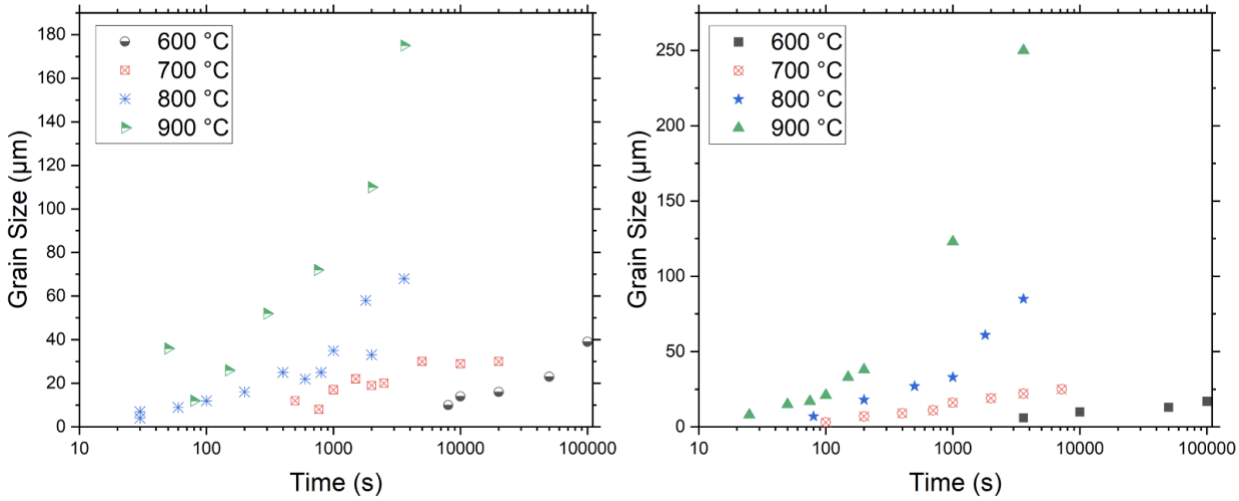

Figure 46 Evolution of the average grain size as a function of time and temperature. The rolled sample is to the left, and to the right is the HCE sample.

6.3 Avrami kinetics (recrystallization fraction versus Time)

6.3.1 Recrystallization kinetics - background

The recrystallization kinetics of metal can be helpful in understanding the effects of annealing in the transformation from mechanically deformed to a fully annealed microstructure. The Johnson–Mehl–Avrami–Kolmogorov (JMAK or Avrami) model can describe the isothermal

solid-to-solid transformation of a metal. Based on this model, the extent of transformation during recrystallization is characterized by an "S" shape, as shown in Figure 47. Another characteristic feature of these graphs is that the beginning (recovery and early nucleation) and the end (grain impingement and growth) are slow. In contrast, the middle part (nuclei growth) is characterized by happening fast [107], [114], [115].

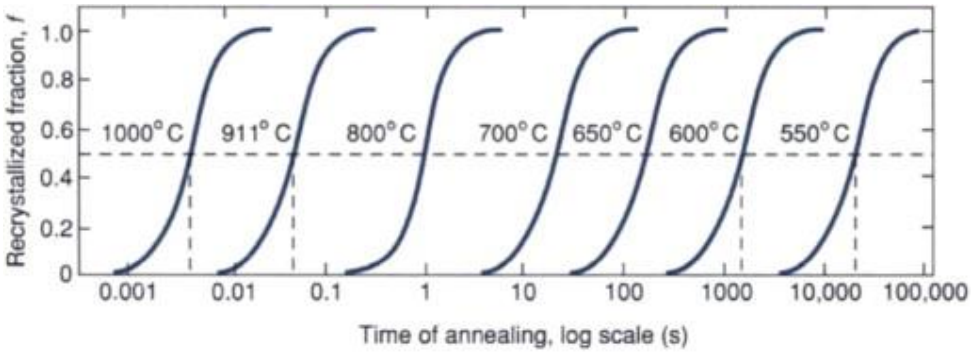

Figure 47 Recrystallization fractions vs. annealing time curves for Fe-3.25Si wt% 60% cold-rolled (from [115], with permission from Elsevier).

One reason for the popularity of the JMAK model is its simplicity (which, in fact, some investigators think is a bad thing). Equation 6-1 is a simplified version of Avrami's model, where X_{rex} is fraction recrystallized usually measured experimentally, k(T) is the recrystallization rate constant and is a function of the temperature, and n is the Avrami exponent [116]–[118].

Equation 6-1

$$X_{rex} = 1 - \exp[-k(T)\, t^n]$$

Equation 6-1 can be mathematically manipulated to obtain an expression to calculate n. Using the Ln on both sides of the equation, one can find a new expression as follows:

Equation 6-2

$$Ln(k[T]) + n\, Ln(t) = Ln\left(Ln\left(\frac{1}{1-X_{rec}}\right)\right)$$

Equation 6-2 can be plotted in the form shown in Figure 48, which is an example for Fe-Mn-C alloys. This graph is known as the Avrami plot, and from this plot, it is possible to do linear interpolation to find an equation with a slope corresponding to the Avrami exponent, "n."

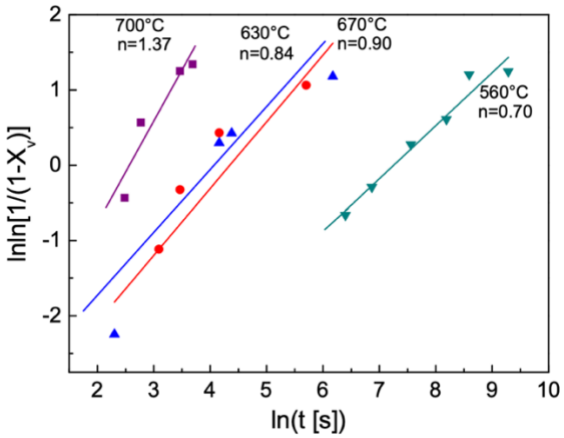

Figure 48 Avrami plots for Fe-Mn-C alloys at various annealing temperatures (from [107], with permission from Elsevier).

The Avrami model assumes random nuclei formation and isotropic and constant grain growth. Without these conditions, a strict representation of the recrystallization kinetics cannot be guaranteed using Avrami's model. However, using this model is still helpful in correlating the recrystallization behavior between different samples.

6.3.2 Results on recrystallization kinetics

Figure 49 shows the recrystallization fraction curves for the experimental alloy as a function of time for the two conditions studied in this investigation. The starting cold-worked hardness of the two rolled and HCE samples are 359 ± 10 HV0.5 and 345 ± 12 HV0.5, respectively. The calculated strain is 0.3 and 1.2 for initial conditions of the rolled and HCE samples, respectively.

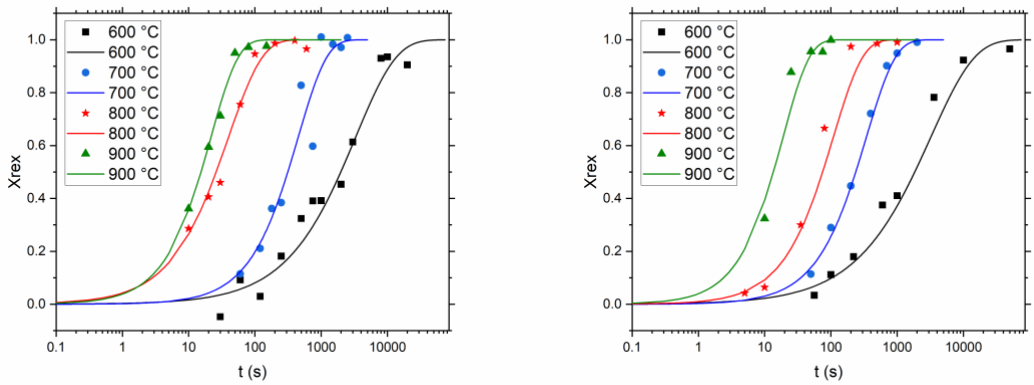

Figure 49 Recrystallization fraction of rolled (to the left) and HCE (to the right) samples as a function of time.

The extent of recrystallization was tracked by relative hardness measurements as a function of time. The hardness data evolution as a function of time is available in Appendix A. The recrystallization fractions are calculated using Equation 6-3, where H_i equals the hardness in the as-deformed state, H_f is the final hardness or the hardness when recrystallization is completed, and H(t) is the hardness at each specific time.

Equation 6-3

$$X_{rex} = \frac{H_i - H(t)}{H_i - H_f}$$

The curves in Figure 49 have the characteristic "S" shape described in the background section. This shape is distinguished for having a slow transformation rate at the beginning and the end, but a fast transformation in between. This behavior allows one to define the start and end of recrystallization as 5 and 95%, respectively, as shown in Figure 49 and Table 5.

The start and end times presented in Table 5 do not show a pronounced tendency. For example, at 600 °C, the recrystallization time range is more extensive for the HCE sample, but 900 °C is more significant for the rolled sample.

Table 5 Start and end of recrystallization range for different sample conditions and literature data.

Sample	**Recrystallization Time for Different Annealing Temperatures**			
	T = 600 °C	**T = 700 °C**	**T = 800 °C**	**T = 900 °C**
Rolled	20 – 30,000 s	6 – 2,000 s	0.3 – 300 s	0.1 – 200 s
HCE	10 – 40,000 s	10 – 2,000 s	1 – 600 s	0.1 – 100 s
Literature [52], [115]	300 – 10,000 s	3-100 s	0.2 – 4 s	0.01 – 0.3 s

A wide range of information is available on the recrystallization kinetics of commercial electrical steel alloys. However, the variability of the experiment parameters is vast, making it hard to compare the data collected in this thesis to the literature directly. Table 5 also contains data on recrystallization times for Fe-3.25Si wt% from a source that, to the author's knowledge, is the data with the closest parameters for comparison. This previous work was done in a similar temperature range to this study and for a 60% cold work reduction. For all the different temperatures, the time range of recrystallization is shorter for the Fe-3.25Si experiment. This difference is attributed most likely due to the lower solute content of the Fe-3.25Si alloy, but there are also differences in the amount of initial strain.

Having similar recrystallization time ranges for the rolled and HCE samples is not something the author would expect from these experiments. Microstructural distinctions between the rolled and machined samples should drive the recrystallization kinetics to be different. The microstructure of samples formed by machining methods has a higher ratio of high-angle to low-angle grain boundaries compared to rolling [15], [82], [110], [119]. Microstructures with higher fractions of high-angle boundaries nucleate and grow sooner because of the enhanced probability of having critical nuclei. Hence, the HCE samples should recrystallize earlier than the rolled samples. Additionally, the more homogeneous microstructure characteristic of HCE samples should be another factor making the recrystallization kinetics of rolled and HCE samples different. The author infers that the reason why the HCE sample does not have a faster recrystallization is due to the HCE workpiece's initial temperature (T_0 = 160 °C) during cutting. This high initial temperature could lead to dynamic recovery/recrystallization in the as-deformed condition, and it has been proved that recovery can reduce the Avrami exponent, hence slow the recrystallization process [52].

Prior studies and earlier in this document, it was demonstrated that dynamic recrystallization is feasible in machining-based deformation processes when the experiment satisfies certain conditions [14], [18], [87]. Adiabatic heating concentrated in the narrow deformation zone is one characteristic of machining-based deformation processes. As pointed out in section 2.7, the higher the initial temperature, the higher the final temperature of the strip [14]. Hence, it is possible to get enough adiabatic heating to promote dynamic recovery or recrystallization, depending on the final temperature.

The samples studied as-deformed hardness are 359 ± 10 HV1 and 345 ± 12 HV1 for the rolled and HCE conditions, respectively. The results shown in Figure 30 showed that for a similar lambda and rake angle, the hardness of an HCE Fe-4Si-4Cr strip could be around 371 HV. This reinforces the idea that the HCE samples of this study have undergone some dynamic recovery.

Figure 50 shows the JMAK plots of the data displayed in Figure 49. Displaying the data in this manner allows one to extract the Avrami exponent "n" from the slope of the linear regression of each temperature data points, as illustrated in Figure 50.

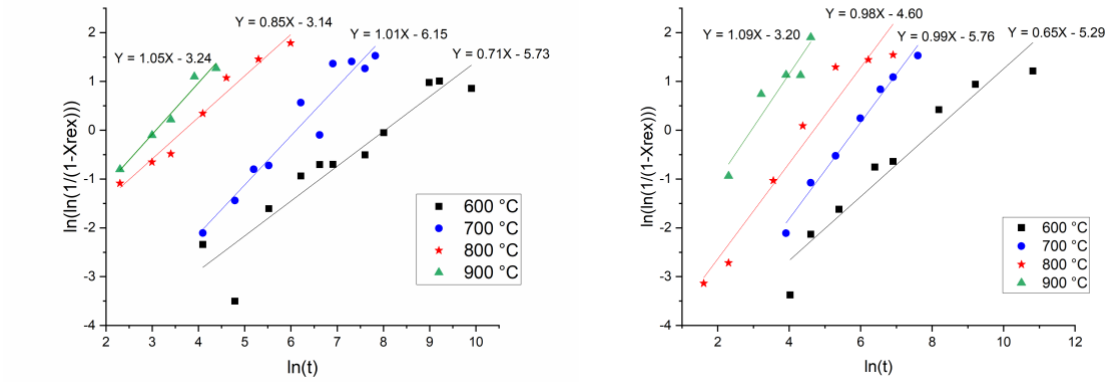

Figure 50 JMAK plots of the experimental alloy for the rolled (to the left) and HCE (to the right) samples. Linear interpolation equation included.

When nucleation and growth are constant in time, Avrami exponents are usually between 3 to 4. The dimensionality of the grain growth determines one number or the other. However, experimental studies have shown that in situations where nucleation ends before the start of grain growth, the Avrami exponent is more likely to be between 1 and 2 [120]. In this investigation, all Avrami exponents were close to or lower than 1. Based on the literature found on recrystallization

kinetics for electrical steel alloys, a possible explanation for the low Avrami exponents can be based on the heterogeneity of the grain structure, as the recrystallization microstructures have illustrated in Figure 44. Previous studies have shown that for heterogeneous microstructures, the corresponding Avrami exponent can range from 1 to 2. This conclusion is supported by the fact that a heterogeneous microstructure does not comply with the assumptions made by the Avrami model of random nuclei formation and isotropic and constant grain growth [118], [121]–[123]. The dynamic recovery present in the HCE samples could also be a reason to the low Avrami exponent. After collecting and analyzing all the Avrami kinetics data, it seems evident that this model is not adequate to quantitively characterize the recrystallization kinetics of real samples of the new Fe-4Si-4Cr experimental alloy. The heterogeneity of the rolled and HCE samples makes it complex to characterize. However, the data collected can be used for practical applications.

Using the metallography and the Avrami model data, it is possible to plot a visual representation of the different stages of recrystallization for a range of temperatures (600–900 °C) and time (10–10,000 s). Figure 51 presents two diagrams produced and called annealing maps. These maps are a visual representation of the stages of the annealing process for a range of temperature versus time conditions, i.e., the annealing maps summarize in a picture the different stages of the recrystallization process for the Fe-4Si-4Cr samples. The author produced these annealing maps motivated by the work of Cuevas et al. [124]. They develop a discrete temperature versus time data matrix that compiles the various recrystallization steps of their TWIP steel samples. For the Fe-4Si-4Cr experiments, the author extended further on the approach of Cueva et al. and developed a procedure to get a continuous annealing map instead.

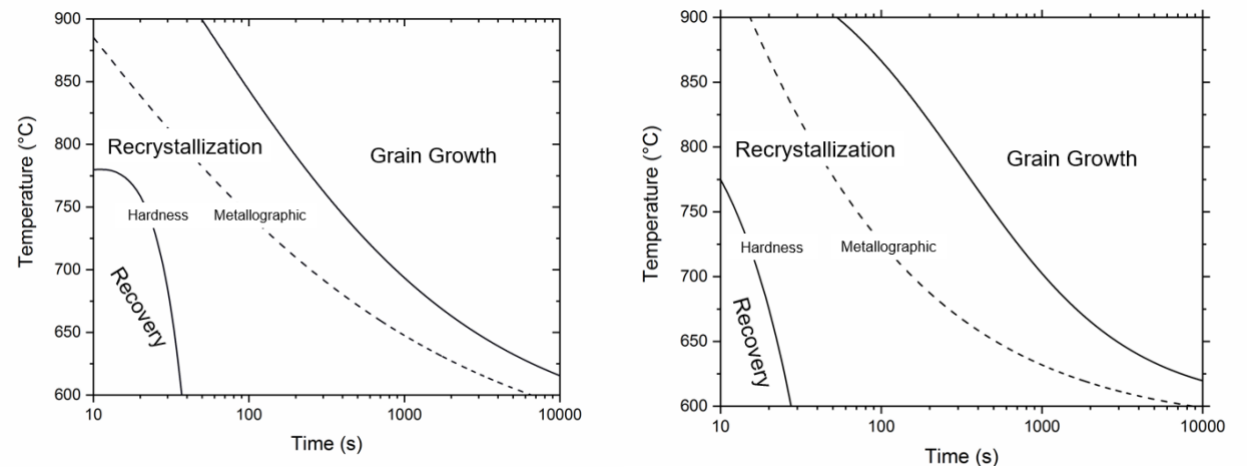

Figure 51 Annealing maps for the Fe-4Si-4Cr alloy. The rolling sample is to the left, and to the right is the HCE sample.

The maps show the three main stages of the annealing process for a mechanically deformed matrix, recovery, recrystallization, and grain growth. Using the data of recrystallization fraction modeled by Equation 6-3, the start and end points of the recrystallization stage were as defined 5% and 95%, respectively. Also, an alternative beginning to recrystallization based on the metallographic observations was defined. The author defined this alternative start point of recrystallization using the times where the metallography data revealed the first traces of nucleation. Note that these times lag behind those sensed by recrystallization fraction and are specific to the etching treatment used to reveal the recrystallized grains. Everything passed 95% of recrystallization fraction was defined as the zone of grain growth. After defining the boundaries, the data was gathered into a discrete matrix similar to the one shown in the paper of Cuevas et al. [124]. Using the matrix, a contour map was plotted to visually define the boundaries between the different stages of recrystallization. Different interpolation techniques were used to smooth the boundaries. There are similarities between the maps for the rolled and HCE conditions. One can identify some differences in the details like the recovery zone is bigger for the rolled samples, but this are small differences. The similarity of the annealing maps correlates well with the closeness of the recrystallization fractions and Avrami plots.

6.4 Texture evolution

6.4.1 Background

The easy direction of magnetization in α-iron (Fe – BCC) makes the concept of anisotropy relevant in soft magnetic materials. The magnetic properties of electrical steels can be significantly influenced by the total orientation of all the individual grains that comprise the whole material. Therefore, GO and NGO electrical steels exist, as explained in section 2.4.

The texture of an electrical steel sheet depends on the multiple previous deformation and annealing steps. The texture imposed by deformation is not random. Dislocations move within a system of slip planes and directions during plastic deformation. The fact that each crystal structure has a set of preferred slip systems makes the texture of a deformed material very specific. Similarly, during recrystallization, the ability of a material to nucleate grains with specific orientations is influenced by the microstructure features. Finally, out of the many nucleated grains, which ones will grow to form the final microstructure can be influenced by the conditions of the heat treatments. GO steels (known for having a strong Goss texture) are an example of abnormal grain growth, where (110)[001] grains grow and consume a large portion of the matrix. This abnormal growth can only be achieved if a specific combination of deformation and annealing steps is followed. For more information, the author recommends [52], [125], [126]

In this section, the author evaluates the texture evolution of rolled and HCE samples made of the Fe-4Si-4Cr experimental alloy. The rolled samples are expected to have similar results as have been widely shown before for other electrical steel alloys [9], [99], [101], [102], [106], [110]. For more information on the main types of texture for rolled samples and how to represent and read texture data, please read section 2.4.

6.4.2 Results and Analysis

Rolled Strips

Figure 52A shows the ODF at $\varphi 2 = 45°$ of the Fe-4Si-4Cr rolled sample in the as-deformed condition. In addition to the ODF, Figure 52A also depicts the position of the γ-fiber, the partial α-fiber, and the θ -fiber in the Euler space, which are the main texture components of the results here presented. The three fibers were superimposed on the graph for visualization aid. Also, Figure 52B is an ODF at $\varphi 2 = 45°$ that shows the position in the Euler space of several orientations. Figure 52B and Figure 7B are used to compare the experimental data and analyze the results.

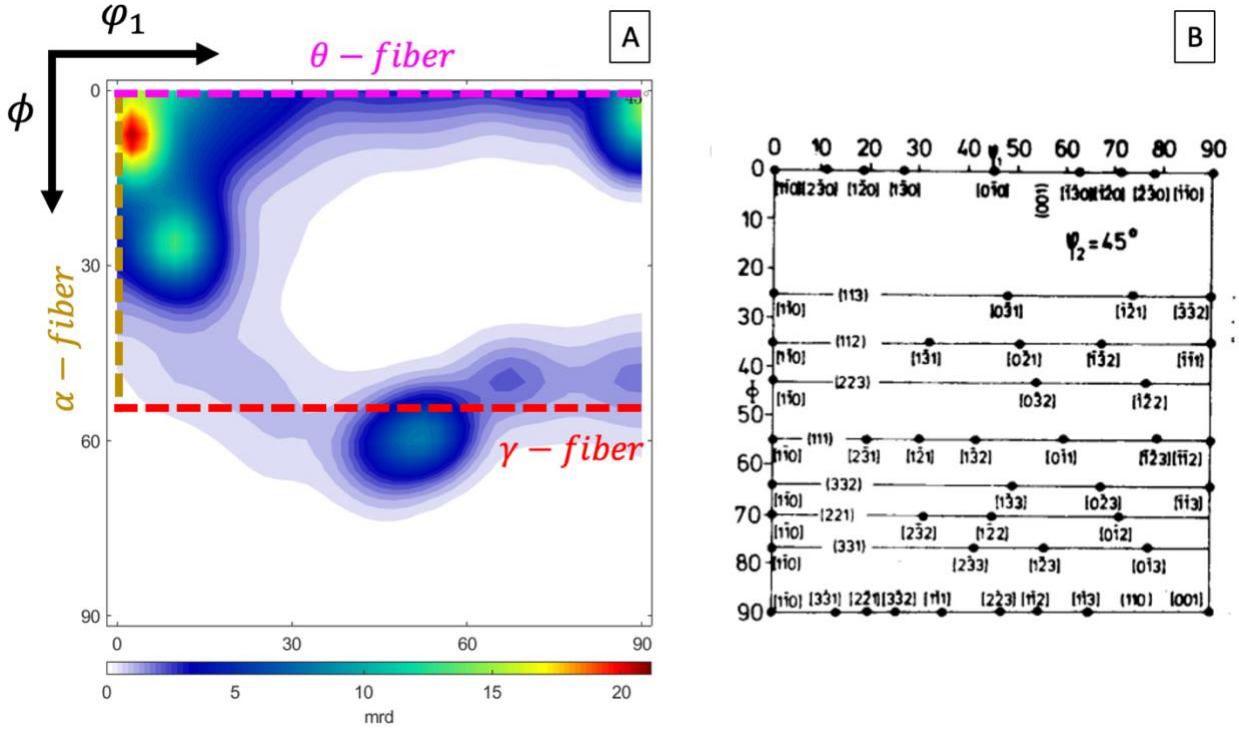

Figure 52 ODF section at $\varphi 2 = 45°$. A) experimental data for the rolled sample in the as-deformed condition. B) ODF showing ideal crystallographic orientations in the Euler space (from [51], with permission from Elsevier).

Based on the ODF shown in Figure 52A, the texture in the as-deformed condition is composed of the γ-fiber, the partial α-fiber, and the θ -fiber. The first two are typically seen in rolled samples of BCC materials. On the other hand, the θ -fiber is not as commonly reported, but it has been seen

in previous studies [37], [98], [106], [127]. Strong texture components are present in the as-deformed condition. Their peaks are located at (001)[$1\bar{1}0$] with an MRD of 21, (001)[$\overline{11}0$] with an MRD of 13, a component with an MRD of 13 deviated ~10° from (113)[$1\bar{1}0$], and a component with a MRD of 10 deviated ~5° from (111)[$0\overline{11}$]. Deviations in the texture components below 15° are generally seen on experimental data, and they can be due to errors in the experimental setup. The peak components are typical of a BCC rolled sample, although the MRDs are very high compared to results in literature which usually are around 7 – 10 [9], [99], [101], [102], [106], [110]. The high intensity of the texture components in the as-deformed conditions can be explained because of the severe microstructure heterogeneity discussed in section 6.2 and shown in Figure 43.

Some of the IPF maps obtained via EBSD for the rolled sample in the as-deformed conditions are shown in Figure 53. One can see in the maps two types of microstructures, a highly deformed with small grains phase and a long elongated with small deformation phase. The elongated grains are < 110 >//RD, and the small deformed matrix contains a series of different orientations with large portions of < 111 >//RD and some < 100 >//RD. In section 6.2, the author elaborated on the rolled sample microstructure heterogeneity. It was discussed that the as-deformed microstructure for the rolled sample was composed of zones of high deformation and zones of low deformation. The author commented that early studies stated that grains with low dislocation density are generally < 110 >//RD oriented, while darker grains, i.e., high dislocation density, usually have a < 111 >//RD orientations. The IPF maps shown in Figure 53 nicely corroborate the previous observations.

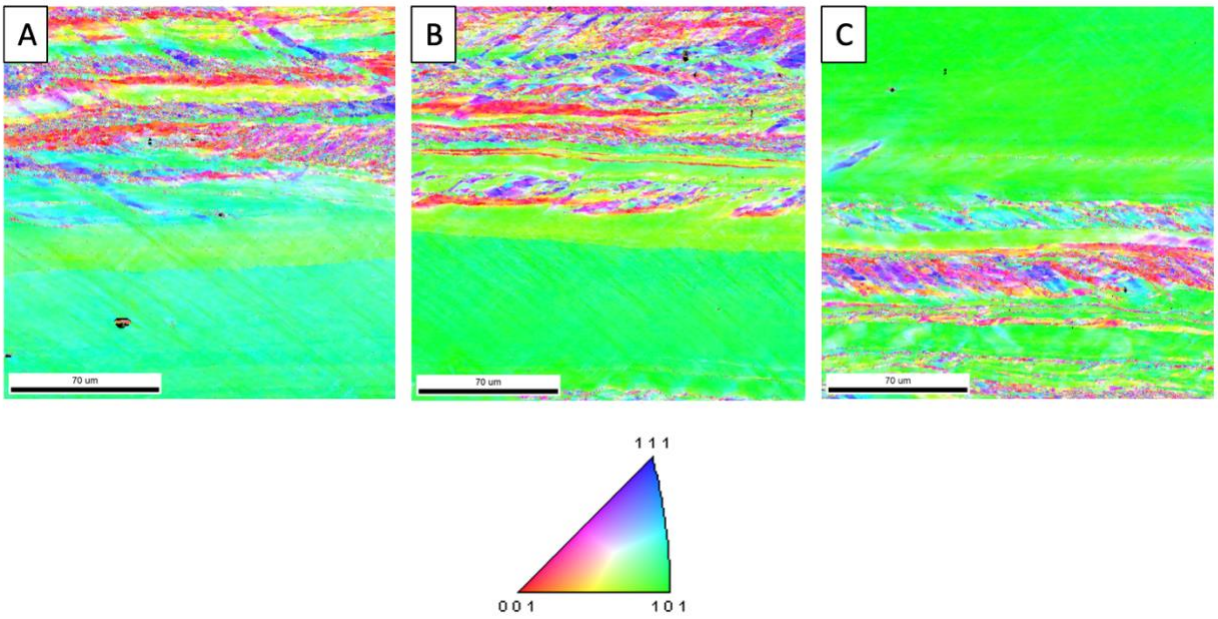

Figure 53 IPF maps parallel to the RD from rolled samples in the as-deformed condition. All the pictures belong to the same sample, but were taken at different positions.

Figure 54 is a compilation of ODF sections and IPF maps that summarize texture evolution in the rolled samples. This figure shows the data corresponding to three conditions, as-deformed, intermediate, and fully annealed. The analysis of the as-deformed has been explained already. Similarly, the texture of the intermediate and fully annealed samples can be presented using the ODFs sections. The ODF section at $\varphi 2 = 45°$ shown in Figure 54B depicts the texture of the intermediate annealed sample. The literature describes the texture of rolled samples after recrystallization as similar to the ones shown for the as-deformed condition [52]. Results shown in Figure 54B agree with what has been described in the literature. The γ-fiber is weaker, having only some of the texture components while missing the $(111)[0\bar{1}\bar{1}]$ orientations as well as the $(111)[\bar{1}\bar{1}2]$. The maximum intensity is located at $(111)[1\bar{2}1]$, but the MRD is approximately 5, much lower than what was shown in the as-deformed condition. On the other hand, the α and θ-fibers remain similar to the as-deformed condition, with just a few changes in the peaks with maximum intensity. All these changes result from the recrystallization of new grains in the dark zones (high deformation) and the reduction of the elongated white zones (low deformation). This effectively reduced the intensity of the <110> peaks, and it even shifted some of them. Finally, the ODF section at $\varphi 2 = 45°$ shown in Figure 54C depicts the texture of the fully annealed sample.

This ODF is considerably different to the previous two. You can still trace the three γ, α, and θ -fibers but in this case, intensities are more spread throughout the Euler space. Furthermore, the highest MRD in this section is only around 2.5, which is considered weak, especially compared to the other two conditions. One can say that the texture of the fully annealed sample doesn't have a strong grain orientation, which is ideal for NGO electrical steel. The texture randomization of the samples is an effect of the normal grain growth and the consequent homogenization of the microstructure. The IPF map shown in Figure 54C agrees with this explanation.

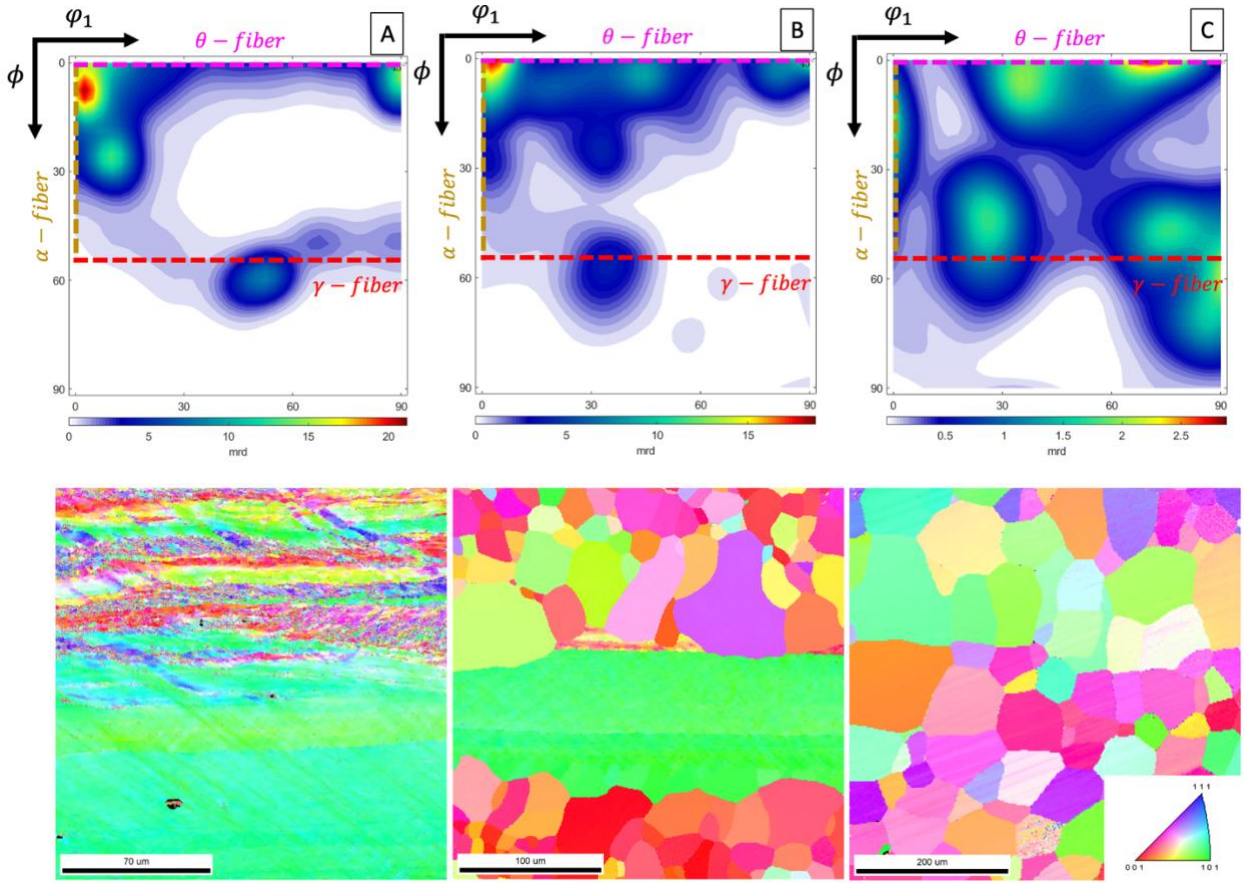

Figure 54 Texture evolution during annealing represented with ODFs at $\varphi 2 = 45°$ and IPF maps. A) as-deformed, B) intermediate annealing, and C) fully annealed.

HCE Strips

The texture analysis of the HCE samples requires a different perspective because machining-based sheet production has fundamental differences from rolling production. During machining, deformation happens via shearing. Shearing in machining is characterized by a narrow

deformation zone, high adiabatic temperatures, high hydrostatic pressures, and a different deformation path. For more details on deformation via machining, please go to section 2.7.
The literature on texture analysis of deformation via shearing in BCC materials has been widely explored for ECAP (equal channel angular pressing) more than for machining techniques. The deformation that occurs during ECAP and machining is similar, and one can use the ECAP models to explain the result on machining-based experiments.

There is some work on the texture analysis of Fe-Si alloys produced via machining [83], [84]. This work showed the texture evolution of Fe-4Si and Fe-6.5 wt% in machining operations using pole figure analysis. The authors demonstrated the relationship between the shear plane angle with respect to CFD and the {110} fiber angle with respect to the CFD. Additionally, they showed the different textures in the primary and secondary shear zones and the texture retention of the samples after recrystallization.

Following, the texture evolution of the machining-based sample of the Fe-4Si-4Cr will be presented. Results will be compared to the rolled samples.

Figure 55 shows the ODF section at $\varphi 2 = 45°$ of the as-deformed HCE sample. The standard $\varphi 2 = 45°$ ODF section ($\varphi_1 = 0 - 90°$, $\Phi = 0\text{-}90°$) is not as commonly used in studies of shearing texture. One can see that not much information can be obtained from Figure 55 since not many of the typical shearing texture components are present in this section, and the ones that you could find at $\varphi 2 = 45°$ are mainly located at the edges of the ODF section. Having the main orientation on the edge of the ODF sections is not ideal, especially considering that the peaks usually deviate some degrees from the ideal orientations. Table 6 contains the typical shearing texture components for BCC and their positions in the Euler space in shear deformation, and the notation of these orientations has been superimposed on Figure 55. The orientation components denote {hkl}parallel to the ND and <uvw> parallel to the RD. Figure 55 shows that only the $(\bar{1}\bar{1}0)[\bar{1}12]$ and the $(11\bar{2})[111]$ are represented in the ODF, despite both of them being deviated approximately 20°. A complete representation of shear deformation texture uses an ODF section at $\varphi 2 = 45°$ with $\varphi_1 = 0 - 360°$ and $\Phi = 0\text{-}90°$; this section will be called as the extended ODF. Experimental data of the HCE samples is shown in Figure 56 using extended ODF sections.

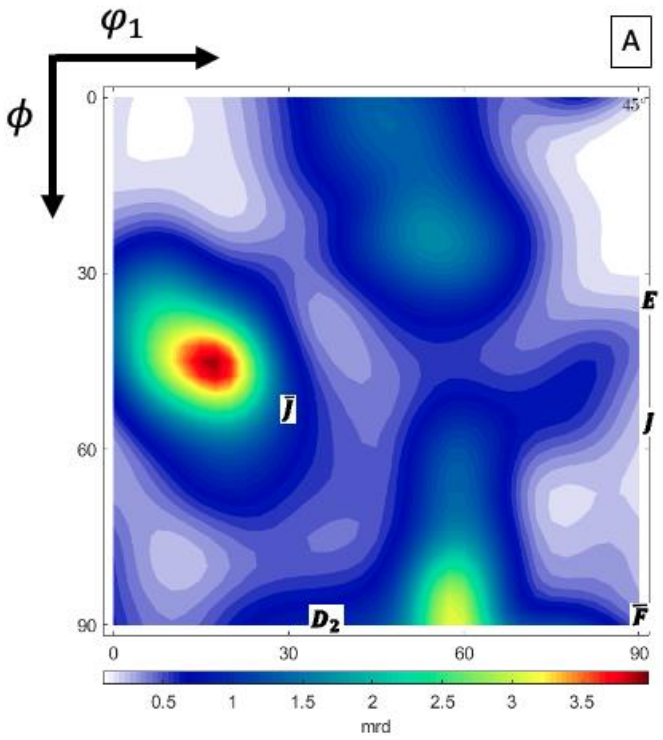

Figure 55 ODF section at $\varphi 2 = 45°$of experimental data for the HCE sample in the as-deformed condition.

Table 6 Typical orientation components in shear deformation of BCC metals (from [128], with permission from Elsevier).

Table 2
Main ideal orientations in simple shear deformation of bcc materials

Notation	$\{h\,k\,l\}\langle u\,v\,w\rangle$	Euler angles (°)[a]		
		φ_1	ϕ	φ_2
D_1	$(\bar{1}\,\bar{1}\,2)[1\,1\,1]$	54.74/234.74	45	0/90
		144.74	90	45
D_2	$(1\,1\,\bar{2})[1\,1\,1]$	125.26	45	0/90
		35.26/215.26	90	45
E	$(\underline{1}\,\underline{1}\,0)[1\,\bar{1}\,1]$	90	35.26	45
$\bar{E}$	$(1\,1\,0)[\underline{1}\,\underline{1}\,1]$	270	35.26	45
J	$(\underline{1}\,\underline{1}\,0)[1\,\bar{1}\,\underline{2}]$	90/210	54.74	45
$\bar{J}$	$(1\,1\,0)[\underline{1}\,\underline{1}\,2]$	30/150/270	54.74	45
F	$\{1\,1\,0\}\langle 0\,0\,1\rangle$	0/180	45	0/90
		90/270	90	45

[a] Given in the $\varphi_2 = 0°$, 45° and 90° sections with $\varphi_1 = 0$–270° only.

In Figure 56, the author superimposed the texture components from Table 6. It is possible to see that some of these typical shear deformation texture components match the HCE experimental data, with some of them slightly deviated. Notice that the D1 $(\bar{1}\bar{1}2)[111]$, D2 $(11\bar{2})[111]$ and F {110}<001> orientations are close to the texture peaks shown in Figure 56 in all the conditions. Also, at FA, there is a high-intensity peak close to $(110)[1\bar{1}2]$. The data here

presented matches the data found in the literature for ECAP deformation texture [129]–[131]. Considering that the <111> is the hardest direction of magnetization in α-iron, almost all the main orientations in simple shearing here presented are detrimental to the soft magnetic performance of HCE sheets. Just the orientation F {110}<001> (Goss texture) benefits magnetic properties, and it happens to be close to some texture peaks in the IA and FA conditions. Still, it does not correspond to the highest intensities.

Some reasons that can be attributed to the slight deviation are sample preparation, the initial high temperature of the HCE workpiece, the effect of the secondary shear zone, specially at the constraining zone in the sample, and variations in the strain path (that can be easily changed in HCE by varying lambda and alpha), and the initial workpiece texture.

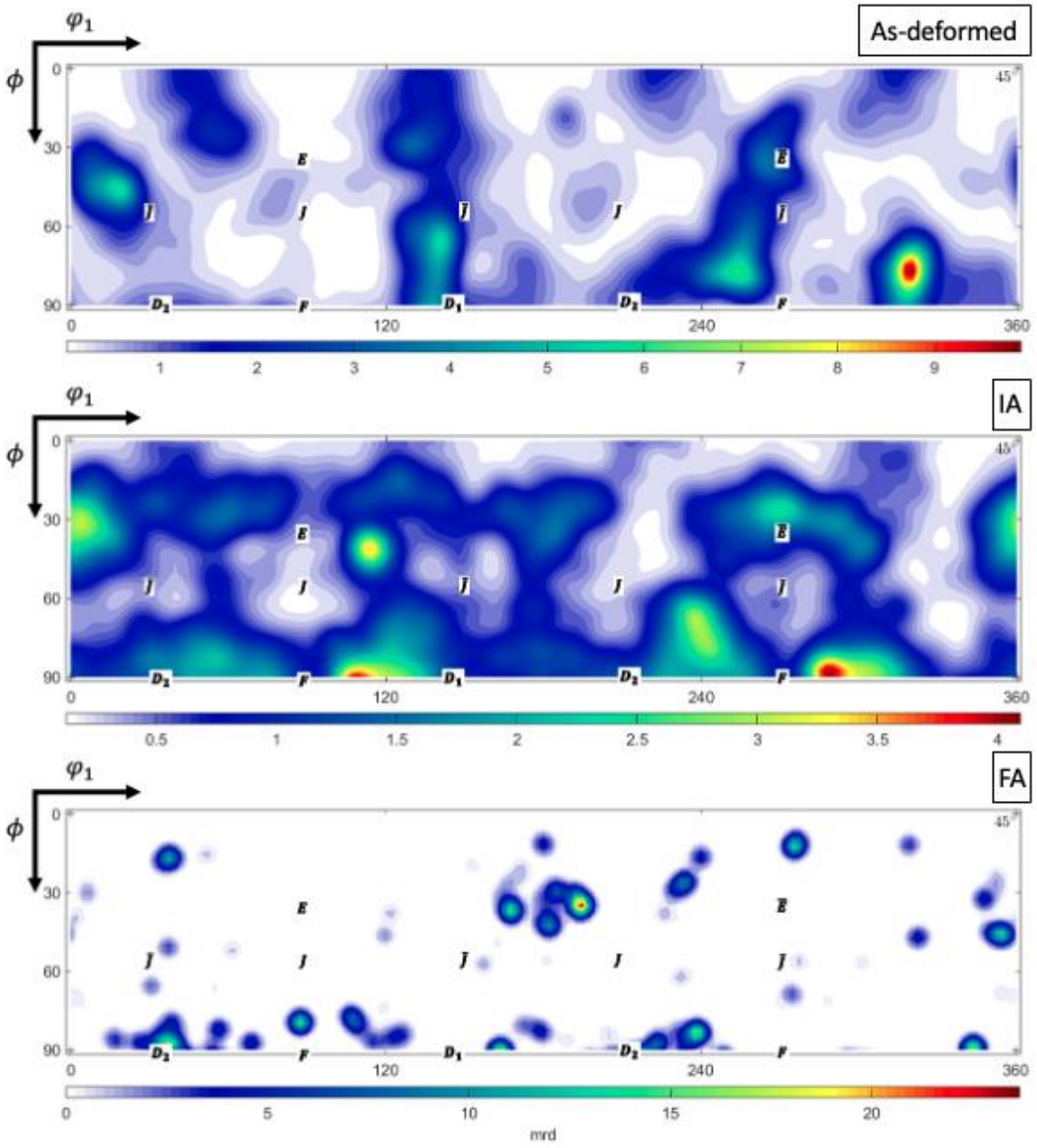

Figure 56 Texture evolution during recrystallization of Fe-4Si-4Cr HCE sample using extended ODF ($\varphi 1$= 0 - 360°) sections at $\varphi 2$ = 45°. On top the as-deformed materials, in the middle the intermediate annealing sample, and at the bottom is the fully annealed sample.

Finally, one common way found in the literature to represent texture in shear deformation processing is the pole figures, specifically the (110) pole figure.

Figure 57 is a schematic of a (110) pole on the plane z that illustrates all the main orientations in simple shearing shown in Table 6.

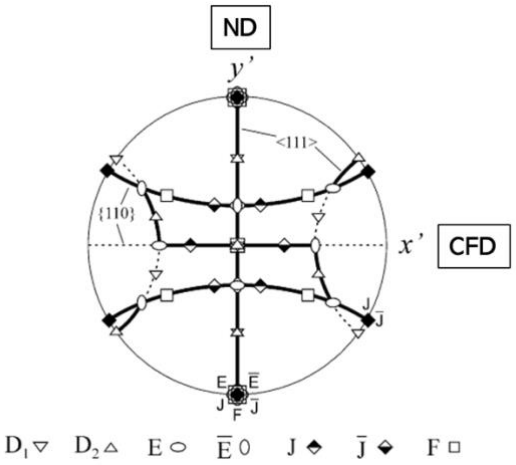

Figure 57 (110) pole figure on the plane z illustrating main ideal shear deformation orientations, partial {110} fiber, and the partial <111> fiber (from [128], with permission from Elsevier).

Figure 57 shows how using these orientations, one can construct a geometric representation of the partial{110}<uvw> and the {hkl}<111> fibers. More importantly, depending on the shearing conditions, one can estimate the angle between y' and the ND axis, which is the same as the angle between x' and the CFD axis. The later angle is important for electrical steel because it shows the angle between the {110} fiber and the CFD (or the RD if traditional electrical steel notation is considered). This concept has been explored already in previous investigations of machining-based production of electrical steels, and the results showed that HCE offers a unique texture control where the angle of the {110} fiber and the CFD can be engineered by varying the cutting parameters and the chip deformation path [83], [84]. The authors in these previous studies showed that there is a correlation between the {110} fiber - CFD angle and the shearing plane.

Figure 58 presents the (110) pole figures for the studied three conditions. Using the same geometric construction shown in Figure 57, the author identified the <111> fiber and measured the angle with respect to the ND. As previously discussed, this is the same angle between the {110} fiber and the CFD. Notice that the angle is similar for the three conditions, and the texture intensity is similar as well, which shows retention of texture for the three conditions based on the pole figures. The differences between the texture analysis using ODFs and pole figures is a consequence of the limitations of using a 2D representation for a 3D shape.

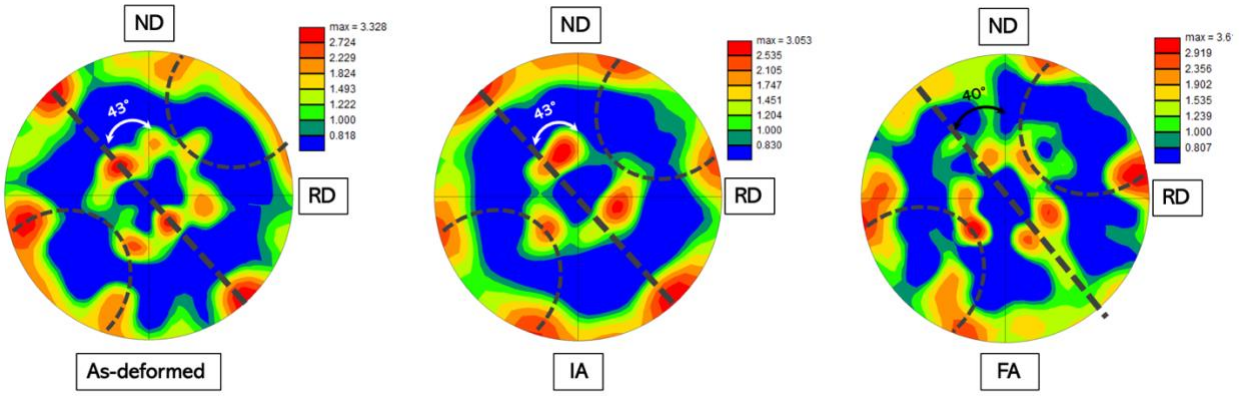

Figure 58 Texture evolution of HCE samples using (110) pole figures. As deformed, intermediate annealing, and fully annealed.

Everything considered, the texture of the rolled and the HCE samples have considerably different texture components. The two conditions retained the as-deformed texture well in the intermediate annealing but not as much after completing a full anneal as shown in Figure 54 and Figure 56. In the case of the rolled sample, it is possible to trace the original texture fibers (γ-fiber, the partial α-fiber, and the θ -fiber) in the fully annealed data, but the texture intensity is weak. On the other hand, the texture of the fully annealed HCE sample changes as compared to the deformed conditions, and one of the features that highlight is the presence of a peak of approximately 25 mrd located close to $(110)[1\bar{1}2]$.

7. MAGNETIC PROPERTIES

7.1 Background

One of the specific objectives of this project is to produce Fe-Si-Cr sheet with core loss lower than commercial benchmark Fe-3.2Si wt% or M19. For this purpose, a new electrical steel alloy was developed with better magnetic performance than ~Fe-3.2Si wt% and good workability. Fe-3.2Si wt% is selected as a control alloy because this is the composition with the highest Si content in large-scale industrial use. Table 7 contains detailed information on the magnetic properties of commercial M-19. Also, Table 7 shows the magnetic properties data for an alloy called DI-MAX HF-10x, a material that will be explained later in this chapter.

Table 7 Commercial control samples. DI-MAX HF-10x, M19 (0.35mm) [54], [55], [132]–[135].

Property	**DI-MAX HF-10X (0.25 mm) AK Steel**	**M19 (0.35 mm) AK Steel**
ρ (μΩ · cm)	60	55
Core loss (W/kg; 1.5 T; 60 Hz)	2.46	3.48
Core loss (W/kg; 1.5 T; 400 Hz)	29.6	42
Saturation Induction (T)	1.97	1.99
Hardness (Vickers)	193	180
Density (g/cm^3)	7.6	7.65
Yield Strength (MPa)	440	421
Composition (wt%)		3.3%(Si + Al)
Grain Size (μm)	60	170

Magnetic properties characterization was performed at Magnet-Physics Inc in Indianapolis, following ASTM A773/A773M-21 for DC testing and ASTM A927/A927M-18 for AC testing.

To evaluate the magnetic properties of the Fe-4Si-4Cr experimental alloy, rolled and machining-base samples were used. In addition to the experimental samples, a commercial material was also tested. The technique used to evaluate the magnetic properties is called the toroidal test (for more details about the test, please go to the experimental section in this chapter). This technique requires rings of electrical steel sheet to stack them up and form a small magnetic core. Figure 59 shows a schematic of the magnetic core and the rings used in this experiment.

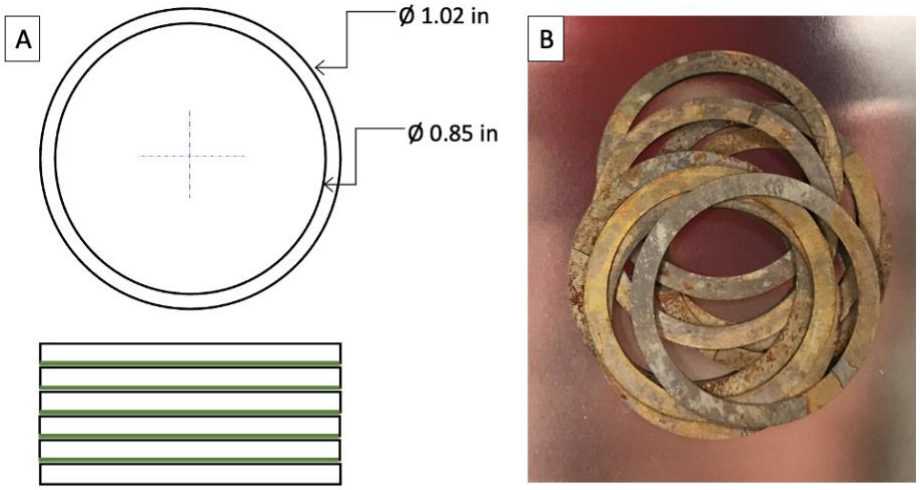

Figure 59 A) Schematic of the toroidal testing setup used in this project, and B) Fe-4Si-4Cr rings produced for magnetic testing via EDM.

Chapter 4 explained that the maximum width available for machining-based strips of the experimental alloy was 2 in. This was a limitation to the size of the ring samples. There are some restrictions related to the geometry of the rings used for the toroidal test, like for example the ratio between the outside diameter and inside diameter. Still, there is no minimum or maximum ring size defined in the ASTM standard. However, in practice, a very small ring size is not desired because of the low intensity of magnetic flux close to the center of the toroid. For this purpose, in this research work, the minimum outside diameter that could be tested was 1.02 in. Figure 38 shows the 50 mm FM+R strip of Fe-4Si-4Cr. This sample is the widest sample produced using the hybrid processing technique and is the sample that was used to test magnetic properties for machining-based conditions. The thickness of this sample is ~205 μm, which is lower than the minimum available thickness of commercial M-19 (0.36 mm). Bertotti's model shown in Equation 2-1 illustrates the effect of the sheet thickness on the core losses. Basically, the higher the thickness, the higher the eddy current losses. Knowing this, a new restriction for the samples is

defined based on the thickness of the FM+R sample. In other words, the rolled and commercial samples must have similar sheet thickness to the FM+R one. Table 7 contains detailed information on a commercial alloy called DI-MAX HF-10x which, to the author's knowledge, is the most similar to the M19 commercial alloy for a thickness close to 205 μm.

In this chapter, the magnetic properties of the Fe-4Si-4Cr experimental alloy are tested and compared to a control sample of the commercial alloy DI-MAX HF-10x.

7.2 Experimental methods

The magnetic properties characterization was performed at Magnet-Physics Inc in Indianapolis. To evaluate the magnetic properties of the Fe-4Si-4Cr experimental alloy, three conditions were identified as FM+R (free machining + light rolling), rolled (rolled sample of Fe-4Si-4Cr), and commercial alloy (DI-MAX HF-10x).

The details on the production of the FM+R samples are presented in chapter 5 (see Figure 33). The ingot for the rolled sample (as well as the FM+R) was obtained from Sophisticated Alloys Inc and more detailed information is available in section 4.1.1. The samples were hot rolled from 10 mm to 2 mm. After hot rolling, the plates were cold rolled to 400 μm with an intermediate annealing of 5 minutes at 800 °C. To obtain a final thickness of ~200 μm, the samples were "sandwiched" between laminations of the same material and further cold rolling was done. The commercial alloy sheet was obtained from AKSteel in the fully processed condition.

EDM was used to cut the rings for magnetic testing from each material (see Figure 59). After cutting the samples via EDM, the rings were heat treated at 800 °C for 1 h in a convection furnace with no atmosphere control. An oxidation layer was formed after the heat treatment and it is shown in see Figure 59. A thin layer Rust-Oleum-brand Crystal Clear Enamel spray was applied to one side of each lamination ring. This coating in addition to the thin oxidation layer were used to electrically isolate the different laminations of the stack.

The mass of the testing specimens was obtained using a scale with 0.001 g accuracy. The inner and outside diameter was obtained using a caliper with 0.01 mm resolution. The material density was obtained using the principle of Archimedes. This data was used to calculate the packing factor and the cross-sectional area of the actual testing material.

The DC or quasi-static B-H loop was measured. The AC core loss curves was tested at frequencies of 60 Hz and 400 Hz and to magnetization levels from near zero up to the flux density level where the form factor of the flux waveform was approximately 1.14.

DC testing was performed using a Magnet-Physik Model Remagraph C-500 Soft Magnetic Test System for DC magnetic properties in accordance with ASTM A773/A773M-21 Standard Test Method for Direct Current Magnetic Properties of Low Coercivity Magnetic Materials Using Hysteresis Graphs, and IEC 60404-4. Typical measurement uncertainty for ring measurements is approx. ± 1% for B and ± 1% for H.

AC testing was performed using a Magnet-Physik Model Remacomp C-1200 test system which corresponds to ASTM A927/A927M-18 Standard Test Method for Alternating-Current Magnetic Properties of Toroidal Core Specimens Using the Voltmeter-Ammeter-Wattmeter Method, and IEC 60404-6 (digital method).

7.3 Results and analysis

One could say that the first results on magnetic properties in this thesis have already been shown in chapter 3. The resistivity measured for Fe-4Si-4Cr wt% was **85 ± 3 μΩ·cm.** Strictly speaking, electrical resistivity is an electrical property of a material rather than a magnetic property. Nevertheless, as previously discussed and explicitly shown in Equation 2-1, the electrical resistivity significantly impacts the eddy current losses, which are the most important core loss at high frequencies. The electrical resistivity target was 80 μΩ·cm based on the value of Fe-6.5Si wt%, and the Fe-4Si-4Cr alloy showed a slightly higher resistivity than the targeted value.

There are studies that explored the concept of ideal grain size for electrical steel alloys [112], [136]–[140]. These studies agree that there is an optimal grain size that reduces total core losses to a minimum. However, the optimal grain size changes due to variations in alloy composition, texture, strip thickness, and impurities. There is no comprehensive literature on the ideal grain size of thin (<0.36 mm) commercial electrical steel. Figure 60 shows the microstructure of a fully-processed commercial electrical steel (DI-MAX HF-10X) with a thickness of 0.25 mm. The average grain size of the commercial alloy is 60 μm, which is about ¼ of the strip thickness. This grain size-thickness relationship agrees with data seen in the literature. Grain boundaries are known for being deleterious to the motion of the magnetic domain walls; thus, the bigger the grain

size, the better the magnetic properties. However, having grains of a size equal to the strip thickness is detrimental to the magnetic properties as well. There is a reason why the ideal grain size should be a fraction of the total strip thickness, and it is related to the anisotropy of α-iron. If one has a material with grains as big as the strip thickness, there is a possibility that some of those grains will have the hard direction of magnetization aligned to the RD. Having a smaller grain size reduces the likelihood of this happening.

The microstructure targeted for the FM and the rolled sample is also shown in Figure 60. The average grain size for the commercial material is 60 µm, for the FM+R sample is 50 µm, and 70 µm for the rolled sample.

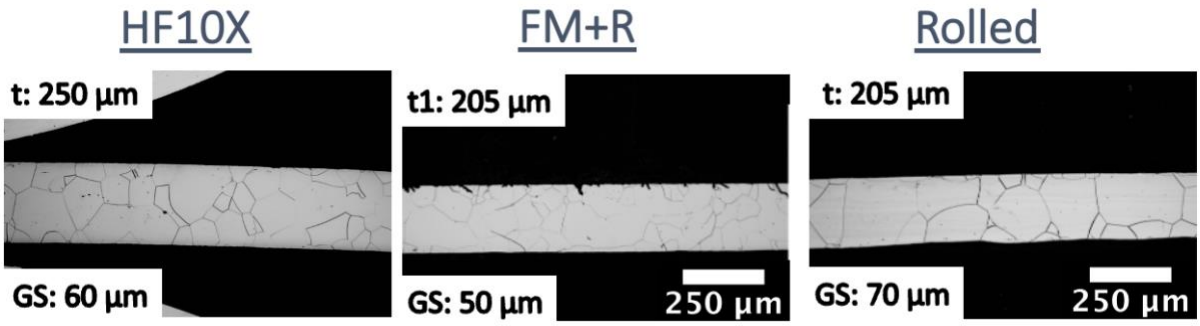

Figure 60 Side-view microstructure of samples prepared for magnetic testing of commercial alloy (DI-MAX HF-10X), experimental alloy in machined (FM+R) and rolled conditions.

The microstructure of the actual samples used for magnetic testing was evaluated via EBSD. Some results are shown in Figure 61. The HF10X and the rolled sample effectively resemble the microstructures shown in Figure 60. In contrast, the FM+R sample has a coarser microstructure. The coarse grain size is detrimental to the magnetic performance of the FM+R sample.

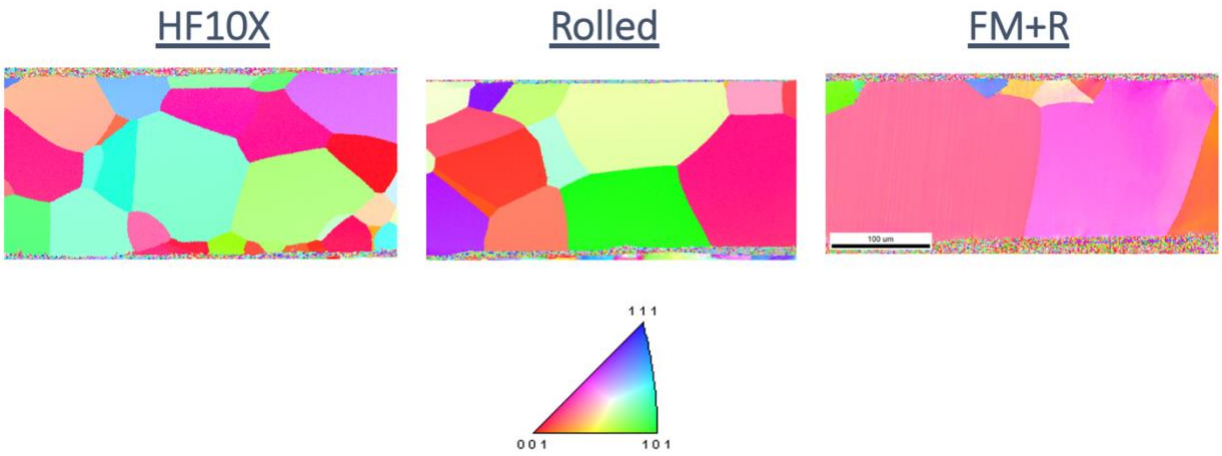

Figure 61 Microstructure of the three samples here studied, DIMAX HF10X, and experimental alloy produced FM+R, and rolled. Characterization done via EBSD with the crystallographic directions parallel to RD.

The magnetic properties that characterize soft magnetic materials are a high magnetic permeability and flux saturation, and a low coercivity, core loss, and magnetostriction. DC testing results are shown in Figure 62. The DC loops are useful to evaluate the magnetic permeability, coercivity, and flux saturation.

Due to the non-linearity of the magnetic permeability, there are many ways to report it. In this work, the magnetic permeability is reported using B values accompanied by their correspondent H. B5 [T] (B at H=500 A/m) is equal to 1.21, 1.17, and 1.25 T for the commercial alloy, the FM+R, and the rolled sample, respectively. Also, B20 [T] (B at H=2000 A/m) is equal to 1.44, 1.35, and 1.37 T for the commercial alloy, the FM+R, and the rolled sample, respectively. These results are also presented in Table 8 for more clarity. The permeabilities along the three samples at B5 and B20 are similar. The sample with the lowest magnetic permeability at the two conditions is the FM+R sample. The commercial and the rolled sample switch places at B5 and B20.

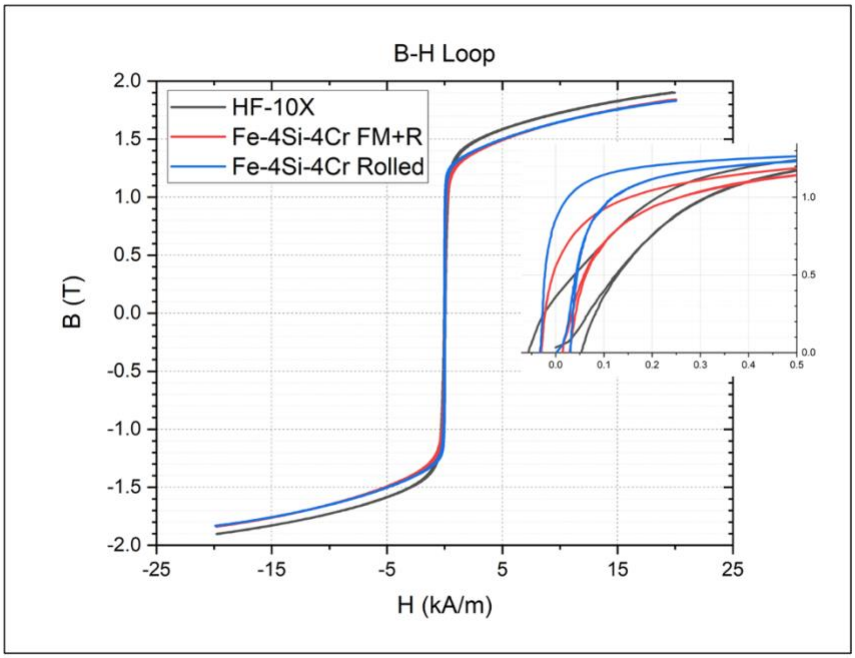

Figure 62 DC testing results of the three sample conditions. The figure also shows a zoom-in of the first quadrant that illustrates some of the magnetic properties in more detail.

The B_{max} for the commercial alloy, the FM+R, and the rolled sample are 1.9, 1.84, and 1.83T, respectively. These values are within the range of traditional electrical steel B_{max}. The parameter determining the magnetic flux saturation in electrical steel is the Fe at% in the alloy. The samples of the experimental alloy have the same Fe at% (Fe-4Si-4Cr wt% = Fe-7.6Si-4.1Cr at%) and assuming a Fe-3.2Si wt% (Fe-6.7Si at%) for the commercial alloy; one can say that the commercial alloy has higher Fe at%.

The magnetic core losses of the experimental alloy in the FM+R and rolling conditions and the DIMAX HF-10X alloy are shown in Figure 63. Overall, it is possible to see that the experimental alloy samples have a lower core loss over all the range of B(T) at the two frequencies. The rolled sample has the lowest core loss, but the difference between the FM+R and the rolled sample is slight (~5%). A 5% difference is small and it could be experimental uncertainty. There is also the possibility that the difference is due to the texture and the surface roughness of the samples benefiting the rolled condition. The differences in the surface quality of the FM+R and rolled samples can be seen in Figure 60. It is possible that the small discontinuities on the constraint face (roughness of the grooves due to incomplete smoothing by rolling) of the FM+R sample act as disturbance for the magnetic flux, creating points of discontinuity which is not beneficial for

the magnetic core. Also, previous studies on magnetic properties of machining-based electrical steel samples demonstrated that during shear deformation, the partial <111> fiber strongly influences the magnetic properties [74], and considering the anisotropy of α-iron, the influence turns out to be detrimental.

The core loss reduction of the Fe-4Si-4Cr rolled sample compared to DIMAX HF-10X is ~28% at 60 Hz and ~35% at 400 Hz. The core loss reduction difference at the two frequencies is related to the higher electrical resistivity of the experimental alloy. Its core loss reducing effect is more noticed at higher frequencies. The magnetic properties studied in this work are summarized in Table 8.

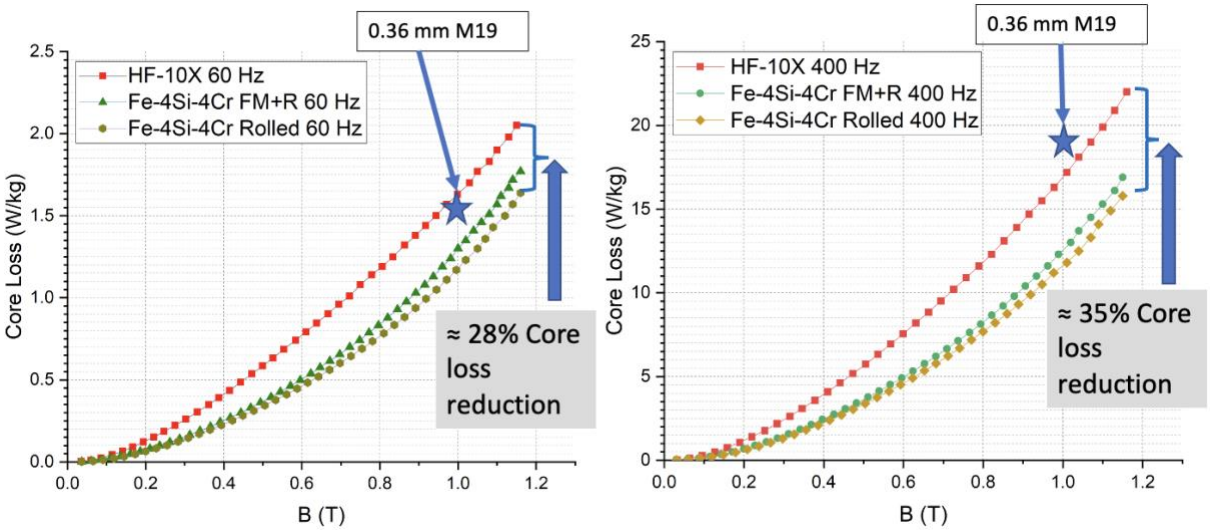

Figure 63 Core losses as a function of the flux density for the DIMAX HF-10X, FM+R, and rolled sample at 60 and 400 Hz. Comparison between the different conditions and commercial reported value of M19 (0.36 mm).

This chapter confirms that the Fe-4Si-4Cr experimental alloy has better magnetic performance than high silicon commercial alloys. The benefits of the magnetic performance of Fe-4Si-4Cr are even more significant at higher frequencies. Based on the calculations of the DOE [1], a reduction of 37% in core losses of electrical motors would save approximately 0.44% of all the electrical energy consumed in the US. This chapter shows that the Fe-4Si-4Cr is close to the 37% core loss reduction claimed by the DOE.

Table 8 Summary of all the magnetic properties examined for the three studied samples DIMAX HF-10X, and Fe-4Si-4Cr in the FM+R and rolled conditions.

Parameters	**HF-10X**	**FM+R**	**Rolled**
$\boldsymbol{\rho}$ $[\boldsymbol{\mu\Omega \cdot cm}]$	60	85	85
$\boldsymbol{B_{max}}$ **[T]**	1.9	1.84	1.83
$\boldsymbol{B5}$ **[T]**	1.21	1.17	1.25
$\boldsymbol{B20}$ **[T]**	1.44	1.35	1.37
$\boldsymbol{H_{CB}}$ **[A/m]**	54.9	29.3	31.3
Core Loss [W/kg] @ 1T & 60 Hz	1.7	1.3	1.2
Core Loss [W/kg] @ 1T & 400 Hz	17.2	13	11.8

8. CONCLUSIONS

The development of a new high-resistivity electrical steel alloy was studied in this thesis work. Also, the implementation and scale up of machining-based technology for electrical steel strip production was demonstrated.

A new experimental alloy Fe-4Si-4Cr wt% was developed with an electrical resistivity of 85 ± 3 $\mu\Omega \cdot cm$, which is higher than the ideal high-silicon alloy, Fe-6.5%Si. The workability experiments of the Fe-4Si-4Cr experimental alloy showed that rolled strips of this new alloy can be produced, in contrast of Fe-6.5Si. Results also showed that this new alloy can withstand >75% cold-rolled reduction.

The magnetic properties obtained via standard stacked toroidal test showed that this new alloy can have a 25% and 33% core loss reduction at 60 and 400 Hz respectively, compared to commercial benchmark alloy with ~ Fe-3.2Si wt%.

Strips of the Fe-4Si-4Cr experimental alloy were produced via machining-based techniques FM and HCE. Strips with a maximum width of 50 mm were produced with a combination of FM and light rolling with a surface roughness comparable to cold-rolled sheets with S_a = 2.75 µm in the free face, and S_a = 0.56 µm in the rake face.

The recrystallizations kinetics of Fe-4Si-4Cr in the rolled and HCE conditions were studied. Annealing maps were developed to summarize in a picture the different stages of the recrystallization process. It was demonstrated that the rolled and the HCE samples retain the as deformed texture well in the intermediate annealing but not as much after completing a full anneal. The rolled sample was characterized for the texture fibers γ-fiber, the partial α-fiber, and the θ-fiber. On the other hand, the texture of the HCE sample matched some of the ideal shear deformation textures with the presence of a peak of approximately 25 mrd located close to $(110)[11\bar{2}]$ in the fully annealed condition.

9. FUTURE WORK

The future work that is proposed can be divided into two fronts: 1) alloy development and 2) machining-based production of electrical steel sheet/strip.

Alloy Development

The results showed that magnetic core losses in electrical steel could be reduced by developing a new high-resistivity Fe-Si-Cr alloy that considerably lowers the eddy current losses. Additional future work can resolve a method to integrate these high-resistivity Fe-Si-Cr alloys into production using the existing manufacturing system of conventional electrical steels. The work in this thesis was at the laboratory scale, and new challenges would come into play if this alloy is introduced into the traditional rolling system. One challenge that stands out is the purity of the initial elements and the necessity to perform decarburization annealing to reduce C wt% to < 50 PPM to avoid magnetic aging. A systematic decarburization study is critical, and this characterization is yet to be done for any Fe-Si-Cr alloy.

In this project, the Fe-4Si-4Cr experimental alloy was explored—other alloys with lower Si% and higher Cr% promise similar magnetic properties but much better workability. A partial study has been carried out by the visiting scholar Theylor Amaya and the author of this thesis, where alternative compositions were explored, and performance was evaluated in terms of electrical resistivity and ductility in a tensile test. The study showed five different alloys with Si wt%<4w% and Cr wt%>4%, with electrical resistivity $\geq 80\ \mu\Omega \cdot cm$, and an improvement of ductility by increasing Cr wt% and reducing Si wt%. The next step in this study is to systematically evaluate the magnetic performance of these experimental alloys compared to Fe-3.2Si, and Fe-4Si-4Cr.

Machining-based production

The results showed that it is possible to produce strips up to 50 mm wide using hybrid deformation processing (combination of machining-based technique and light rolling). However, there are challenges in the process that should be addressed to facilitate a transition to even wider sheets. One critical challenge is the cutting tool damage evidenced during the processing of Fe-

4Si-4Cr wide strips via HCE. Additional work should include a study of the cutting tool performance where parameters like edge radius, composition, geometry, and manufacturing post-processing (grinding of the tool edge) are explored systematically to optimize the machining-based production. Also, a direct comparison of the commercial cutting tools and the experimental tooling used for FM and HCE will help identify characteristics that are important to enhance the performance of the experimental cutting tools.

Finally, a systematic study of the starting workpiece grain size effect on machining-based production of intermediate strips (12 – 25 mm width) will improve the understanding of the critical deformation phenomena and further optimization of the machining-based processes.

APPENDIX HARDNESS DATA FOR RECRYSTALLIZATION KINETICS EXPERIMENTS

Rolled Sample Hardness Data (HV0.5)

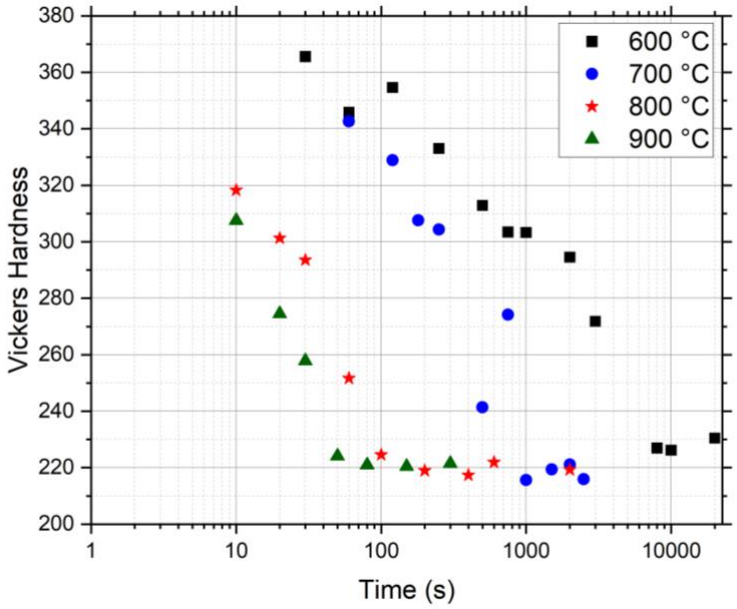

HCE Sample Hardness Data (HV0.5)

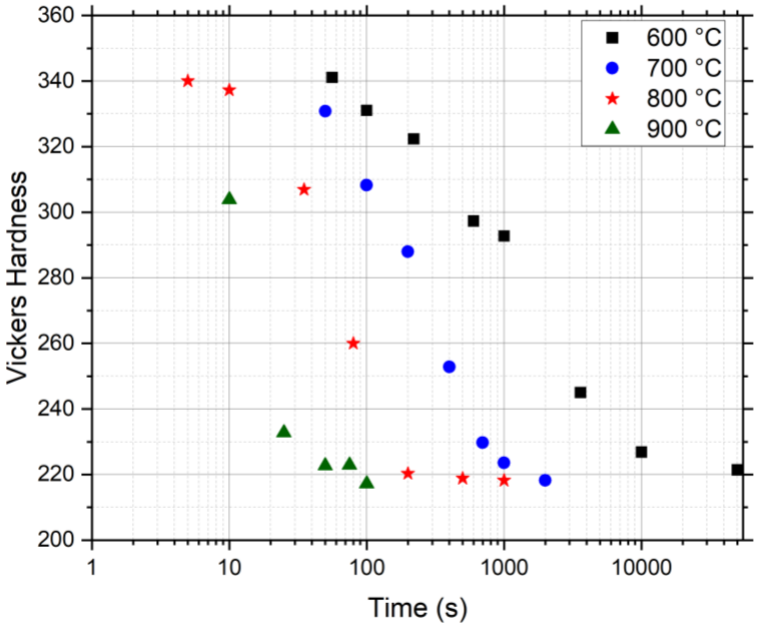

REFERENCES

[1] DOE, “Development of New Steel Alloy to Reduce Core Losses in Electric Motors,” 2017.

[2] V. M. Hernández-Guzmán, R. Silva-Ortigoza, and J. A. Orrante-Sakanassi, “Permanent Magnet Synchronous Motor,” *Adv. Ind. Control*, no. November 2010, pp. 97–203, 2021, doi: 10.1007/978-3-030-58786-4_4.

[3] A. J. Moses, “Electrical steels. Past, present and future developments,” *IEE Proc. A Phys. Sci. Meas. Instrumentation. Manag. Educ. Rev.*, vol. 137, no. 5, pp. 233–245, 1990, doi: 10.1049/ip-a-2.1990.0039.

[4] V. Mânescu, G. Pâltânea, and H. Gavrilâ, “Non-Oriented Silicon Iron Alloys – State of the Art and Challenges,” *Rev. Roum. Sci. Techn.-Electrotechn. Energ.*, vol. 59, pp. 371–380, 2014, doi: 10.5923/j.eee.20120206.07.

[5] G. Tian and X. Bi, “Fabrication and magnetic properties of Fe-6.5% Si alloys by magnetron sputtering method,” *J. Alloys Compd.*, vol. 502, no. 1, pp. 1–4, 2010, doi: 10.1016/j.jallcom.2010.02.175.

[6] J. Schoen, S. Robert, and S. Glenn, “Method of continuously casting electrical steel strip with controlled spray cooling.,” U.S. Patent No. 6,739,384.

[7] S. Kasai, M. Namikawa, and T. Hiratani, “Recent progress of high silicon electrical steel in JFE steel,” *JFE Tech. Rep.*, vol. 21, no. 21, pp. 14–19, 2016.

[8] T. Ros-Yañez, Y. Houbaert, and V. Gómez Rodríguez, “High-silicon steel produced by hot dipping and diffusion annealing,” *J. Appl. Phys.*, vol. 91, no. 10 I, pp. 7857–7859, 2002, doi: 10.1063/1.1449445.

[9] H. Li, H. Liu, Z. Liu, H. Lu, H. Song, and G. Wang, “Characterization of microstructure, texture and magnetic properties in twin-roll casting high silicon non-oriented electrical steel,” *Mater. Charact.*, vol. 88, pp. 1–6, 2014, doi: 10.1016/j.matchar.2013.11.014.

[10] X. D. He, X. Li, and Y. Sun, “Microstructure and magnetic properties of high silicon electrical steel produced by electron beam physical vapor deposition,” *J. Magn. Magn. Mater.*, vol. 320, no. 3–4, pp. 217–221, 2008, doi: 10.1016/j.jmmm.2007.05.030.

[11] Y. Takada, M. Abe, S. Masuda, and J. Inagaki, “Commercial scale production of Fe-6.5 wt. % Si sheet and its magnetic properties,” *J. Appl. Phys.*, vol. 64, no. September 1998, 1998, doi: https://doi.org/10.1063/1.342373.

[12] T. Ros-Yáñez, D. Ruiz, J. Barros, and Y. Houbaert, “Advances in the production of high-silicon electrical steel by thermomechanical processing and by immersion and diffusion annealing,” *J. Alloys Compd.*, vol. 369, no. 1–2, pp. 125–130, 2004, doi: 10.1016/j.jallcom.2003.09.070.

[13] S. Molafilabi, A. Sadeghi, and M. Hadad, “Investigation of large strain extrusion machining (LSEM) of pure magnesium (Mg),” *Int. J. Light. Mater. Manuf.*, vol. 3, no. 2, pp. 100–107, 2020, doi: 10.1016/j.ijlmm.2019.09.001.

[14] A. B. Kustas, D. R. Johnson, K. P. Trumble, and S. Chandrasekar, “Enhancing workability in sheet production of high silicon content electrical steel through large shear deformation,” *J. Mater. Process. Technol.*, vol. 257, no. February, pp. 155–162, 2018, doi: 10.1016/j.jmatprotec.2018.02.027.

[15] D. Sagapuram, M. Efe, K. P. Trumble, and S. Chandrasekar, “Enabling shear textures and fine-grained structures in Magnesium sheet by machining-based deformation processing,” *IOP Conf. Ser. Mater. Sci. Eng.*, vol. 63, no. 1, pp. 0–10, 2014, doi: 10.1088/1757-899X/63/1/012155.

[16] E. P. Gnanamanickam, S. Lee, J. P. Sullivan, and S. Chandrasekar, “Direct measurement of large-strain deformation fields by particle tracking,” *Meas. Sci. Technol.*, vol. 20, no. 9, 2009, doi: 10.1088/0957-0233/20/9/095710.

[17] M. Efe, W. Moscoso, K. P. Trumble, W. Dale Compton, and S. Chandrasekar, “Mechanics of large strain extrusion machining and application to deformation processing of magnesium alloys,” *Acta Mater.*, vol. 60, no. 5, pp. 2031–2042, 2012, doi: 10.1016/j.actamat.2012.01.018.

[18] T. L. Brown *et al.*, “A study of the interactive effects of strain, strain rate and temperature in severe plastic deformation of copper,” *Acta Mater.*, vol. 57, no. 18, pp. 5491–5500, 2009, doi: 10.1016/j.actamat.2009.07.052.

[19] Y. Guo, M. Efe, W. Moscoso, D. Sagapuram, K. P. Trumble, and S. Chandrasekar, "Deformation field in large-strain extrusion machining and implications for deformation processing," *Scr. Mater.*, vol. 66, no. 5, pp. 235–238, 2012, doi: 10.1016/j.scriptamat.2011.10.045.

[20] M. Komatsubara, K. Sadahiro, O. Kondo, T. Takamiya, and A. Honda, "Newly developed electrical steel for high-frequency use," *J. Magn. Magn. Mater.*, vol. 242–245, pp. 212–215, 2002, doi: 10.1016/S0304-8853(01)01164-7.

[21] B. S. Puentes Rodriguez, D. Brice, J. B. Mann, S. Chandrasekar, and K. Trumble, "Production of High-Resistivity Electrical Steel Alloys by Substitution of Si with Al and Cr," in *TMS 2019 148th Annual Meeting & Exhibition Supplemental Proceedings*, 2019, pp. 599–606.

[22] K. Narita, N. Teshima, Y. Mori, and M. Enokizono, "Recent researches on high silicon-iron alloys," *IEEE Trans. Magn.*, vol. 17, no. 6, pp. 2857–2862, 1981, doi: 10.1109/TMAG.1981.1061740.

[23] P. A. Beck and P. R. Sperry, "Strain induced grain boundary migration in high purity aluminum," *J. Appl. Phys.*, vol. 21, no. 2, pp. 150–152, 1950, doi: 10.1063/1.1699614.

[24] J. C. Perrier and P. Brissonneau, "Some physical and mechanical properties of SiAlFe alloys," *J. Magn. Magn. Mater.*, vol. 26, pp. 79–82, 1982, doi: https://doi.org/10.1016/0304-8853(82)90121-4.

[25] M. Ohring, "Engineering Materials Science. - Chapter 7 Mechanical Behavior of Solids," *Eng. Mater. Sci.*, pp. 299–V, 1995, doi: 10.1016/b978-012524995-9/50031-3.

[26] D. Hull and D. J. Bacon, "Introduction to dislocations - Chapter 3 Movement of Dislocations," *Elsevier*, pp. 43–62, 2011, doi: 10.1016/b978-0-08-096672-4.00003-7.

[27] C. R. Weinberger, B. L. Boyce, and C. C. Battaile, "Slip planes in bcc transition metals," *Int. Mater. Rev.*, vol. 58, no. 5, pp. 296–314, 2013, doi: 10.1179/1743280412Y.0000000015.

[28] T. B. Britton, F. P. E. Dunne, and A. J. Wilkinson, "On the mechanistic basis of deformation at the microscale in hexagonal close-packed metals," *Proc. R. Soc. A Math. Phys. Eng. Sci.*, vol. 471, no. 2178, 2015, doi: 10.1098/rspa.2014.0881.

[29] A. You, M. A. Y. Be, and I. In, "Si sheet and its magnetic properties," vol. 5367, no. September 1998, pp. 8–11, 2012.

[30] C. S. Li, C. L. Yang, G. J. Cai, and Q. W. Wang, “Ordered phases and microhardness of Fe-6.5%Si steel sheet after hot rolling and annealing,” *Materials Science and Engineering A*, vol. 650. pp. 84–92, 2016, doi: 10.1016/j.msea.2015.09.068.

[31] H. T. Liu *et al.*, “Effects of rolling temperature on microstructure, texture, formability and magnetic properties in strip casting Fe-6.5 wt% Si non-oriented electrical steel,” *Journal of Magnetism and Magnetic Materials*, vol. 391. pp. 65–74, 2015, doi: 10.1016/j.jmmm.2015.04.105.

[32] H. A. Kuhn, “Workability Theory and Application in Bulk Forming Processes,” *Metalwork. Bulk Form.*, vol. 14, no. Eq 2, pp. 172–187, 2018, doi: 10.31399/asm.hb.v14a.a0009004.

[33] T. Kvackaj *et al.*, “Application of workability test to SPD processing,” *Arch. Metall. Mater.*, vol. 58, no. 2, pp. 407–412, 2013, doi: 10.2478/amm-2013-0008.

[34] H. J. Bunge, *Formability of Metallic Materials Plastic Anisotropy, Formability Testing, Forming Limits*, 1st ed. 20. Berlin, Heidelberg: Springer Berlin Heidelberg, 2000.

[35] R. Mikail, “Fundamentals of Electric Motors and Transformers,” pp. 15–27, 1803.

[36] G. P. Shultz, “Introduction to Transformers,” in *Newnes*, G. P. Shultz, Ed. Boston: Newnes, 1990, p. 107.

[37] H. Li, H. Liu, Z. Liu, H. Lu, H. Song, and G. Wang, “Characterization of microstructure, texture and magnetic properties in twin-roll casting high silicon non-oriented electrical steel,” *Mater. Charact.*, vol. 88, pp. 1–6, 2014, doi: 10.1016/j.matchar.2013.11.014.

[38] D. W. Dietrich, “Magnetically Soft Materials.,” *Sel Mater Serv Env. (Source B. Ser.*, vol. 2, pp. 389–393, 1987, doi: 10.31399/asm.hb.v02.a0001093.

[39] G. Lyudkovsky, P. K. Rastogi, and M. Bala, “Nonoriented Electrical Steels,” *JOM*, vol. 38, no. 1, pp. 18–26, 1986, doi: https://doi.org/10.1007/BF03257950.

[40] K. Raviprasad and K. Chattopadhyay., “The effect of rapid preconditioning on the,” *aterials Sci. Eng. 98*, pp. 281–284, 1988, doi: https://doi.org/10.1016/0025-5416(88)90170-X.

[41] H. Yu, K. Ming, H. Wu, Y. Yu, and X. Bi, “Ordering suppression and excellent ductility in soft-magnetic Fe-6.5 wt%Si sheet by Hf addition,” *J. Alloys Compd.*, vol. 766, pp. 186–193, 2018, doi: 10.1016/j.jallcom.2018.06.343.

[42] P. R. Swann, L. Grånäs, and B. Lehtinen, “The B2 and DO3 Ordering Reactions in Iron–Silicon Alloys in the Vicinity of the Curie Temperature,” *Met. Sci.*, vol. 9, no. 1, pp. 90–96, 1975, doi: 10.1179/030634575790445279.

[43] G. Ouyang *et al.*, “Characterization of ordering in Fe-6.5%Si alloy using X-ray, TEM, and magnetic TGA methods,” *Materials Characterization*, vol. 158. 2019, doi: 10.1016/j.matchar.2019.109973.

[44] G. Ouyang, X. Chen, Y. Liang, C. Macziewski, and J. Cui, “Review of Fe-6.5 wt%Si high silicon steel—A promising soft magnetic material for sub-kHz application,” *Journal of Magnetism and Magnetic Materials*, vol. 481. pp. 234–250, 2019, doi: 10.1016/j.jmmm.2019.02.089.

[45] O. Kubaschewski, *IRON-Binary Phase Diagrams*. Springer, 2013.

[46] Y. U. YI, Z. ZHOU, Z. WANG, S. JIANG, and W. HUANG, “Si-STEEL THIN-STRIP PREPARED BY TWIN-ROLL CONTINUOUS CASTING,” *Surf. Rev. Lett.*, vol. 18, no. 3n04, pp. 97–102, 1900, doi: 10.1142/S0218625X11014515.

[47] B. Verbrugge and D. C. Jiles, “Core loss reduction in electrical steels through materials processing,” *J. Appl. Phys.*, vol. 85, no. 8, pp. 4895–4897, 1999, doi: 10.1063/1.369134.

[48] Y. Sato, T. Sato, and Y. Okazaki, “Production and properties of melt-spun Fe-6.5wt.%Si ribbons,” *Mater. Sci. Eng.*, vol. 99, no. 1, pp. 73–76, 1988, doi: 10.1016/0025-5416(88)90295-9.

[49] S. Suwas and R. K. Ray, *Crystallographic Texture in Materials*. Journal of the Indian Institute of Science, 2016.

[50] B. D. Cullity and C. D. Graham, *Introduction to Magnetic Materials. John Wiley & Son*. John Wiley & Sons, 2011.

[51] H.-J. Bunge, *Texture Analysis in Materials Science: Mathematical Methods*. Butterworth-Heinemann, 2013.

[52] F. J. Humphreys and M. Hatherly, *Recrystallization and related annealing phenomena.*, Third edit. Amsterdam, Netherlands: Elsevier, 2012.

[53] C. Chen, *Magnetism and metallurgy of soft magnetic materials - Chapter 1*. Amsterdam ; North-Holland Pub. Co., 1977.

[54] G. Bertotti, A. Canova, M. Chiampi, D. Chiarabaglio, F. Fiorillo, and A. M. Rietto, “Core loss prediction combining physical models with numerical field analysis,” *J. Magn. Magn. Mater.*, vol. 133, no. 1, pp. 647–650, 1994, doi: 10.1016/0304-8853(94)90646-7.

[55] W. A. Pluta, “Some properties of factors of specific total loss components in electrical steel,” *IEEE Trans. Magn.*, vol. 46, no. 2, pp. 322–325, 2010, doi: 10.1109/TMAG.2009.2033559.

[56] H. Zhao *et al.*, “An Improved Core Loss Model of Ferromagnetic Materials Considering High-Frequency and Nonsinusoidal Supply,” *IEEE Trans. Ind. Appl.*, vol. 57, no. 4, pp. 4336–4346, 2021, doi: 10.1109/IAS44978.2020.9334779.

[57] D. Petrovic, “Non-oriented electrical steel sheets,” *Mater. Tehnol.*, vol. 44, no. 6, pp. 317–325, 2010.

[58] J. Barros, T. Ros-Yañez, L. Vandenbossche, L. Dupré, J. Melkebeek, and Y. Houbaert, “The effect of Si and Al concentration gradients on the mechanical and magnetic properties of electrical steel,” *J. Magn. Magn. Mater.*, vol. 290-291 PA, pp. 1457–1460, 2005, doi: 10.1016/j.jmmm.2004.11.547.

[59] G. Langford, P. K. Nagata, R. J. Sober, and W. C. Leslie, “Plastic Flow in Binary Substitutional Alloys of BCC Iron-Effects of Wire Drawing and Alloys Content on Work Hardening and Ductility,” *Metall. Mater. Trans.*, vol. 3, no. 7, pp. 1843–1849, 1972, doi: 10.1007/BF02642569.

[60] H. Baker and H. Okamoto, *ASM Handbook. Vol. 3. Alloy Phase Diagrams*. 1992.

[61] V. Raghavan, “Cr-Fe-Si (Chromium-Iron-Silicon),” *J. Phase Equilibria Diffus.*, vol. 25, no. 6, pp. 545–546, 2005, doi: 10.1361/15477020421179.

[62] W. Moscoso, M. R. Shankar, J. B. Mann, W. D. Compton, and S. Chandrasekar, “Bulk nanostructured materials by large strain extrusion machining,” *J. Mater. Res.*, vol. 22, no. 1, pp. 201–205, 2007, doi: 10.1557/jmr.2007.0021.

[63] M. N. Issahaq, S. Chandrasekar, and K. P. Trumble, “Single-Step Shear-Based Deformation Processing of Electrical Conductor Wires,” *J. Manuf. Sci. Eng.*, vol. 143, no. 5, 2021, doi: 10.1115/1.4048984.

[64] D. R. Klenosky, D. R. Johnson, S. Chandrasekar, and K. P. Trumble, “Characterization of Large Strain Extrusion Machining (LSEM) of AA7050,” in *Light Metals 2017*, 2017, pp. 301–304, doi: 10.1007/978-3-319-51541-0_40.

[65] R. L. Brown, “Strip Fabrication Using Peeling Techniques,” *Mater. Manuf. Process.*, vol. 4, no. 4, pp. 467–481, 1989, doi: 10.1080/10426918908956310.

[66] A. Middlemiss, D. Hague, and M. C. Gleave, “Strip production by peeling,” *Met. Technol.*, vol. 9, no. 1, pp. 413–418, 1982, doi: 10.1179/030716982803286322.

[67] Y. Guo, M. Efe, W. Moscoso, D. Sagapuram, K. P. Trumble, and S. Chandrasekar, “Deformation field in large-strain extrusion machining and implications for deformation processing,” *Scripta Materialia*, vol. 66, no. 5. pp. 235–238, 2012, doi: 10.1016/j.scriptamat.2011.10.045.

[68] J. H. Yu *et al.*, “The effect of heat treatments and Si contents on B2 ordering reaction in high-silicon steels,” *Mater. Sci. Eng. A*, 2001, doi: 10.1016/S0921-5093(00)01960-2.

[69] J. R. Davis, P. Allen, S. R. Lampman, and T. B. Zorc, “Metals Handbook, Tenth Edition. Vol. 2. Properties and Selection: Nonferrous Alloys and Special-Purpose Materials,” *ASM Handb. Prop. Sel. Nonferrous Alloy. Spec. Mater. Vol. 2*, 1990.

[70] J. Hong, H. Choi, S. Lee, J. K. Kim, and Y. mo Koo, “Effect of Al content on magnetic properties of Fe-Al Non-oriented electrical steel,” *J. Magn. Magn. Mater.*, vol. 439, pp. 343–348, 2017, doi: 10.1016/j.jmmm.2017.03.082.

[71] T. Ros, Y. Houbaert, O. Fischer, and J. Schneider, “Thermomechanical processing of high Si-steel (up to 6.3% Si),” *IEEE Trans. Magn.*, vol. 37, no. 4, pp. 2321–2324, 2001, doi: 10.1109/20.951160.

[72] J. Stodolny and J. Groyecki, “Cold deformability of Fe-Si-Al alloys,” *Phys. Scr.*, vol. 39, no. 2, pp. 279–281, 1989, doi: 10.1088/0031-8949/39/2/017.

[73] M. Littmann, “Iron and silicon-iron alloys,” *IEEE Trans. Magn.*, vol. 7, no. 1, pp. 48–60, 1971, doi: 10.1109/TMAG.1971.1066998.

[74] A. B. Kustas, “Shear-Based Deformation Processing and Characterization of Electrical Steel Sheet,” no. Open Access Dissertations. 1241., p. 161, 2016, [Online]. Available: https://docs.lib.purdue.edu/open_access_dissertations/1241.

[75] F. E. Werner and R. I. Jaffee, “Energy-efficient steels for motor laminations,” *J. Mater. Eng. Perform.*, vol. 1, no. 2, pp. 227–234, 1992, doi: 10.1007/BF02648621.

[76] P. Iglesias, M. D. Bermúdez, W. Moscoso, and S. Chandrasekar, “Influence of processing parameters on wear resistance of nanostructured OFHC copper manufactured by large strain extrusion machining,” vol. 268, pp. 178–184, 2010, doi: 10.1016/j.wear.2009.07.009.

[77] M. Sevier, H. T. Y. Yang, W. Moscoso, and S. Chandrasekar, “Analysis of Severe Plastic Deformation by Large Strain Extrusion Machining,” vol. 39, no. November, pp. 2645–2655, 2008, doi: 10.1007/s11661-008-9608-0.

[78] D. Sagapuram *et al.*, “On control of flow instabilities in cutting of metals,” *CIRP Ann.*, vol. 64, no. 1, pp. 49–52, 2015, doi: 10.1016/j.cirp.2015.04.059.

[79] P. Kumar, R. S. Joshi, and R. K. Singla, “Sliding wear behaviour of CP titanium laminates produced by large strain extrusion machining,” *Wear*, vol. 477, pp. 203774-, 2021, doi: 10.1016/j.wear.2021.203774.

[80] M. Efe, W. Moscoso, K. P. Trumble, W. Dale Compton, and S. Chandrasekar, “Mechanics of large strain extrusion machining and application to deformation processing of magnesium alloys,” *Acta Mater.*, vol. 60, no. 5, pp. 2031–2042, 2012, doi: 10.1016/j.actamat.2012.01.018.

[81] G. E. Dieter, *Mechanical metallurgy - Chapter 17*, 3rd ed. New York: McGraw-Hill, 1986.

[82] D. Sagapuram, M. Efe, W. Moscoso, S. Chandrasekar, and K. P. Trumble, “Controlling texture in magnesium alloy sheet by shear-based deformation processing,” *Acta Mater.*, vol. 61, no. 18, pp. 6843–6856, 2013, doi: 10.1016/j.actamat.2013.07.063.

[83] A. B. Kustas, D. Sagapuram, K. P. Trumble, and S. Chandrasekar, “Texture Development in High-Silicon Iron Sheet Produced by Simple Shear Deformation,” *Metall. Mater. Trans. A Phys. Metall. Mater. Sci.*, vol. 47, no. 6, pp. 3095–3108, 2016, doi: 10.1007/s11661-016-3437-3.

[84] A. B. Kustas, D. Sagapuram, S. Chandrasekar, and K. P. Trumble, “Deformation and recrystallization texture development in Fe-4%Si subjected to large shear deformation,” *IOP Conf. Ser. Mater. Sci. Eng.*, vol. 82, no. 1, pp. 12054-, 2015, doi: 10.1088/1757-899X/82/1/012054.

[85] F. Ren, F. Chen, and J. Chen, “Investigation on dynamic recrystallization behavior of martensitic stainless steel,” *Adv. Mater. Sci. Eng.*, vol. 2014, 2014, doi: 10.1155/2014/986928.

[86] R. Soc and G. Britain, “Recrystallization of metals during hot deformation,” *Philos. Trans. R. Soc. London. Ser. A, Math. Phys. Sci.*, vol. 288, no. 1350, pp. 147–158, 1978, doi: 10.1098/rsta.1978.0010.

[87] D. Sagapuram, M. Efe, W. Moscoso, S. Chandrasekar, and K. P. Trumble, “Deformation temperature effects on microstructure and texture evolution in high strain rate extrusion-machining of Mg-AZ31B,” *Mater. Sci. Forum*, vol. 702–703, pp. 52–55, 2012, doi: 10.4028/www.scientific.net/MSF.702-703.52.

[88] D. Sagapuram *et al.*, “On the Cutting of Metals: A Mechanics Viewpoint,” *J. Manuf. Sci. Eng.*, vol. 142, no. 11, 2020, doi: 10.1115/1.4047869.

[89] J. E. ; Williams, E. F. ; Smart, and D. R. Milner, “The metallurgy of machining I. Basic considerations and the cutting of pure metals,” *Metallurgia*, vol. 81, no. 483, pp. 3–10, 1970.

[90] E. R. Davies, *Introduction to texture analysis*. Handbook of Texture Analysis, 2008.

[91] C. Okolieocha, D. Raps, K. Subramaniam, and V. Altstädt, “Microcellular to nanocellular polymer foams: Progress (2004-2015) and future directions - A review,” *Eur. Polym. J.*, vol. 73, pp. 500–519, 2015, doi: 10.1016/j.eurpolymj.2015.11.001.

[92] P. R. Rios, F. J. Siciliano, H. R. Zschommler Sandim, R. L. Plaut, and A. F. Padilha, “Nucleation and Growth During Recrystallization,” *Mater. Res.*, vol. 8, no. 3, pp. 225–238, 2005, doi: 10.1016/0886-7798(94)90054-X.

[93] P. A. Beck, “The formation of recrystallization nuclei [6],” *J. Appl. Phys.*, vol. 20, no. 6, pp. 633–634, 1949, doi: 10.1063/1.1698446.

[94] Y. Huang and F. J. Humphreys, “Subgrain growth and low angle boundary mobility in aluminium crystals of orientation {110}〈001〉,” *Acta Mater.*, vol. 48, no. 8, pp. 2017–2030, 2000, doi: 10.1016/S1359-6454(99)00418-8.

[95] A. D. Rollett, G. Gottstein, L. S. Shvindlerman, and D. A. Molodov, “Grain boundary mobility – a brief review,” *Zeitschrift für Met.*, vol. 95, no. 4, pp. 226–229, Apr. 2004, doi: 10.3139/146.017938.

[96] R. D. Doherty *et al.*, “Current issues in recrystallization: A review,” *Mater. Sci. Eng. A*, vol. 238, no. 2, pp. 219–274, 1997, doi: 10.1016/S0921-5093(97)00424-3.

[97] P. R. Calvillo, N. Salazar, J. Schneider, and Y. Houbaert, “Microstructure characterization by EBSD of hot rolled high-silicon steel,” *Defect Diffus. Forum*, vol. 273–276, pp. 69–74, 2008, doi: 10.4028/www.scientific.net/ddf.273-276.69.

[98] Y. Xu, H. Jiao, W. Qiu, R. D. K. Misra, and J. Li, “Effect of cold rolling process on microstructure, texture and properties of strip cast Fe-2.6%Si steel,” *Materials (Basel).*, vol. 11, no. 7, 2018, doi: 10.3390/ma11071161.

[99] J. T. Park and J. A. Szpunar, “Evolution of recrystallization texture in nonoriented electrical steels,” *Acta Mater.*, vol. 51, no. 11, pp. 3037–3051, 2003, doi: 10.1016/S1359-6454(03)00115-0.

[100] S. S. F. De Dafé, S. D. C. Paolinelli, and A. B. Cota, “Influence of thermomechanical processing on shear bands formation and magnetic properties of a 3% Si non-oriented electrical steel,” *J. Magn. Magn. Mater.*, vol. 323, no. 24, pp. 3234–3238, 2011, doi: 10.1016/j.jmmm.2011.07.015.

[101] K. M. Lee *et al.*, “Effect of hot band grain size on development of textures and magnetic properties in 2.0% Si non-oriented electrical steel sheet,” *J. Magn. Magn. Mater.*, vol. 396, pp. 53–64, 2015, doi: 10.1016/j.jmmm.2015.08.010.

[102] A. Stöcker, A. Franke, H. Hermann, and R. Kawalla, “Influence of hot rolling condition on the final microstructure of nonoriented electrical steel Fe-3.2 wt.% Si,” *Mater. Sci. Forum*, vol. 854, pp. 16–21, 2016, doi: 10.4028/www.scientific.net/MSF.854.16.

[103] H. Jiao *et al.*, “Significant effect of as-cast microstructure on texture evolution and magnetic properties of strip cast non-oriented silicon steel,” *J. Mater. Sci. Technol.*, vol. 34, no. 12, pp. 2472–2479, 2018, doi: 10.1016/j.jmst.2018.05.007.

[104] S. da C. Paolinelli, M. A. da Cunha, and A. B. Cota, “The influence of shear bands on final structure and magnetic properties of 3% Si non-oriented silicon steel,” *J. Magn. Magn. Mater.*, vol. 320, no. 20, pp. 641–644, 2008, doi: 10.1016/j.jmmm.2008.04.050.

[105] X. Lu *et al.*, “Evolution of microstructure and texture in grain-oriented 6.5%Si steel processed by strip-casting,” *Mater. Charact.*, vol. 126, pp. 125–134, 2017, doi: 10.1016/j.matchar.2017.02.022.

[106] H. T. Liu *et al.*, “Effects of initial microstructure and texture on microstructure, texture evolution and magnetic properties of non-oriented electrical steel,” *J. Magn. Magn. Mater.*, vol. 406, pp. 149–158, 2016, doi: 10.1016/j.jmmm.2016.01.018.

[107] Y. Lü, D. A. Molodov, and G. Gottstein, “Recrystallization kinetics and microstructure evolution during annealing of a cold-rolled Fe-Mn-C alloy,” *Acta Mater.*, vol. 59, no. 8, pp. 3229–3243, 2011, doi: 10.1016/j.actamat.2011.01.063.

[108] M. Koizumi and H. Inagaki, “Role of shear band in texture control of Al-Mg alloys,” *Met. Mater. Int.*, vol. 5, no. 6, pp. 511–517, 1999, doi: 10.1007/BF03026297.

[109] H. Pan, Z. Zhang, and J. Xie, “The effects of recrystallization texture and grain size on magnetic properties of 6.5 wt% Si electrical steel,” *J. Magn. Magn. Mater.*, vol. 401, pp. 625–632, 2016, doi: 10.1016/j.jmmm.2015.10.047.

[110] G. Sahoo, C. D. Singh, M. Deepa, S. K. Dhua, and A. Saxena, “Recrystallization behaviour and texture of non-oriented electrical steels,” *Mater. Sci. Eng. A*, vol. 734, no. July, pp. 229–243, 2018, doi: 10.1016/j.msea.2018.07.072.

[111] M. Shiozaki and Y. Kurosaki, “The effects of grain size on the magnetic properties of nonoriented electrical steel sheets,” *J. Mater. Eng.*, vol. 11, no. 1, pp. 37–43, 1989, doi: 10.1007/BF02833752.

[112] K. Matsumura and B. Fukuda, “Recent developments of non-oriented electrical steel sheets,” *IEEE Trans. Magn.*, vol. 20, no. 5, pp. 1533–1538, 1984, doi: 10.1109/TMAG.1984.1063223.

[113] E. T. Stephenson and A. R. Marder, “Effects of Grain Size on the Core Loss and Permeability of Motor Lamination Steel.,” *IEEE Trans. Magn.*, vol. MAG-22, no. 2, pp. 101–106, 1986, doi: 10.1109/tmag.1986.1064281.

[114] M. Fanfoni and M. Tomellini, “The Johnson-Mehl-Avrami-Kolmogorov model: A brief review,” *Nuovo Cim. della Soc. Ital. di Fis. D - Condens. Matter, At. Mol. Chem. Physics, Biophys.*, vol. 20, no. 7, pp. 1171–1182, 1998, doi: 10.1007/BF03185527.

[115] M. Ohring, “How Engineering Materials Are Strengthened and Toughened,” *Eng. Mater. Sci.*, vol. 3, pp. 431–500, 1995, doi: 10.1016/b978-012524995-9/50033-7.

[116] V. Erukhimovitch and J. Baram, “Modeling recrystallization kinetics,” *Mater. Sci. Eng. A*, vol. 214, no. 1–2, pp. 78–83, 1996, doi: 10.1016/0921-5093(96)10223-9.

[117] R. Y. Wang *et al.*, “A Generalized Avrami Equation for Crystallization Kinetics of Polymers with Concomitant Double Crystallization Processes,” *Cryst. Growth Des.*, vol. 17, no. 11, pp. 5908–5917, 2017, doi: 10.1021/acs.cgd.7b01016.

[118] A. Fenghui, L. Bo, Z. Deqin, L. Jinlong, and S. Yuhui, “Recrystallization kinetics of Fe-3%Si after deformation at high strain rate and high temperature,” *Mater. Res.*, vol. 22, pp. 1–6, 2019, doi: 10.1590/1980-5373-MR-2018-0746.

[119] J. Schneider, A. Stöcker, A. Franke, and R. Kawalla, “Effects by the microstructure after hot and cold rolling on the texture and grain size after final annealing of ferritic non-oriented FeSi electrical steel,” *AIP Adv.*, vol. 8, no. 4, pp. 1–14, 2018, doi: 10.1063/1.4993526.

[120] J. W. Cahn, “The kinetics of grain boundary nucleated reactions,” *Acta Metall.*, vol. 4, no. 5, pp. 449–459, 1956, doi: 10.1016/0001-6160(56)90041-4.

[121] N. X. Sun, X. D. Liu, and K. Lu, “An explanation to the anomalous Avrami exponent,” *Scr. Mater.*, vol. 34, no. 8, pp. 1201–1207, 1996, doi: 10.1080/07362994.2014.961088.

[122] A. D. Rollett, D. J. Srolovitz, R. D. Doherty, and M. P. Anderson, “Computer simulation of recrystallization in non-uniformly deformed metals,” *Acta Metall.*, vol. 37, no. 2, pp. 627–639, 1989, doi: 10.1016/0001-6160(89)90247-2.

[123] H. Luo, J. Sietsma, and S. van der Zwaag, “A metallurgical interpretation of the static recrystallization kinetics of an intercritically deformed C-Mn steel,” *Metall. Mater. Trans. A Phys. Metall. Mater. Sci.*, vol. 35 A, no. 6, pp. 1889–1898, 2004, doi: 10.1007/s11661-004-0097-5.

[124] F. De Las Cuevas *et al.*, “Kinetics of recrystallization and grain growth of cold rolled TWIP steel,” *Adv. Mater. Res.*, vol. 89–91, pp. 153–158, 2010, doi: 10.4028/www.scientific.net/AMR.89-91.153.

[125] N. Rajmohan, J. A. Szpunar, and Y. Hayakawa, “Goss Texture Development in Fe–Si Steels,” *Textures Microstruct.*, vol. 32, no. 1–4, pp. 153–174, 1999.

[126] S. Mishra, C. Därmann, and K. Lücke, “On the development of the goss texture in iron-3% silicon,” *Acta Metall.*, vol. 32, no. 12, pp. 2185–2201, 1984.

[127] M. Y. Huh and O. Engler, “Effect of intermediate annealing on texture, formability and ridging of 17%Cr ferritic stainless steel sheet,” *Mater. Sci. Eng. A*, vol. 308, no. 1–2, pp. 74–87, 2001, doi: 10.1016/S0921-5093(00)01995-X.

[128] S. Li, I. J. Beyerlein, and M. A. M. Bourke, “Texture formation during equal channel angular extrusion of fcc and bcc materials: comparison with simple shear,” *Mater. Sci. Eng. A. Struct. Mater.*, vol. 394, no. 1, pp. 66–77, 2005, doi: 10.1016/j.msea.2004.11.032.

[129] H. Miyamoto, T. Xiao, T. Uenoya, and M. Hatano, “Effect of simple shear deformation prior to cold rolling on texture and ridging of 16% Cr ferritic stainless steel sheets,” *ISIJ Int.*, vol. 50, no. 11, pp. 1653–1659, 2010, doi: 10.2355/isijinternational.50.1653.

[130] R. B. Singh, D. Verma, N. K. Mukhopadhyay, G. V. S. Sastry, and R. Manna, “Development of Texture in Ultrafine-Grained Low-Carbon Steel Processed through Equal-Channel Angular Pressing,” *J. Mater. Eng. Perform.*, vol. 28, no. 6, pp. 3638–3651, 2019, doi: 10.1007/s11665-019-04085-0.

[131] D. Verma, S. K. Shekhawat, N. K. Mukhopadhyay, G. V. S. Sastry, and R. Manna, “Development of Texture in Interstitial-Free Steel Processed by Equal-Channel Angular Pressing,” *J. Mater. Eng. Perform.*, vol. 25, no. 3, pp. 820–830, 2016, doi: 10.1007/s11665-016-1912-z.

[132] J. F. Gieras, *Advancements in Electric Machines by J. F. Gieras: Chapter 2, Materials Engineering.*, 1st ed. 20. Dordrecht: Springer Netherlands, 2008.

[133] E. T. Stephenson, “Effects of thickness and resistivity on core loss and permeability of nonoriented semiprocessed steels,” *J. Appl. Phys.*, vol. 55, no. 6, pp. 2142–2144, 1984, doi: 10.1063/1.333590.

[134] G. Bertotti, “General Properties of Power Losses in Soft Ferromagnetic Materials.,” *IEEE Trans. Magn.*, vol. 24, no. 1, pp. 621–630, 1987, doi: 10.1109/20.43994.

[135] G. Bertotti, D. Chiarabaglio, F. Fiorillo, A. Boglietti, M. Chiampi, and M. Lazzari, “An improved estimation of iron losses in rotating electrical machines,” *IEEE Trans. Magn.*, vol. 27, no. 6, pp. 5007–5009, 1991, doi: 10.1109/20.278722.

[136] L. Meyer, F. Schmidt, and C. Strassburger, “Influence of niobium and vanadium on the structure and properties of low-pearlite aluminium-killed steels,” *STAHL EISEN*, vol. 89, no. 22, pp. 1235–1249, 1969.

[137] H. Shimanaka, Y. Itoh, T. Irie, K. Matsumura, H. Nakamura, and Y. Shono, “Nonoriented Silicon Steels Useful for Energy Efficient Electrical Apparatus,” *Energy Effic. Electr. Steels - J. Met.*, vol. 32, no. 8, p. 12, 1980.

[138] R. R. Judd and K. E. Blazek, “Effect of High-Temperature Annealing on the Magnetic Properties of Fully Processed Nonoriented Silicon Steel Sheets,” *Energy Effic. Electr. Steels; Pittsburgh; Pa.; 5-9 Oct. 1980*, pp. 147–155, 1980.

[139] P. Charpentier and J. H. Bucher, “Effects of structural variables on the magnetic properties of cold rolled carbon steels.,” *Mech. Work. Steel Process. X. AIME*, pp. 61–98, 1972.

[140] E. Stephenson and A. Marder, “The effects of grain size on the core loss and permeability of motor lamination steel,” *IEEE Trans. Magn.*, vol. 22, no. 2, pp. 101–106, 1986, doi: 10.1109/TMAG.1986.1064281.